

REPORT DOCUMENTATION PAGE

AFRL-SR-BL-TR-99-

Public reporting burden for this collection of information is estimated to average 1 hour per response, including gathering and maintaining the data needed, and completing and reviewing the collection of information. Send comments regarding this burden estimate or any aspect of this collection of information, including suggestions for reducing this burden, to Washington Headquarters Service, Paperwork Project, Davis Highway, Suite 1204, Arlington, VA 22202-4302, and to the Office of Management and Budget, Paperwork Project, Washington, DC 20503.

0121

data sources,
spect of this
15 Jefferson

| | | | | | |
|---|--|---|----------------------------|---|--|
| 1. AGENCY USE ONLY (Leave Blank) | | 2. REPORT DATE 3/1/99 | | 3. REPORT TYPE AND DATES COVERED Final Report 10/1/94 - 12/31/98 | |
| 4. TITLE AND SUBTITLE Aerodynamic Response of Turbomachinery Blade Rows to Convecting Density Wakes | | | | 5. FUNDING NUMBERS F49620-98-1-0272 | |
| 6. AUTHORS Dr. Choon S. Tan, Principal Research Engineer Prof. Eugene E. Covert, T. Wilson Professor, Emeritus Ramer, B. (Research Assistant), Wijesinghe, H.S. (Research Assistant) | | | | | |
| 7. PERFORMING ORGANIZATION NAME(S) AND ADDRESS(ES) Gas Turbine Lab, Bldg. 31-254 Massachusetts Institute of Technology, 77 Massachusetts Avenue, Cambridge, MA 02139. | | | | 8. PERFORMING ORGANIZATION REPORT NUMBER | |
| 9. SPONSORING / MONITORING AGENCY NAME(S) AND ADDRESS(ES) Air Force Office of Scientific Research Bolling Air Force Base 110 Duncan Avenue, Suite B115 DC 20332-8080 | | | | 10. SPONSORING / MONITORING AGENCY REPORT NUMBER | |
| 11. SUPPLEMENTARY NOTES | | | | | |
| 12a. DISTRIBUTION / AVAILABILITY STATEMENT | | | | 12b. DISTRIBUTION CODE | |
| 13. ABSTRACT (Maximum 200 words) The aim of the current research has been to contribute to the "aerodynamic forcing function" aspect of the high cycle fatigue problem. In this regard density wakes were identified as a potential new source of turbomachinery blade vibration. In order to characterize the density wake induced force and moment fluctuations a two-dimensional computational study was conducted to simulate the passage of density wakes through a cascade blade row. Both inviscid incompressible flows and viscous compressible flows ($M_\infty=0.15$ to $M_\infty=0.87$ and Reynolds number $Re(c,U_\infty) \approx 700,000$) were considered. The inviscid flow simulations show a pair of counterrotating vortices in the blade passage and a flux of density wake fluid to the blade suction/pressure surface as low/high density wakes convect through the blade row. This fluid flux is found to be the key mechanism which affects the blade static pressure distribution and hence the blade force and moment response. The viscous flow simulations have uncovered additional mechanisms for blade force and moment fluctuations: (1) periodic vortex shedding at the blade trailing edge, (2) convecting separation bubbles on the blade suction surface (due to the density wake - blade boundary layer interaction) and (3) axial deflection of the blade passage shock wave position (due to the density wake - shock wave interaction). Simple functional relationships have been derived to quantify the force and moment fluctuations for each flow simulation. A simple cascade flow model has also been developed to determine parametric trends in the blade force and moment fluctuations with varying density wake properties and compressor geometries. | | | | | |
| 14. SUBJECT TERMS Density Wakes Turbomachinery Forced Response High Cycle Fatigue | | | | 15. NUMBER OF PAGES 109 | |
| | | | | 16. PRICE CODE | |
| 17. SECURITY CLASSIFICATION OF REPORT Unclassified | 18. SECURITY CLASSIFICATION OF THIS PAGE Unclassified | 19. SECURITY CLASSIFICATION OF ABSTRACT Unclassified | 20. LIMITATION OF ABSTRACT | | |

Aerodynamic Response of Turbomachinery Blade Rows to Convecting Density Wakes

Summary

This document constitutes the final report for AFOSR contract number F49620-9~~7~~⁸-1-0202. Results from the research conducted during the period October 1, 1994 to December 31, 1998 are presented here.

19990517 017

Abstract

The aim of the current research has been to contribute to the “aerodynamic forcing function” aspect of the high cycle fatigue problem. In this regard *density wakes* were identified as a potential new source of turbomachinery blade vibration. In order to characterize the density wake induced force and moment fluctuations a two-dimensional computational study was conducted to simulate the passage of density wakes through a cascade blade row. Both inviscid incompressible flows and viscous compressible flows ($M_\infty = 0.15$ to $M_\infty = 0.87$ and Reynolds number $Re(c, U_\infty) \approx 700,000$) were considered.

The inviscid flow simulations show a pair of counterrotating vortices in the blade passage and a flux of density wake fluid to the blade suction/pressure surface as low/high density wakes convect through the blade row. This fluid flux is found to be the key mechanism which affects the blade static pressure distribution and hence the blade force and moment response.

The viscous flow simulations have uncovered additional mechanisms for blade force and moment fluctuations: (1) periodic vortex shedding at the blade trailing edge, (2) convecting separation bubbles on the blade suction surface (due to the density wake - blade boundary layer interaction) and (3) axial deflection of the blade passage shock wave position (due to the density wake - shock wave interaction).

Simple functional relationships have been derived to quantify the force and moment fluctuations for each flow simulation. A simple cascade flow model has also been developed to determine parametric trends in the blade force and moment fluctuations with varying density wake properties and compressor geometries.

Nomenclature

Symbols

| | |
|------------------|--|
| c | Blade chord |
| d | Spacing of counterrotating vortices |
| e | Energy |
| h | Blade spacing |
| | Height of counterrotating vortices above flat plate |
| i | $\sqrt{-1}$ |
| k | Index of summation |
| l | Moment arm length |
| l_1 | Upstream extent of flat plate pressure distribution |
| l_2 | Downstream extent of flat plate pressure distribution |
| p | Static pressure |
| r | Distance from line vortex |
| s_1, s_2 | Constants in expression for counterrotating vortex strengths |
| t | Time |
| u | Velocity in axial direction |
| v | Velocity in azimuthal direction |
| v_f | Fluid flux velocity in azimuthal direction |
| w | Wake width |
| | Induced velocity |
| x | Axial direction coordinate |
| y | Azimuthal direction coordinate |
| y^+ | Boundary layer coordinate $(\sqrt{\tau_w/\rho y})/\nu$ |
| A_{eff} | Effective area used in cascade model |
| C_μ | Turbulence model constant |
| C_1 | Turbulence model constant |
| C_2 | Turbulence model constant |
| C_f | Wall skin friction coefficient |
| C_m | Moment coefficient about mid chord (positive clockwise) |
| C_p | Pressure coefficient |
| ΔC_{p_s} | Static pressure rise coefficient across the shock wave |
| C_x | Axial force coefficient |
| C_y | Azimuthal force coefficient |
| K | Constant of proportionality in cascade model |
| M | Mach number |
| N | Number of discrete vortex panels |
| R | Gas constant |
| Re | Reynolds number |
| St | Strouhal number |
| T | Flat plate cascade spacing |
| U | Total velocity |

| | |
|-------------------|--|
| U_R | Rotor tip speed |
| U_{edge} | Boundary layer edge velocity at blade trailing edge |
| α | Angle between flow and flat plate |
| β_1 | Flat plate stagger angle |
| δ^* | Boundary layer displacement thickness |
| η | Coordinate normal to flat plate |
| γ | Ratio of specific heats ($\gamma = 1.4$) |
| λ | Position of density discontinuity |
| μ | Reduced frequency (fc/U) |
| | Viscosity |
| ν | Kinematic viscosity |
| ω | Vorticity |
| ρ | Density |
| ρ^* | Density parameter $(\rho_2 - \rho_1)/(\rho_2 + \rho_1)$ |
| Ψ_{s-s} | Static to static pressure rise coefficient |
| ξ | Coordinate along flat plate |
| σ | Flat plate cascade space-chord ratio (T/c) |
| σ_κ | Turbulence model constant |
| σ_ϵ | Turbulence model constant |
| θ | Boundary layer momentum thickness |
| τ | Non dimensional time |
| τ_w | Wall shear stress |
| ϑ | Blade trailing edge thickness |
| ζ | Location of any point in the complex plane ($\zeta = \xi + i\eta$) |
| Γ | Circulation strength |
| Γ_A | Circulation strength of counterrotating vortex A |
| Γ_B | Circulation strength of counterrotating vortex B |
| Γ_k | Circulation strength of vortex panel k |
| Γ_{max} | Maximum circulation strength of counterrotating vortices |

Subscripts

| | |
|----------|--|
| 1 | Free stream or value outside density wake |
| 2 | Value inside density wake |
| | Behind density discontinuity for Marble's analysis |
| ∞ | Free stream value or total value |

Operators and Modifiers

| | |
|--------------|------------------------------|
| $\tilde{()}$ | Non-dimensionalized quantity |
| Δ | Difference operator |

∇ Gradient operator

Acronyms

| | |
|----------|------------------------------|
| HCF | High Cycle Fatigue |
| CFD | Computational Fluid Dynamics |
| DFT, dft | Discrete Fourier Transform |

1 Background

Increased operational requirements and increased thrust to weight ratios have led to higher mean and fluctuating stresses in components of modern turbomachinery. This has increased the likelihood of encountering high cycle fatigue (HCF) failure in fan, compressor and turbine blades.

The large number of parameters and the wide occurrence of HCF producing conditions over the engine operating regime imply that structural integrity must be evaluated in an extremely large number of situations. An additional implication is that it is difficult to extract general guidelines for high cycle fatigue prevention because of the high dimensionality of the parameter space that must be explored [1]. Further complexity is introduced by the diversity of local phenomena, e.g. tip leakage flows, unsteady shock motion and local separation that are characteristic of turbomachinery flows. The lack of HCF design principles which consider these flow phenomena is exemplified in the following statement taken from a recent HCF workshop held at the MIT Gas Turbine Laboratory [1]: *“...forced blade response is not currently predictable, and structural design and analysis for high cycle fatigue situations have not advanced beyond the early concepts of the fatigue limit, the Goodman diagram and Miner’s rule.”*

The aim of the current research is to focus on aerodynamic characterization of blade force response to help increase the predictive capability of HCF failure¹. Several forced vibration “sources” exist in turbomachinery. In particular viscous wakes from upstream blade rows and potential flow effects due to rotor–stator interaction have received a lot of attention (Kemp and Sears [13], Kerrebrock and Mikolajczak [14], Manwaring and Wisler [17], Valkov [27])². The forced vibration source considered in this study are convecting density wakes. Density wakes can enter the engine from ground ingested hot air, steam ingestion during carrier launches and exhaust gas ingestion from forward firing weapons [21]. The difference in temperature between the blades and the surrounding fluid can also generate density gradients particularly in the downstream wakes of blades. Incomplete and non-uniform combustion can also introduce density gradients into the flow entering turbines.

2 Technical Approach

Computational fluid dynamics (CFD) is the “tool” used in this research to investigate the forces and moments induced by convecting density wakes. CFD is a relatively inexpensive and convenient method to investigate flow phenomena compared to experimental investigations in wind tunnels. In particular the flow field properties at any location in the computational domain can be conveniently determined and an overall “picture” of the flow

¹Note that forced vibrations are distinct from self excited vibrations due to blade flutter and dynamic stall.

²Note these studies are primarily concerned with compressor performance and the corresponding effects on unsteady blade loading have not been considered.

can be generated to help identify specific flow features. The flow geometry and free stream conditions are also easily changed within a CFD simulation compared to an experimental facility where arbitrary changes in flow geometry are generally not feasible.

The use of CFD is constrained by available computational resources however. This research has therefore been limited to two-dimensional unsteady flows with a single compressor blade row geometry. While turbine blades are subjected to larger density non-uniformities (due to hot-streaks from the combustor and from blade cooling), compressor blades are considered here since they are more susceptible to HCF failure.

The compressor blade profile used in this study is the General Electric, Low Speed Research Compressor (LSRC) Stator-B blade. The geometry of this blade is described in Section 14.3.

The density wakes considered convect along the axial direction and have density gradients directed only in the axial direction. Discussion is focused on low density wakes (wake densities lower than free stream density) which are more common in compressor blade passages. To help isolate individual flow features a single density wake is convected through the blade passage in all simulations. The density variation inside the density wake is specified to be sinusoidal. This variation is considered to be a representative case.

To investigate the wide parameter space of density wake – cascade blade row interactions a simple cascade model is also developed. The model uses a combination of singularity solutions and a proportional constant determined from the inviscid CFD results.

Subsequent sections in this report are organized as follows :

- Physical description of the origin of density wake induced blade forces.
- Theoretical background which includes the derivation of non-dimensional scaling relationships.
- Results from the inviscid flow simulations
- Results from the viscous flow simulations.
- Results from the cascade flow model.
- Appendices:
 - Description of the viscous flow solver, computational grid and non-dimensionalization.
 - Blade force and moment fluctuation profiles.
 1. Baseline response and boundary layer profiles.
 2. Primary and secondary response - time histories and functional relationships.
 3. Primary response compressibility scaling.
 - Cascade model source code.

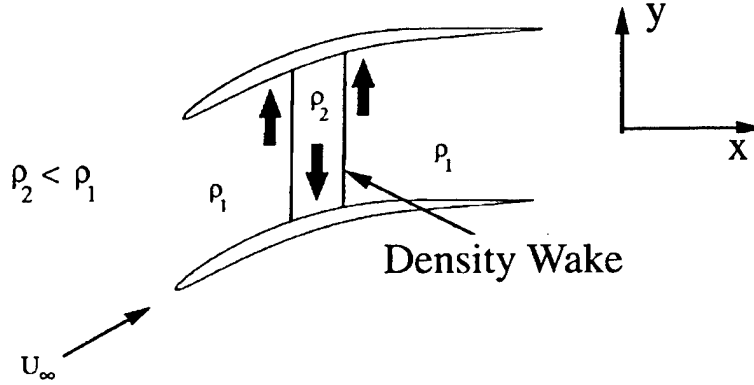


Figure 1: Density wake convecting through a compressor blade row.

3 Physical Origin of Unsteadiness

An analogy to the passage of a density wake through a compressor blade row can be found in the atmosphere; low density (high temperature) air rises to higher altitudes where the pressure is lower and remains there because of force equilibrium. Similarly, high density (low temperature) air sinks to regions of high pressure nearer to the earth.

Now consider the passage of a density wake through a cascade blade row as illustrated in Figure 1. Assume the wake has a lower density than the free stream density. As the wake moves through the cascade, the low density fluid migrates towards the suction side (low pressure side) of the blades by the action of centrifugal forces. To satisfy mass conservation the surrounding higher density fluid is subsequently displaced toward the pressure side of the blade. This relative motion of low and high density fluids generates a pair of counterrotating vortices in the blade passage. The low density fluid directed toward the blade suction surface and the associated counterrotating vortices convect through the blade passage together with the density wake.

The blade pressure distribution is influenced by the impact of the low density fluid on the blade surface. The blade force and moment coefficients therefore change with time during passage of the density wake.

4 Theoretical Background: Marble's Linearized Analysis

For the case of a density wake convecting through a compressor blade row as shown in Figure 1 the density gradients and pressure gradients are misaligned by almost 90 degrees.

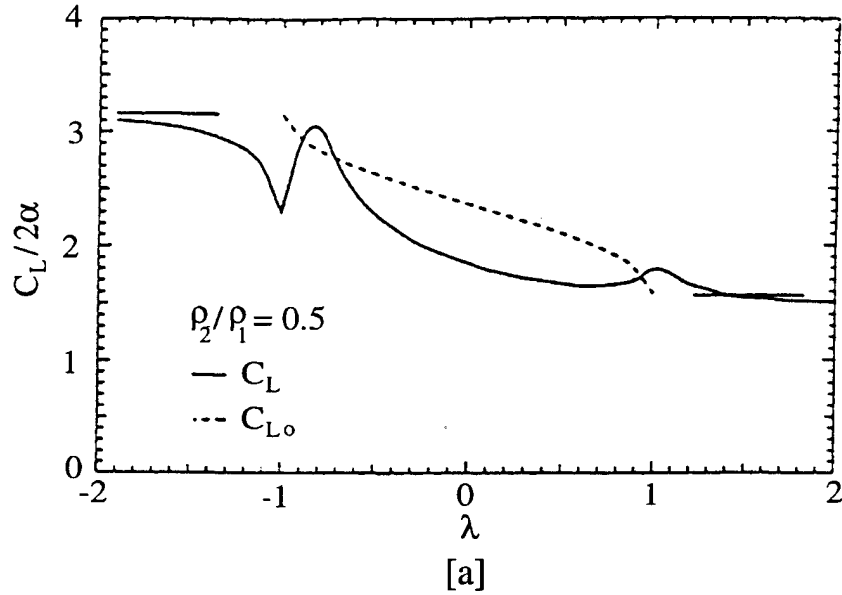


Figure 2: Lift coefficient fluctuation during passage of a density discontinuity over a flat plate. λ is the position of the density discontinuity as it convects along the flat plate. The flat plate lies between $|\lambda| \leq 1$.

This misalignment allows for vorticity production in the flow³. For a continuous density distribution in two-dimensional, inviscid, incompressible flow this vorticity satisfies the linearized relation,

$$\left(\frac{\partial}{\partial t} + u \frac{\partial}{\partial x} \right) \omega = \frac{1}{\rho^2} \nabla p \times \nabla \rho \quad (1)$$

If the density gradient ($\nabla \rho$) is large (zeroth order), the convected vorticity ω is of the same order as the pressure field [18].

The first study of density gradients as a source of flow unsteadiness was conducted by Marble [18]. He performed a linearized potential flow analysis for a flat plate at an angle of attack α encountering a density discontinuity. If the fluid is treated as incompressible and the velocity disturbances caused by the airfoil are small compared to the free stream velocity, the density field can be expressed as $\rho(x - ut, y)$ [18]. The results of Marble's analysis are shown in Figure 2 and Figure 3. In these Figures λ is the position of the density discontinuity as it convects over the flat plate. The flat plate lies between $|\lambda| \leq 1$.

³The generation of vorticity due to the misalignment of density gradients and pressure gradients is often referred to as "baroclinic torque".

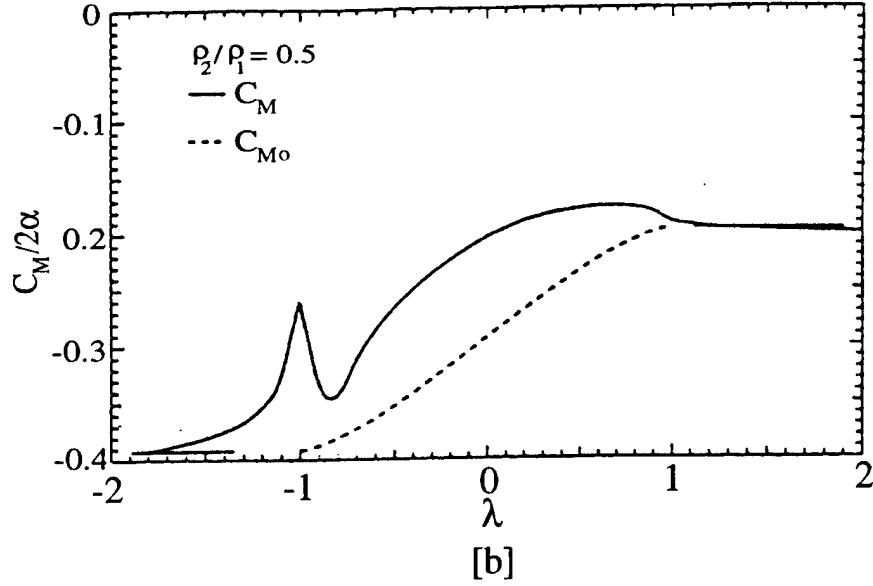


Figure 3: Moment coefficient fluctuation during passage of a density discontinuity over a flat plate. λ is the position of density discontinuity as it convects along the flat plate. The flat plate lies between $|\lambda| \leq 1$.

The dotted lines correspond to the quasi-steady results while the solid lines correspond to the unsteady results. Initially the effect of the density discontinuity is to reduce the local lift. This is a consequence of a downwash velocity field which precedes the arrival of the discontinuity. This is followed by a rapid rise in lift as the discontinuity convects over the leading edge. This is caused by an upwash velocity field behind the discontinuity. A gradual relaxation of the perturbation occurs as the density discontinuity convects further downstream. The final steady lift scales with the ratio of the density across the discontinuity. The moment coefficient shown in Figure 3 also reflects these events in local loading.

Marble's linearized analysis provides a basic understanding of the parameters involved in this problem. In particular the density parameter ρ^* ,

$$\rho^* = \frac{\rho_2 - \rho_1}{\rho_2 + \rho_1} \quad (2)$$

is shown to be a key parameter in the unsteady loading. Re-writing Equation 1 using the density parameter ρ^* and the non-dimensionalized vorticity $\tilde{\omega} = \omega c/U_\infty$ gives,

$$\frac{D\tilde{\omega}}{D\tilde{\tau}} = \frac{c^2}{wh} \rho^* \left[\frac{1}{\rho^2} \left(\tilde{\nabla}_w \tilde{\rho} \times \tilde{\nabla}_h \tilde{p} \right) \right] \quad (3)$$

where,

$$\tilde{p} = \frac{p}{(\rho_2 - \rho_1)U_\infty^2}$$

$$\tau = \frac{U_\infty}{c}t$$

$$\tilde{\rho} = \frac{\rho}{\rho_1 + \rho_2}$$

$$\tilde{\nabla}_w = w\nabla$$

$$\tilde{\nabla}_h = h\nabla$$

Equation 3 suggests the non-dimensional wake width w/c and non-dimensional blade spacing h/c to be additional key parameters.

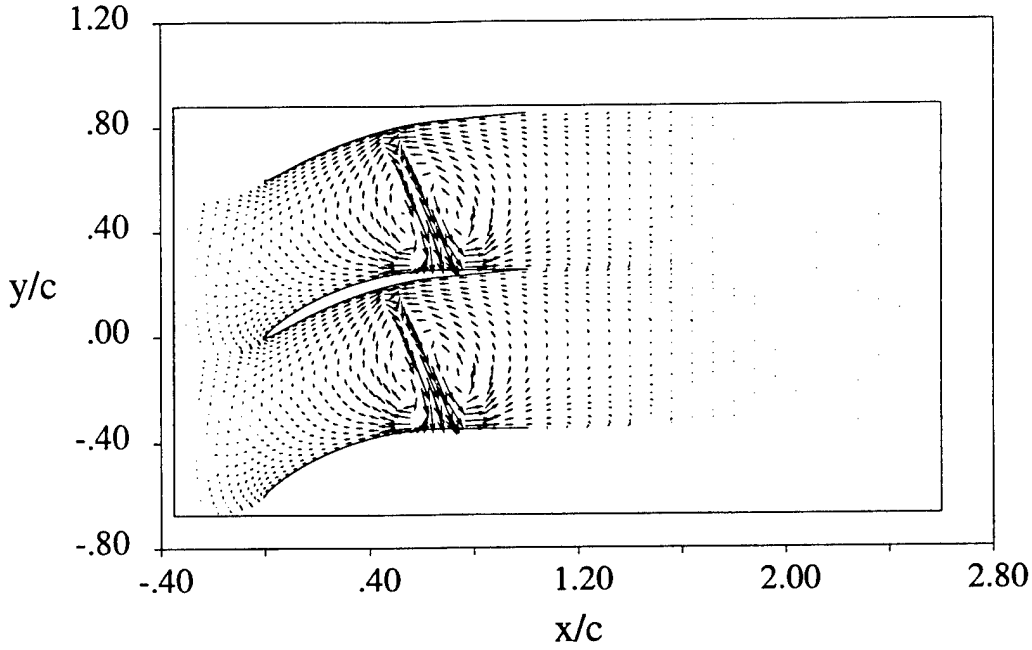


Figure 4: Perturbation velocity vectors during passage of a density wake of width $0.2c$ and density ratio 0.5 through the NACA4F blade row. The flow is inviscid and incompressible. $\tau = 0.65$.

5 Results From The Inviscid Flow Simulations

The inviscid flow simulations capture the essential flow physics of the density wake – blade row interaction described in Section 3. In particular the passage of low density wake fluid to the blade suction surface and the formation of counterrotating vortex pairs within the blade passage are observed. The perturbation velocity vectors in Figure 4 obtained during passage of a density wake of width $0.2c$ and density ratio 0.5 clearly illustrate these flow features.

The transport of the low density wake fluid to the blade suction surface constitutes a fluid flux which can be expressed mathematically as,

$$\text{fluid flux} = \int_0^{w/c} \rho v_f dx \quad (4)$$

where ρ is the wake density, v_f is the velocity of the wake fluid and dx is a increment in length parallel to the axial flow direction. ρ and v_f are functions of x . v_f and non-dimensional wake width w/c are also functions of time τ .

The impingement of the low density fluid on the blade suction surface results in a local

increase in the blade static pressure. As the density wake convects downstream the static pressure increase moves further aft along the blade suction surface. This effect can be seen in the suction surface pressure distribution plotted in Figure 5. A corresponding decrease in static pressure occurs at the blade pressure surface due to the "suction" effect of the counterrotating vortices. The net result is a local reduction in the static pressure difference across the blade and a time varying fluctuation in the blade force and moment.

The magnitude of the force and moment fluctuations increases as the fluid flux to the blade surface increases. Hence larger wake widths and smaller density ratios increase the magnitude of the blade force and moment fluctuations ⁴. Figure 6 shows the time varying azimuthal force coefficient and moment coefficient during passage of a range of density wakes. Initially a reduction in the azimuthal force occurs as the density wake convects over the front half of the blade. This is followed by a gradual return to steady state as the density wake leaves the blade trailing edge. Similarly an increase in the counterclockwise moment occurs as the density wake convects over the front half of the blade. As the density wake passes the blade mid chord, the moment decreases back towards steady state. The shape of these force and moment profiles are roughly common over the range of density wake widths, $0.1 \leq w/c \leq 0.4$, and density ratios $0.25 \leq \rho_2/\rho_1 \leq 2.0$ considered.

The amplitude of the maximum fluctuations in the force and moment coefficients were found to scale linearly for small wake widths w/c and small density parameter ρ^* (see Figure 7 and Figure 8). This scaling is given by,

$$\frac{Cy_{max} - Cy_{mean}}{Cy_{mean}} = 2.19 \left(\frac{w}{c} \right) \rho^* \quad (5)$$

$$\frac{Cm_{max} - Cm_{mean}}{Cm_{mean}} = -3.05 \left(\frac{w}{c} \right) \rho^* \quad (6)$$

⁴Smaller density ratios are associated with larger density gradients which generate stronger vorticity and higher v_f .

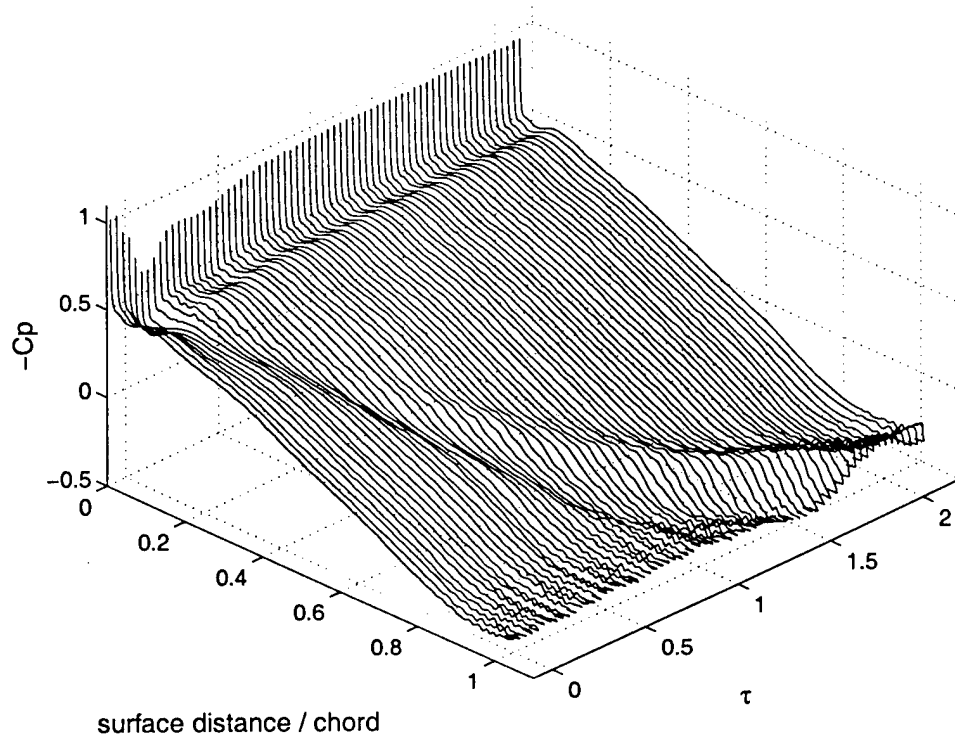


Figure 5: Suction surface pressure distribution during passage of a density wake width $0.2c$ and density ratio 0.5.

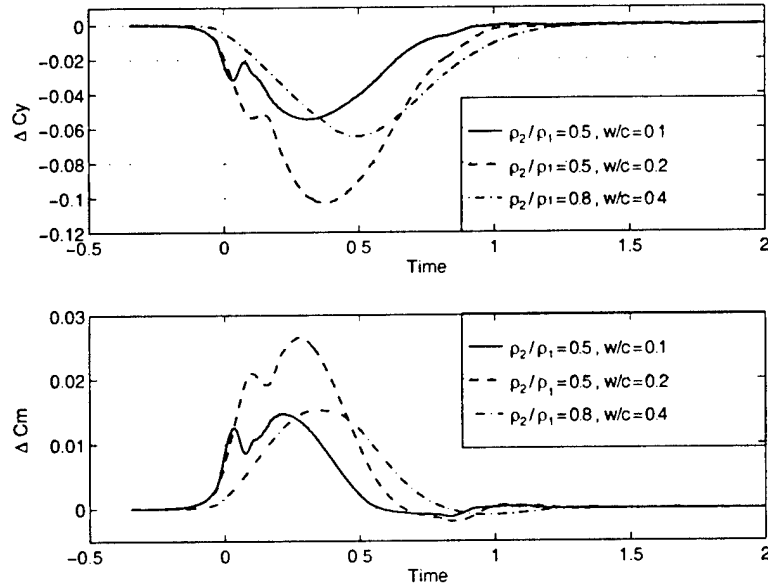


Figure 6: Fluctuation in (a) azimuthal force coefficient and (b) moment coefficient (positive counter-clockwise about the mid-chord) during passage of density wakes. $\Delta C_y = C_{y_{max}} - C_{y_{mean}}$, $\Delta C_m = C_{m_{max}} - C_{m_{mean}}$ where $C_{y_{mean}} = 0.75$, $C_{m_{mean}} = -0.13$. Reproduced from Ramer.

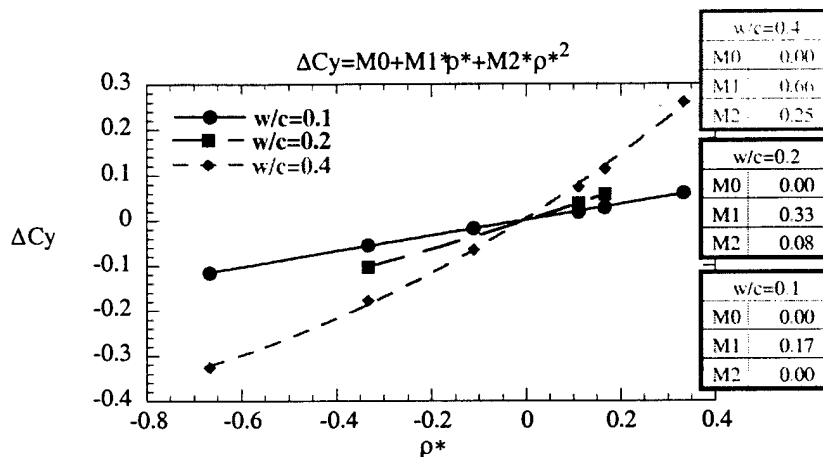


Figure 7: Maximum fluctuation in the azimuthal force coefficient (from steady state) during passage of density wakes through the NACA4F blade row. $\Delta C_y = (C_{y_{max}} - C_{y_{mean}})/C_{y_{mean}}$. Reproduced from Ramer.

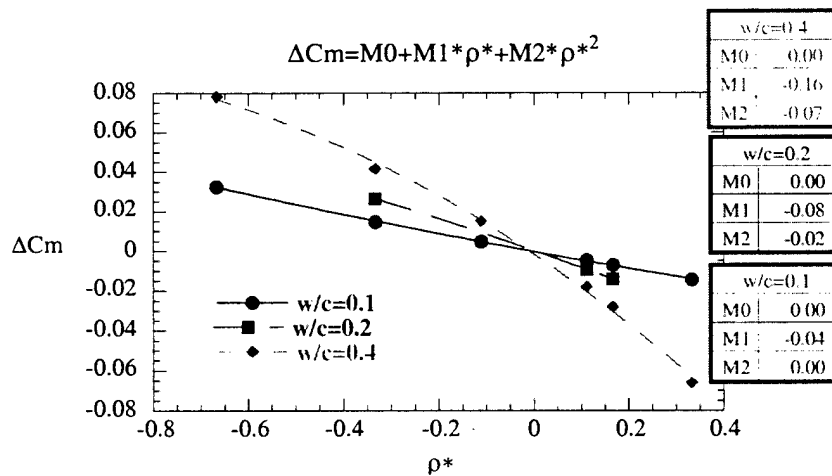


Figure 8: Maximum fluctuation in moment coefficient (from steady state) during passage of density wakes through the NACA4F blade row. $\Delta C_y = (C_{y_{max}} - C_{y_{mean}})/C_{y_{mean}}$. Reproduced from Ramer.

5.1 Conclusions

- The passage of density wakes through a compressor blade row results in a time varying fluctuation in the blade force and moment coefficients. This fluctuation is a result of the localized reduction of static pressure difference across the blade due to a flux of density wake fluid to the blade surface. During passage of low density wakes the wake fluid is directed toward the blade suction surface. This reduces the blade force coefficient and increases the counter-clockwise moment coefficient. The opposite is true during passage of a high density wake. In this case the wake fluid is directed toward the blade pressure surface.
- Parametric studies show the amplitude of the maximum fluctuation in blade force and moment coefficients to have the following functional relationship:
$$\Delta Cy = f(w/c, \rho^*, Cy(mean))$$
$$\Delta Cm = f(w/c, \rho^*, Cm(mean))$$
The effect of blade spacing h/c is included in $Cy(mean)$ and $Cm(mean)$.
- The shape of the force and moment coefficient fluctuations are common over the range of density wake widths $0.1 \leq w/c \leq 0.4$ and density ratios $0.25 \leq \rho_2/\rho_1 \leq 2.0$ considered.
- For $w/c \leq 0.2$ and $-0.2 \leq \rho^* \leq 0.2$, ΔCy and ΔCm scale linearly. Increasing non-linearity is observed for larger wake widths and density ratios.

| Convective Time Scale (τ) | Location of density wake |
|----------------------------------|---------------------------------|
| 0.0 | wake l.e. intercepts blade l.e. |
| 0.1 | wake t.e. intercepts blade l.e. |
| 1.3 | wake t.e. passes blade t.e. |

Table 1: The location of a density wake at different times during passage through the LSRC cascade blade row. $w/c = 0.2$, $\rho_2/\rho_1 = 0.50$, $M_\infty = 0.15$.

6 Results From The Viscous Flow Simulations

The viscous flow simulations were conducted at Reynolds number $Re(U_\infty, c) \approx 700,000$ and Mach numbers ranging from $M_\infty = 0.15$ to $M_\infty = 0.87$. The purpose of these simulations was to investigate the impact of blade boundary layers and blade passage shock waves on the density wake blade row interaction. The important features of the viscous flow simulations are best described using the time varying blade force and moment profiles shown in Figure 9. The force and moment profiles can be divided into 3 different regions depending on the position of the density wake within the blade passage (see Table 1). The characteristic flow features in each response region are summarized below.

1. Baseline response region. This response corresponds to all times when the density wake is upstream of the compressor blade leading edge. The force and moment fluctuations observed here are a consequence of vortex shedding⁵.
2. Primary response region. This response corresponds to when the density wake is within the cascade blade passage. The characteristic flow features here are the fluid flux directed to the blade surfaces and the associated counterrotating vortices⁶. For flow at $M_\infty = 0.87$ blade passage shock wave fluctuations are also observed.
3. Secondary response region. This response corresponds to all times after the density wake leaves the cascade blade trailing edge. A separation bubble is observed on the blade suction surface during this response⁷.

6.1 Vortex Shedding From Cascade Blade Rows

The baseline response vortex shedding was observed for Reynolds numbers in the range $Re(U_\infty, c) = 600,000 - 800,000$. A summary of the force and moment fluctuation amplitudes and frequencies are included in [26]. Experimental results from Lawaczeck and Heinemann [16], Boldman et.al. [3] and Parker [19] have indicated vortex shedding at similar flow conditions and from similar cascade geometries.

⁵Note vortex shedding is a result of the viscous flow environment and is not a consequence of the passage of density wakes.

⁶Note these are the same features as for inviscid incompressible flows.

⁷A qualitative description of this flow feature has been included in the September 1998 Progress Report [26].

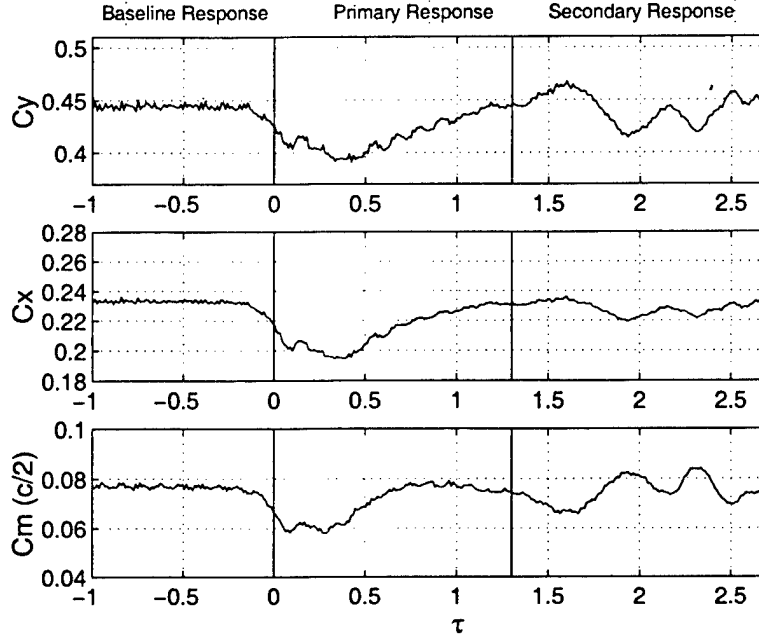


Figure 9: Fluctuations in (1) azimuthal force coefficient, (2) axial force coefficient and (3) moment coefficient (positive clockwise about the mid chord) during passage of a density wake of width $0.2c$ and density ratio $\rho_2/\rho_1 = 0.5$. 3 distinct regions can be identified in the response. $M_\infty = 0.15$.

6.2 Primary Response Force And Moment Fluctuations

The time varying blade force and moment fluctuations for the viscous flow simulations are plotted in Figure 54 through Figure 105 in Section 16. The magnitude of the force and moment fluctuations are plotted separately in Figure 10 through Figure 13.

The change in magnitude the force and moment fluctuations with density wake width and density ratio (at a given flow Mach number) follow the same trends as the inviscid flow predictions, i.e. the magnitude increases with increase in both wake width and wake density ratio. This is as expected as the mechanism which consists of the fluid flux to the blade surface is responsible for the change in blade static pressure distribution for both viscous and inviscid flow simulations.

In the viscous flow simulations the vortex shedding induced force and moment fluctuations are superimposed on the density wake induced force and moment fluctuations. In most cases the maximum fluctuation in the primary response can be easily distinguished from the baseline response. However as the free stream Mach number increases the baseline fluctuations increase in magnitude and can sometimes exceed the primary response fluctuations. This is particularly true during the passage of density wakes with large density ratios ($\rho_2/\rho_1 = 0.75$) at high free stream Mach numbers. A clear distinction between the baseline response and the primary response cannot be seen for these cases. The maximum

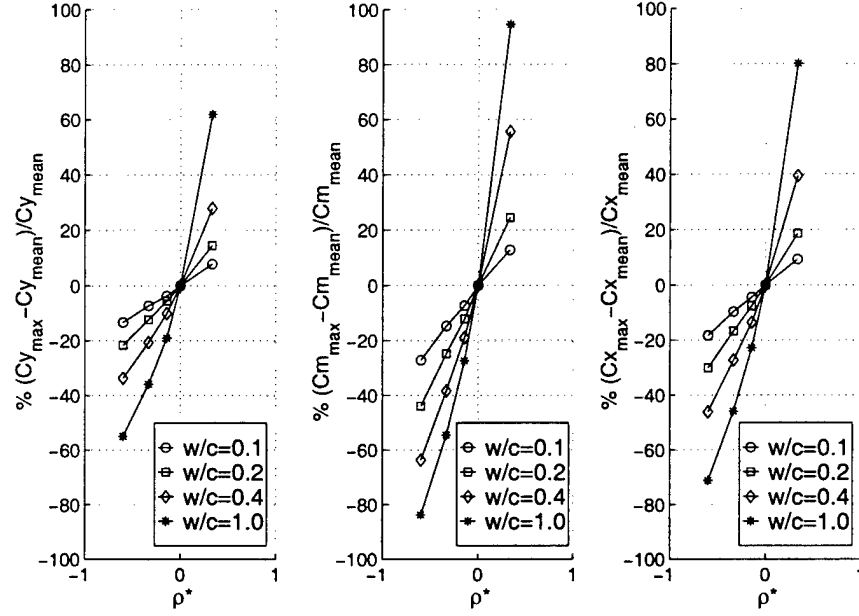


Figure 10: Maximum fluctuation in the force and moment coefficients as functions of density wake width and density parameter ρ^* . The straight lines joining data points are to help aid clarity. $M_\infty = 0.15$.

fluctuation in the primary response is nevertheless obtained by identifying the maximum (or minimum) point on the response curves corresponding to the time when the density wake is contained within the blade passage.

6.2.1 Compressibility Scaling

Comparison of the results in Figure 10 through Figure 13 show that in general the force and moment fluctuations for a given density wake width and density ratio to increase with freestream Mach number. This increase can be scaled using the Prandtl-Glauert compressibility factor as follows,

$$Cy_o(max) = Cy(max) \times \sqrt{1 - M_\infty^2} \quad (7)$$

$$Cx_o(max) = Cx(max) \times \sqrt{1 - M_\infty^2} \quad (8)$$

$$Cm_o(max) = Cm(max) \times \sqrt{1 - M_\infty^2} \quad (9)$$

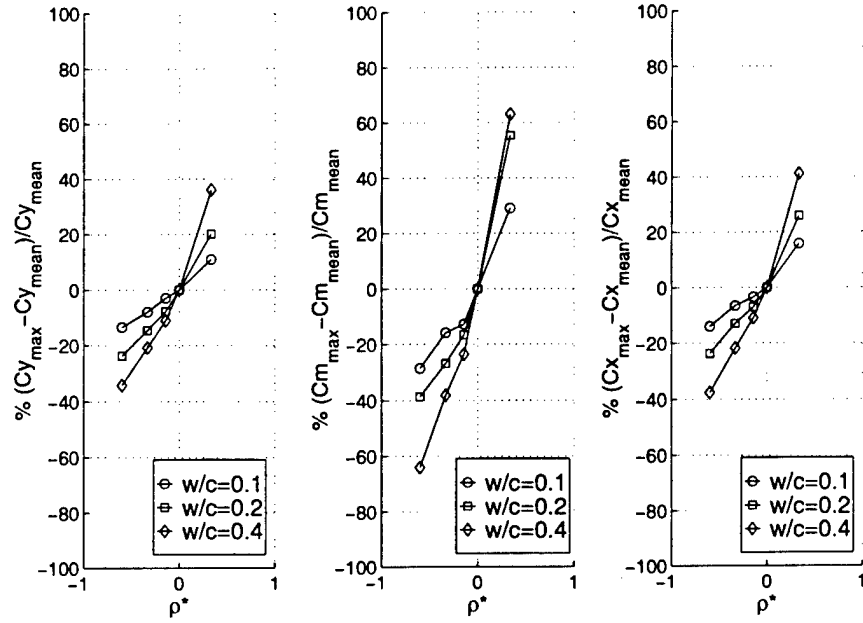


Figure 11: Maximum fluctuation in the force and moment coefficients as functions of density wake width and density parameter ρ^* . The straight lines joining data points are to help aid clarity. $M_\infty = 0.53$.

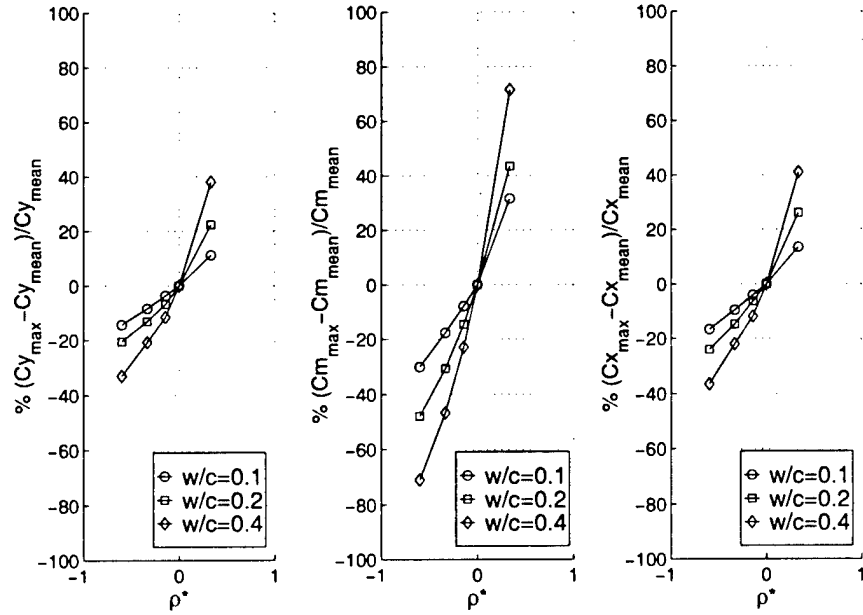


Figure 12: Maximum fluctuation in the force and moment coefficients as functions of density wake width and density parameter ρ^* . The straight lines joining data points are to help aid clarity. $M_\infty = 0.63$.

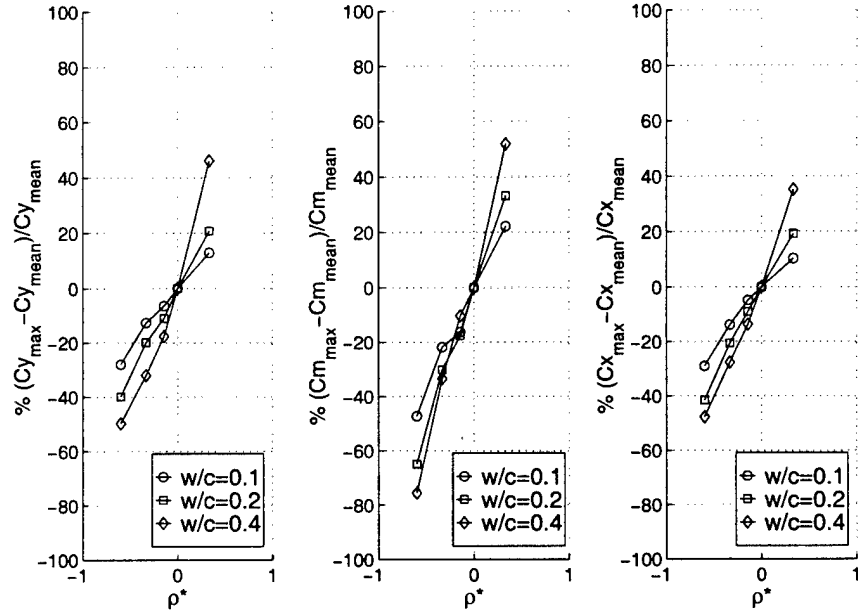


Figure 13: Maximum fluctuation in the force and moment coefficients as functions of density wake width and density parameter ρ^* . The straight lines joining data points are to help aid clarity. $M_\infty = 0.87$.

where the “o” subscript indicates the incompressible value. Figure 106 through Figure 117 in Section 17 compares the force and moment coefficients scaled in this manner at each Mach number. The following conclusions can be made from these plots.

- For wake widths of $0.1c$ the maximum fluctuation in the azimuthal force coefficient for all compressible tests compares to within 5% of the corresponding incompressible inviscid result. For wake widths of $0.2c$ the deviations from the incompressible result increase from 5% to a maximum of 20% for $|\rho^*| \geq 1/3$. Similarly for wake widths of $0.4c$ deviations of up to 40% can be seen for $|\rho^*| \geq 1/3$.
- For wake widths of $0.1c$ the maximum fluctuation in the axial force coefficient for $M_\infty = 0.53$, $M_\infty = 0.63$ and $M_\infty = 0.87$ deviates up to a maximum of 35% from the corresponding result at $M_\infty = 0.15$ for all ρ^* . For wake widths of $0.2c$ and $0.4c$ a deviation of more than 50% can be seen between the compressible results.
- For wake widths of $0.1c$ and $0.2c$ the maximum fluctuation in the moment coefficient deviates up to 35% between the $M_\infty = 0.15$ and the incompressible calculation. For wake widths of $0.1c$ there is a maximum deviation of 60% for $\rho^* < 0$ and a maximum deviation of 100% for $\rho^* > 0$. For larger wake widths the deviations exceed 100%.

Clearly the Prandtl–Glauert factor is not adequate to describe the compressibility effects on the maximum fluctuation in the force and moment coefficients. Deviations from this factor increase with increasing Mach number, increasing wake width and increasing density

ratio. Reasonable scaling for the azimuthal force coefficient can be achieved however for small wake widths ($w/c = 0.1$).

6.2.2 Shock Wave Fluctuations

The viscous flow simulation at $M_\infty = 0.87$ is characterized by a shock wave $0.25c$ downstream of the blade leading edge as shown in Figure 14.

The passage of a density wake through the blade row causes fluctuations in the position of the shock front. This in turn causes changes in the static pressure rise across the shock wave. The maximum deflection of the shock wave as a function of the density wake width and density parameter is plotted in Figure 15. During passage of low density wakes ($\rho^* < 0.0$) the shock front is initially displaced upstream towards the blade leading edge. As the density wake moves further aft the shock wave returns back towards the unperturbed position. Note for a high density wake (wake density higher than free stream density) the shock wave moves downstream. In general the shock wave displacement increases with density wake width and density parameter $|\rho^*|$. The maximum deflection of the shock wave is found to vary almost linearly for values of density parameter $\rho^* \leq -0.15$. The data points for density parameter $\rho^* = -0.60$ and wake widths $0.2c$ and $0.4c$ indicate the last recorded position of the shock wave before it is suppressed by the higher temperature (lower Mach number) within the density wake [26].

The effect of shock motion on (1) the static pressure rise across the shock and (2) the blade azimuthal force coefficient is illustrated in Figure 16. Notice the maximum reduction in azimuthal force coefficient corresponds to the point of maximum static pressure rise across the shock.

While there is additional contribution to changes in the blade static pressure distribution from the unsteady shock wave motion, this contribution is such that the blade force and moment fluctuation magnitudes increase with density wake width and density ratio. Hence there is no change in the trends for the force and moment fluctuations between flows with shock waves and without shock waves.

6.3 Secondary Response Force And Moment Fluctuations

The magnitude of the secondary response fluctuations depend on the fluctuation of the suction surface flow separation point. This fluctuation in separation point is due to the formation and subsequent downstream convection of the separation bubble. The maximum upstream motion of the separation point is plotted in Figure 17 through Figure 20 for varying density wake widths and density ratios for each Mach number flow. In general the separation point moves further upstream as the wake density ratio decreases (for a high density wake, $\rho_2/\rho_1 > 1$, the separation point moves further upstream as the density ratio increases). An increase in density wake width also drives the separation point further

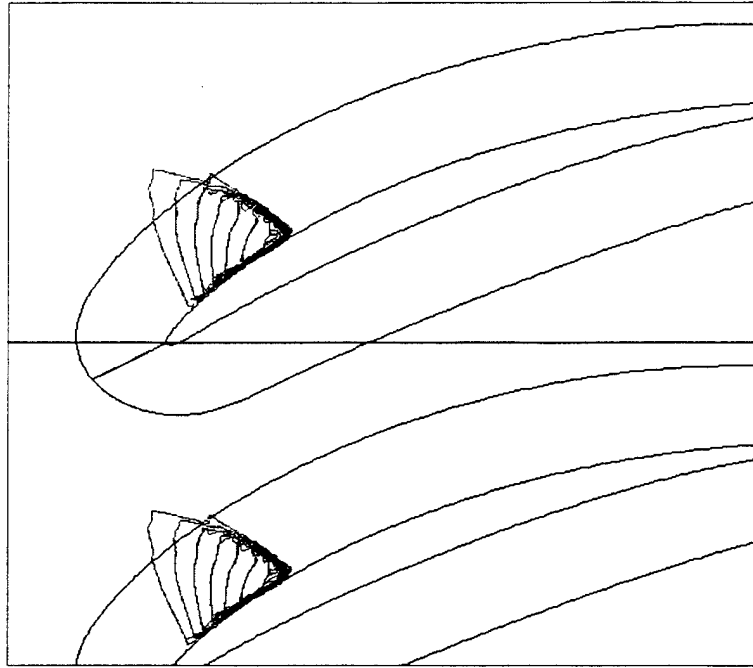


Figure 14: Mach number contours indicating extent of supersonic region in Run 4. Contours range from $M = 1.0$ to $M = 1.5$ in steps of 0.05. $M_\infty = 0.87$.

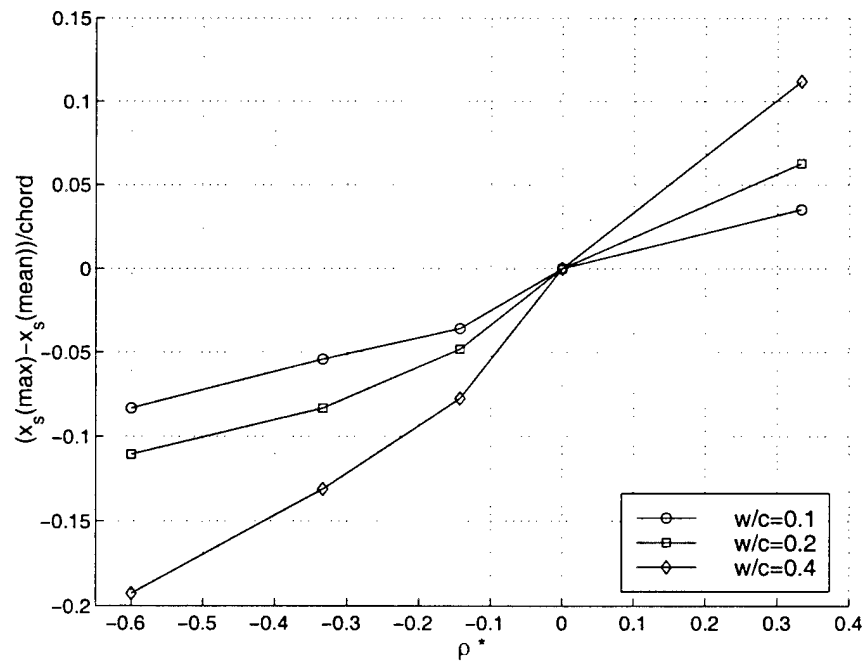


Figure 15: Changes in the maximum deflection of the shock wave as a function of the density wake width w/c and density parameter ρ^* .

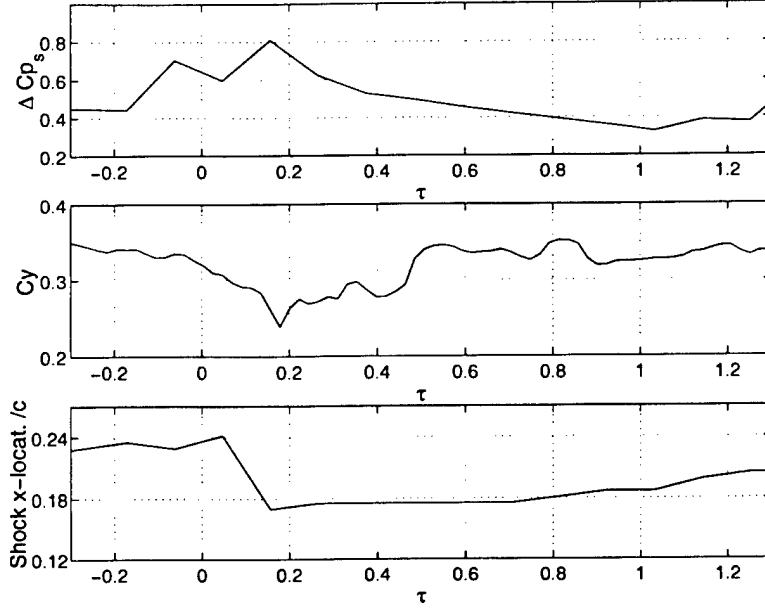


Figure 16: The change in (1) static pressure difference across the shock wave, (2) azimuthal force coefficient and (3) blade shock location during passage of a density wake width $0.1c$ and density ratio 0.25. $M_\infty = 0.87$.

upstream however there is an upper limit ($w/c = 0.2$) beyond which further increase in density wake width does not further effect the separation point motion. This is particularly evident in the $M_\infty = 0.15$, $M_\infty = 0.53$ and $M_\infty = 0.63$ results for density ratios $\rho_2/\rho_1 < 1$.

The magnitude the secondary response force and moment fluctuations are plotted in Figure 21 through Figure 24 for varying density wake widths and density ratios. The following conclusions can be made from these plots.

- The magnitude of the force and moment fluctuations follow the same trends as the separation point fluctuation with changes in density wake width and density ratio. Note how the curves for wake widths of $0.2c$ and $0.4c$ almost collapse together. This corresponds to the same trend observed for the separation point fluctuation in Figure 17 through Figure 20. This shows a clear link between the separation point motion and the magnitude of the secondary response fluctuations.
- The magnitude of the secondary fluctuations normalized by the baseline fluctuation magnitudes decrease with increasing free stream Mach number. This however is a consequence of the increased magnitude of baseline fluctuations with increased Mach number. In general the secondary fluctuations for all coefficients without normalization increases with Mach number.

The formation of a separation bubble on the blade suction surface temporarily suppresses the vortex shedding at the blade trailing edge. This results in a lack of high frequency con-

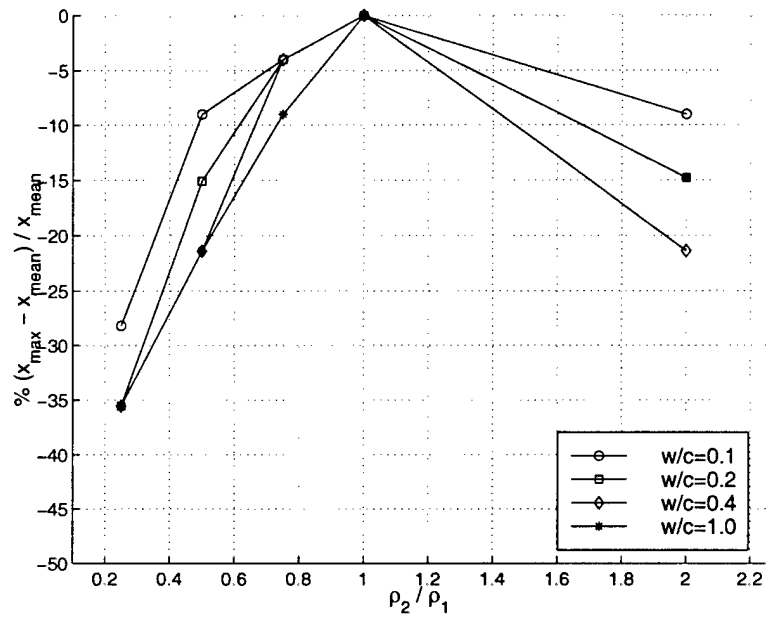


Figure 17: The maximum change in the suction surface separation point from the mean baseline position as a function of wake width and density ratio. $M_\infty = 0.15$

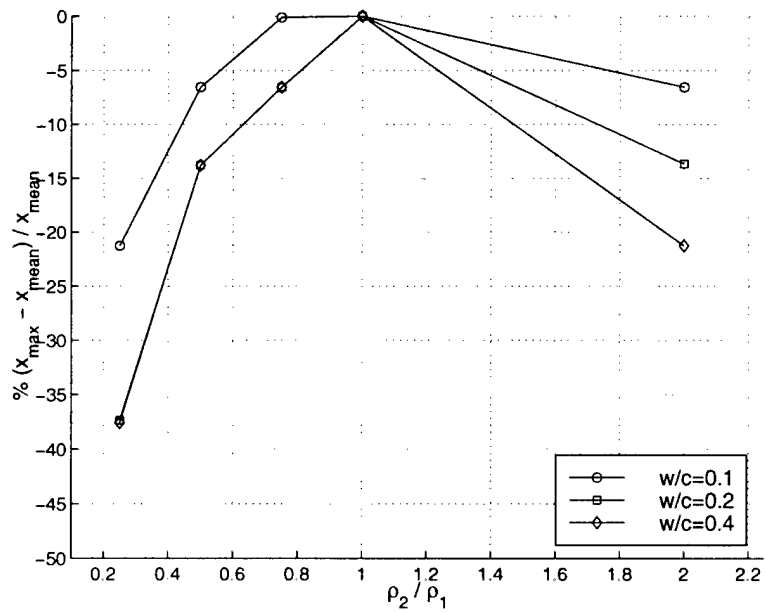


Figure 18: The maximum change in the suction surface separation point from the mean baseline position as a function of wake width and density ratio. $M_\infty = 0.53$.

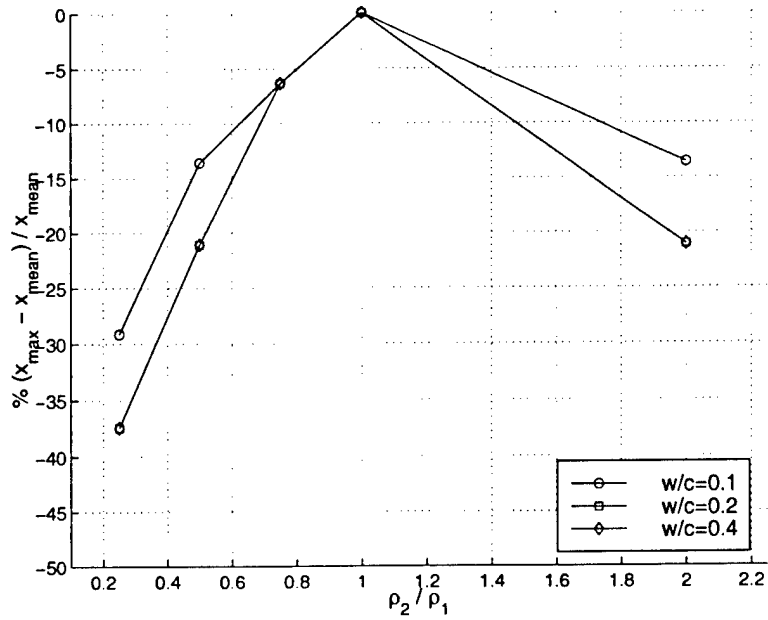


Figure 19: The maximum change in the suction surface separation point from the mean baseline position as a function of wake width and density ratio. $M_\infty = 0.63$.

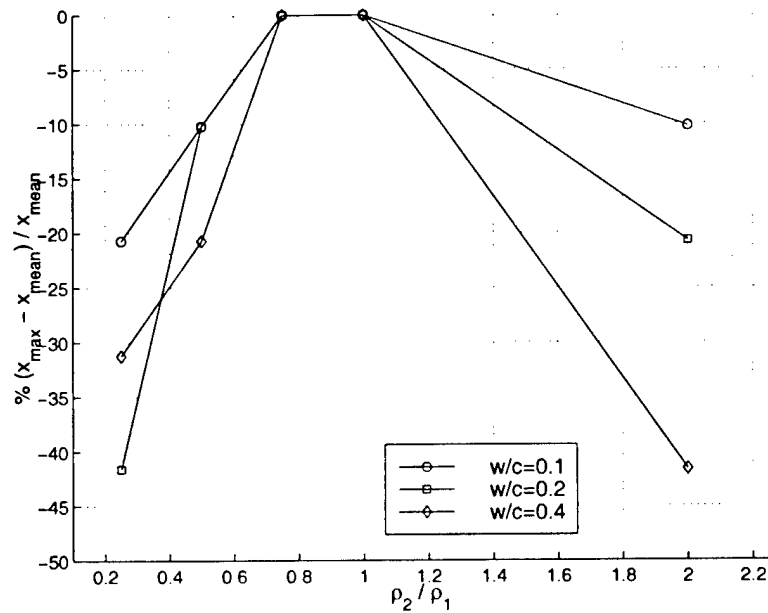


Figure 20: The maximum change in the suction surface separation point from the mean baseline position as a function of wake width and density ratio. $M_\infty = 0.87$.

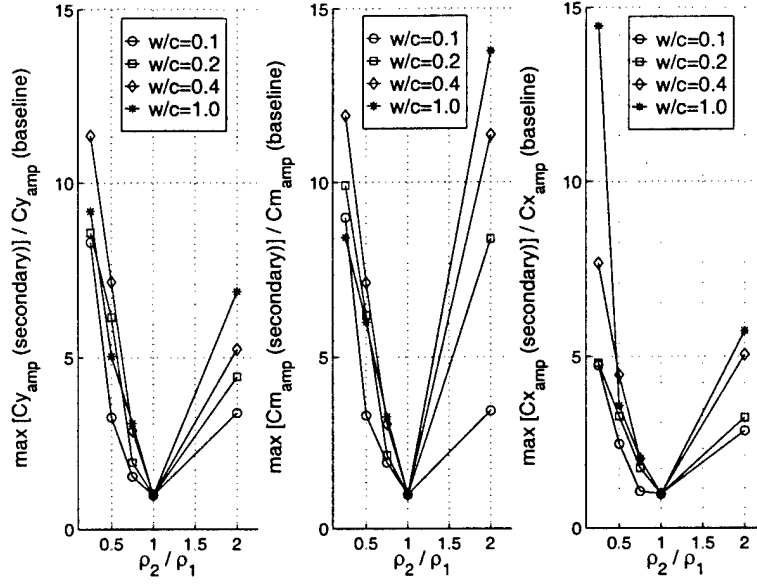


Figure 21: The maximum fluctuation in the blade azimuthal force, axial force and moment coefficients in the secondary response region for varying density wake widths and density ratios. $M_\infty = 0.15$.

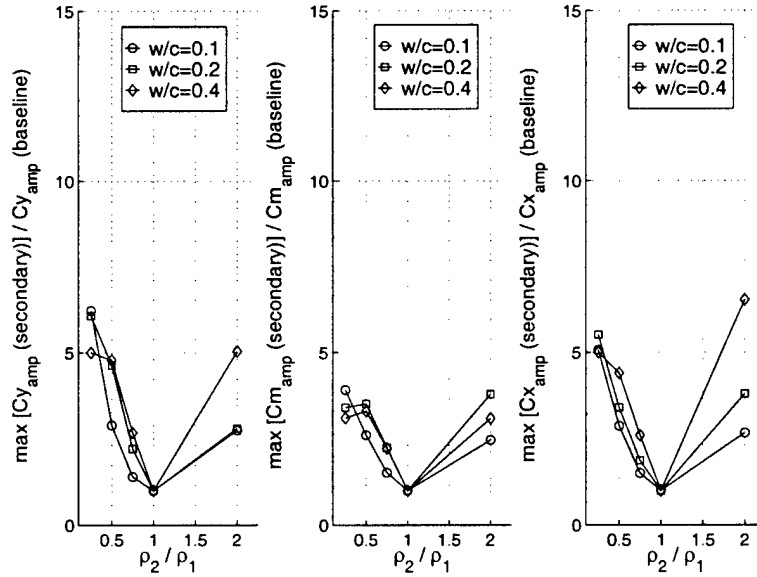


Figure 22: The maximum fluctuation in the blade azimuthal force, axial force and moment coefficients in the secondary response region for varying density wake widths and density ratios. $M_\infty = 0.53$.

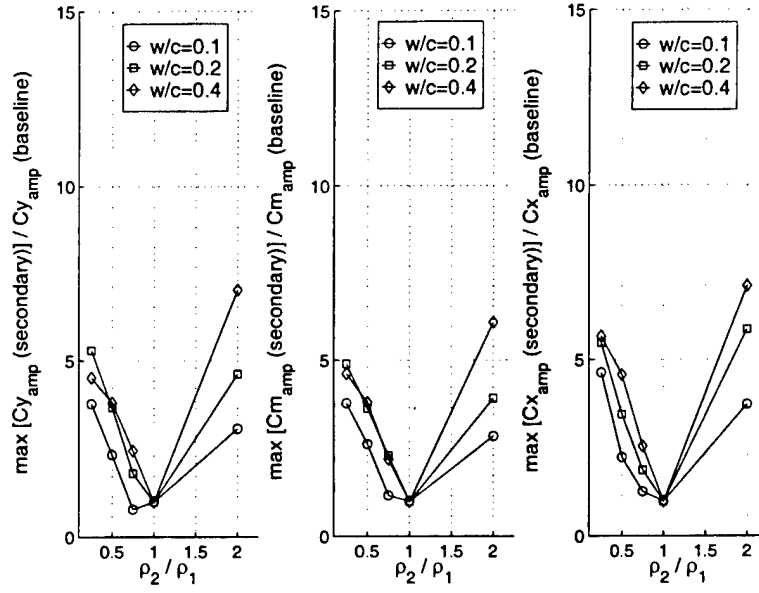


Figure 23: The maximum fluctuation in the blade azimuthal force, axial force and moment coefficients in the secondary response region for varying density wake widths and density ratios. $M_\infty = 0.63$.

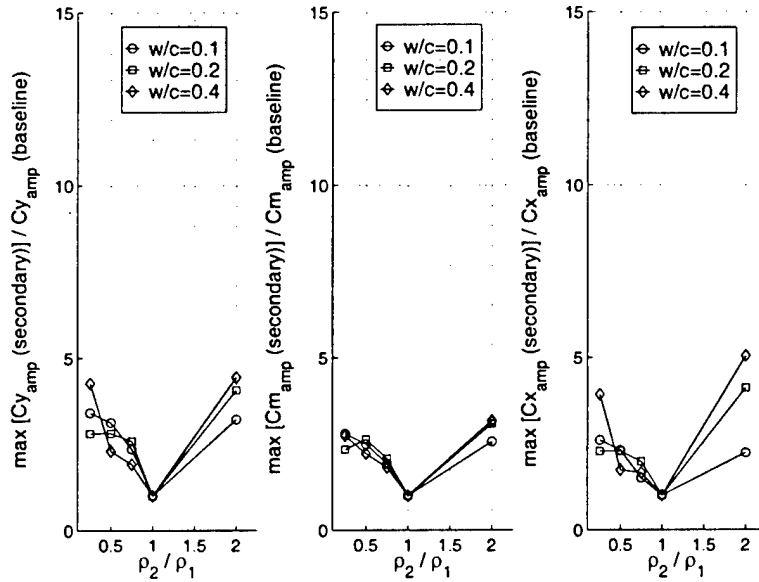


Figure 24: The maximum fluctuation in the blade azimuthal force, axial force and moment coefficients in the secondary response region for varying density wake widths and density ratios. $M_\infty = 0.87$.

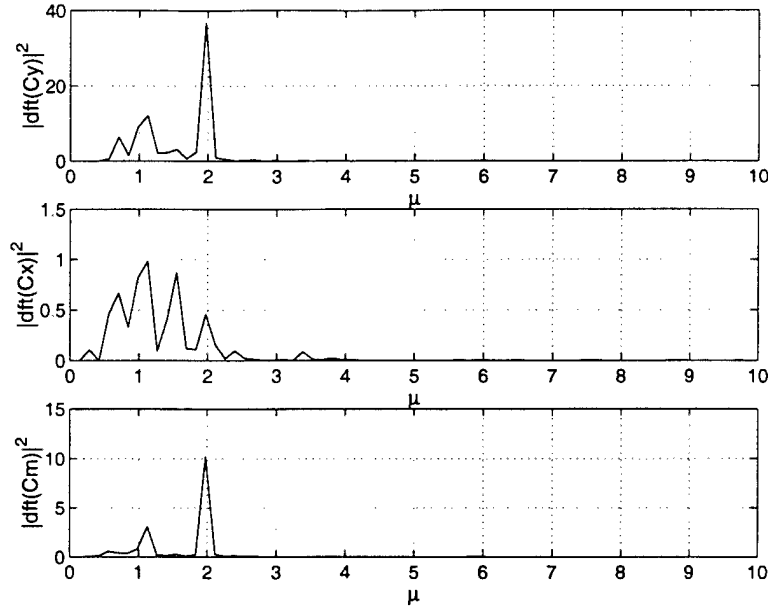


Figure 25: Discrete fourier transform of the baseline force and moment coefficients. $dft(X)$ is the discrete fourier transform of the time signal X . μ = non-dimensional frequency. $M_\infty = 0.87$.

tent in the force and moment fluctuations. This is evident by comparing the frequency spectrum plots obtained separately for the baseline response region (Figure 25) and the secondary response region (Figure 26). Visual examination of the time histories of the force and moment fluctuations for all the parametric tests (Figure 54 through Figure 105 in Section 16) also indicates this result.

6.4 Conclusions

- The cascade blade force and moment fluctuations observed in viscous compressible flows can be divided into 3 main regions based on the position of the density wake:
 1. The baseline response. This corresponds to when the density wake is upstream of the blade leading edge.
 2. The primary response. Response when the density wake is contained within the blade passage.
 3. The secondary response. Response after the density wake leaves the blade trailing edge.
- The baseline response is a consequence of vortex shedding at the blade trailing. The frequency of blade force and moment fluctuations are found to correspond with the vortex shedding frequency and the magnitude is found to increase with flow Mach number [26].

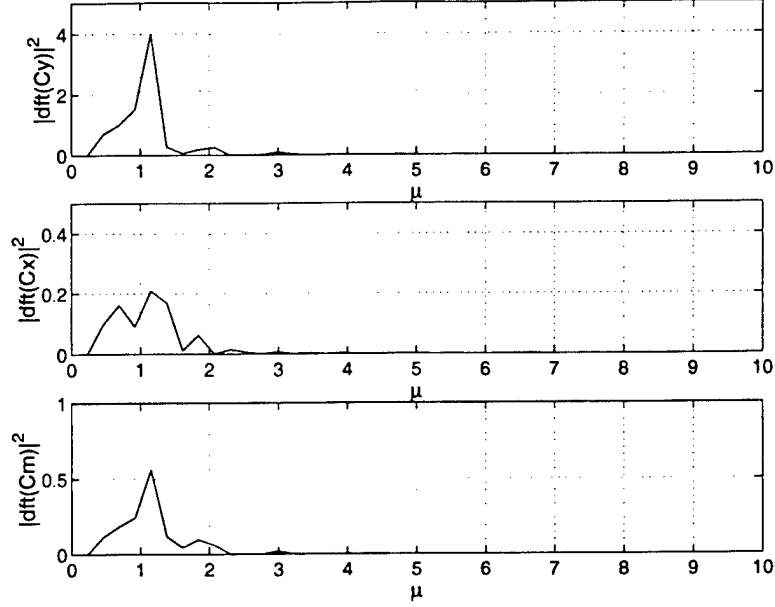


Figure 26: Discrete fourier transform of the secondary response force and moment coefficient fluctuations. $w/c = 0.2$, $\rho_2/\rho_1 = 0.5$, $M_\infty = 0.87$. $dft(X)$ is the discrete fourier transform of the time signal X . μ = non-dimensional frequency.

- The magnitude of the primary response force and moment fluctuations scale with the magnitude of the fluid flux directed to the blade surfaces (similar to the inviscid flow force and moment fluctuations). At $M_\infty = 0.87$ shock wave deflection is also found to contribute towards the force and moment fluctuations. The magnitude of the fluid flux and the deflection of the shock wave both scale with (1) the non-dimensional density wake width w/c and (2) the density parameter ρ^* . The trends for the maximum fluctuation in the force and moment coefficients in viscous flows (primary response) are therefore identical to the trends observed in the inviscid flows.
- The magnitude of the primary response force and moment fluctuations increase with flow Mach number. For small density wake widths ($w/c = 0.1$) the magnitude of the azimuthal force coefficient fluctuations are found to scale with the Prandtl-Glauert compressibility correction factor $\sqrt{1 - M_\infty^2}$.
- The magnitude of the force and moment fluctuations in the secondary response are typically 2–10 times larger than the vortex shedding induced baseline fluctuations. These additional fluctuations are caused by a separation bubble on the blade suction surface formed by the density wake – boundary layer interaction. The magnitude of these fluctuations scale with the maximum fluctuation in the blade suction surface separation point which in turn scales with (1) the normalized density wake width w/c and (2) the density ratio ρ_2/ρ_1 .
- The separation bubble is found to temporarily suppress vortex shedding for 2–3 con-

vective time scale units after the density wake has left the blade trailing edge. The vortex shedding frequencies are consequently absent in the frequency response of the secondary fluctuations.

7 Cascade Flow Model

CFD flow solvers are useful for investigating specific fluid flow phenomena however they are less useful for conducting parametric studies. This is due to the excessive computational run-times involved⁸. Furthermore investigation of changes in flow geometry is tedious as a new computational grid must be generated for each simulation. A simple flow model which incorporates the essential fluid dynamic features can however greatly reduce the time required to determine parametric trends and can also help assess the relative importance of flow geometry variables on a specific output variable.

A cascade flow model was therefore developed in this study in parallel with the CFD simulations to help determine the density wake induced blade force and moment fluctuations in an economical manner. The results from the viscous compressible CFD simulations in particular indicate a variety of fluid phenomena associated with the passage of density wakes; these cannot be easily modeled at the present time. As a first step we develop a simple model aimed at characterizing trends in the force and moment fluctuations for inviscid incompressible flows only. The assumptions and equations used in the model are presented below together with the results from a parametric analysis. The source code for the model is listed in Section 18.

7.1 Modeling Assumptions

The model is focused on the density wake induced force and moment fluctuations in inviscid incompressible background flows. A combination of potential flow singularity solutions and a constant of proportionality determined from the inviscid CFD results is used to develop the model. In addition the model uses “quasi-steady aerodynamic” assumptions and is therefore at best valid for low reduced frequencies ($\mu < 1.0$ [4]). The following additional assumptions are made to further simplify the model:

1. The flow is two dimensional.
2. The cascade blades are unstalled so the flow always follows the blade surface.
3. Effects due to blade camber and thickness are neglected so that the cascade blades can be represented as flat plates.
4. The density wake can be represented as a row of counterrotating vortices which convect with the mean flow.
5. The influence of shed vorticity can be neglected in the transient response.

A schematic of the model is shown in Figure 27. The basic approach involves solving for the bound vorticity on the cascade flat plates such that the flow remains tangent to the

⁸The investigation of time-accurate flow phenomena in particular requires extensive computational resources.

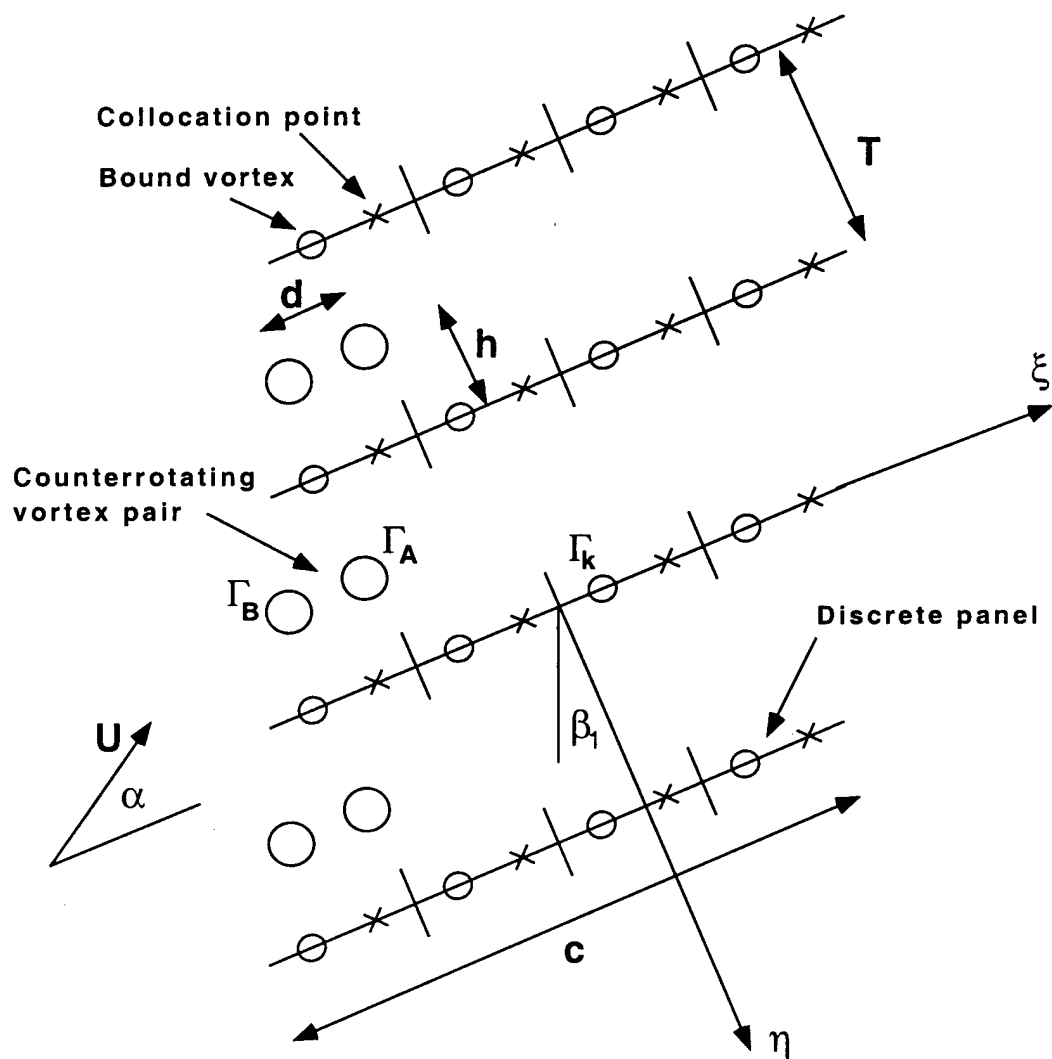


Figure 27: Model schematic indicating flat plate cascade and counterrotating vortex pairs.

plate surface. The flat plates are divided into N discrete panels each with a bound vortex at the $1/4$ chord location. There are no changes in the bound vortex circulation strength on similar panels on different plates (i.e. zero interblade phase angle). The flow tangency condition is applied at the $3/4$ chord location of each panel. The cascade flat plates are inclined at stagger angle β_1 and have space-chord ratio σ . The free stream velocity is inclined at an angle α to the flat plates.

The convecting density wake is modeled by a row of counterrotating vortex pairs. This approach is motivated from the inviscid CFD flow visualization results which indicate the formation of counterrotating vortex pairs as the density wake interacts with the cascade pressure field (see Figure 4). The counterrotating vortices are staggered at angle β_1 (equal to the blade stagger angle) and are convected parallel to the flat plates at a fixed vertical offset h . The density wake width is represented by the spacing d of the counterrotating vortices. The circulation Γ_A and Γ_B associated with each of the vortices in the counterrotating vortex pair is prescribed as a function of space and time.

7.2 Induced velocities

As stated above the basic approach used in the model involves solving for the circulation strength of each flat plate vortex panel such that the flow tangency condition is satisfied on the blade surface. The first step in this approach requires the evaluation of the induced velocity field of (1) the bound vortices and (2) the convecting counterrotating vortex pairs. For the case of an isolated flat plate the velocity $w(\text{airfoil})$ induced by a single bound vortex of circulation strength Γ at a distance r from the vortex is given by,

$$w(\text{airfoil}) = \frac{\Gamma}{2\pi r} \quad (10)$$

For the case of a cascade of flat plates with bound vorticity at N discrete vortex panels the induced velocities from a row of vortices extending from $-\infty$ to $+\infty$ must be summed. The velocity $w(\text{cascade})$ induced at any location ζ by a row of vortices strength Γ_k located at the same relative position ξ on a discrete vortex panel k , is given by

$$w(\text{cascade}) = \frac{-i\Gamma_k}{2T} e^{i\beta_1} \coth \left(\pi \frac{\zeta - \xi}{T} e^{i\beta_1} \right) \quad (11)$$

where β_1 is the plate stagger angle and T is the plate spacing. This expression is derived in Kaufmann [12]. The real and imaginary parts of Equation 11 yield the induced velocity in directions parallel to and normal to the flat plate. For the counterrotating vortices which convect a distance h above the flat plate, an equivalent expression can be obtained for the induced velocities. The velocity field $w(\text{vortices})$ induced by the front row of vortices in the

counterrotating pair (Figure 27) each with circulation strength Γ_A and stagger angle β_1 is given by,

$$w(\text{vortices}) = \frac{-i\Gamma_A}{2T} e^{i\beta_1} \coth \left\{ \left(\pi \frac{\zeta - \xi}{T} + i\pi h \right) e^{i\beta_1} \right\} \quad (12)$$

7.2.1 Circulation Strength of The Counterrotating Vortices

The circulation strength of the vortices in the counterrotating pair is assumed to be a function of the vorticity ω (of the vortex), an effective area A_{eff} , and time τ , i.e.

$$\Gamma = f(\omega, A_{eff}, \tau) \quad (13)$$

The vorticity ω is assumed to change from zero to a fixed magnitude as the vortices convect through the cascade. This change in vorticity is governed by the interaction of the wake density gradient and the blade pressure gradient according to Equation 1. A hyperbolic tangent functional approximation is assumed to represent this change in vorticity. By interchanging the time dependency τ with the vortex position ξ (by assuming a constant convection speed) the change in counterrotating vortex circulation strengths Γ can now be expressed as,

$$\Gamma = 0.5 \times \Gamma_{max} \times (1 + \tanh(s_1\xi + s_2)) \quad (14)$$

where Γ_{max} is a constant dependent on the density wake properties and the cascade pressure distribution. The variables s_1 and s_2 are chosen such that the \tanh function varies between -3 and $+3$ as the counterrotating vortex location ξ varies between predetermined end points l_1 and l_2 . These end points are obtained by considering the upstream and downstream decay of the cascade pressure field as a function of the blade row stagger angle, space-chord ratio and blade leading edge radius. For values of ξ less than l_1 the circulation strengths are set to zero while for values greater than l_2 the circulation strengths are set to Γ_{max} . The -3 to $+3$ range of the \tanh function is chosen to ensure a smooth transition of Γ_A and Γ_B to the fixed end values (see Figure 28).

Γ_{max} in Equation 14 is assumed to contain the influence of the blade row pressure gradient and the density gradient together with an effective area as follows,

$$\Gamma_{max} = f(\nabla p, \nabla \rho, A_{eff}) \quad (15)$$

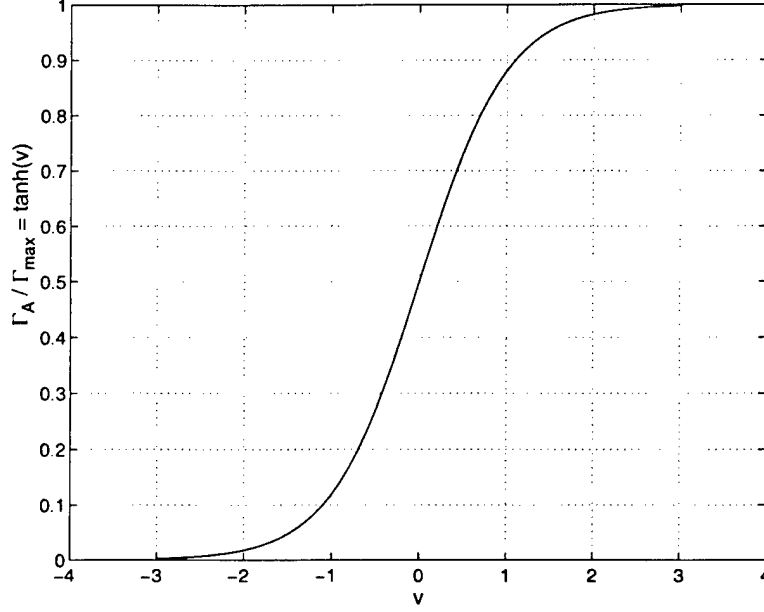


Figure 28: Change in circulation strength of the convecting vortices. $v = s_1\xi + s_2$ where ξ is the location of the convecting vortex and s_1 and s_2 are constants which ensure the \tanh function is evaluated between -3 and $+3$.

In the simplest case the functional relation for Γ_{max} , ∇p , $\nabla \rho$ and A_{eff} is assumed to be linear, i.e.

$$\Gamma_{max} = K \frac{(Cp_s - Cp_p)}{T} \frac{(\rho_2 - \rho_1)}{d/2} \times (A_{eff}) \quad (16)$$

where Cp_s and Cp_p are the plate suction surface and pressure surface pressure coefficients⁹. A_{eff} is set equal to $T \times d/2$ and K is a constant of proportionality to be determined from the inviscid CFD results. Once K is fixed the value of Γ_{max} is determined purely by the cascade geometry and density wake parameters.

7.3 Solution Procedure

The bound vortex circulation strengths Γ_k at each discrete vortex panel k and the induced velocities F_k from the forcing terms (described shortly) at each panel $3/4$ chord location are related by an aero-influence coefficient matrix A as follows,

$$\{F\} = [A] \{\Gamma\} \quad (17)$$

⁹($Cp_s - Cp_p$) is evaluated at the plate $1/4$ chord location.

The A matrix stores the vertical component of velocity induced at the 3/4 chord location $\zeta(k)$ of each panel by the bound vortex of strength Γ_k at each panel 1/4 chord location $\xi(k)$. The A matrix can be obtained by substituting appropriate values for ζ and ξ in Equation 11 for a given cascade space-chord ratio and stagger angle.

The forcing vector F_k contains (1) the vertical component of the free stream velocity U_n and (2) the velocity induced by the counterrotating vortex pairs at the panel 3/4 chord locations. The F_k vector is constantly updated as the counterrotating vortex pairs convect through the cascade. The velocity induced by the counterrotating vortices at the plate leading edge is also added to F_k ¹⁰.

The unknown values of the panel bound vortex strengths Γ_i can now be evaluated by inverting the aero-influence coefficient matrix A as follows,

$$\{\Gamma\} = [A]^{-1} \{F\} \quad (18)$$

The cascade lift (force normal to the flat plate along the $-\eta$ direction)¹¹ and the moment (clockwise positive about the plate mid-chord) is then obtained using,

$$L = \rho U \sum_{k=1}^N \Gamma_k \quad (19)$$

$$M = \rho U \sum_{k=1}^N \Gamma_k \times \xi(k) \quad (20)$$

Note the influence of shed vorticity and the unsteady contribution to lift and moment from the unsteady circulation $d\Gamma_k/dt$ is not included in this model. The remaining sections describe the validation of the model and the parametric studies conducted with different density wakes and cascade geometries.

7.4 Steady State Model Validation

The steady state lift coefficient predicted by the model (i.e. with no convecting density wakes) is shown in Figure 29 for a range of cascade space-chord ratio's and stagger angles. The cascade lift coefficient $Cl_{cascade}$ shown here is normalized by the lift coefficient of an isolated flat plate airfoil $Cl_{airfoil}$. A single vortex panel is used in this case. All curves show an asymptotic value of 1.0 as the space-chord ratio is increased. This is as expected and confirms the cascade lift coefficient approaches the flat plate lift coefficient in the limit of

¹⁰This represents the influence of the counterrotating vortices on the free stream flow.

¹¹The term "lift" will be used subsequently instead of "force" to help indicate this direction.

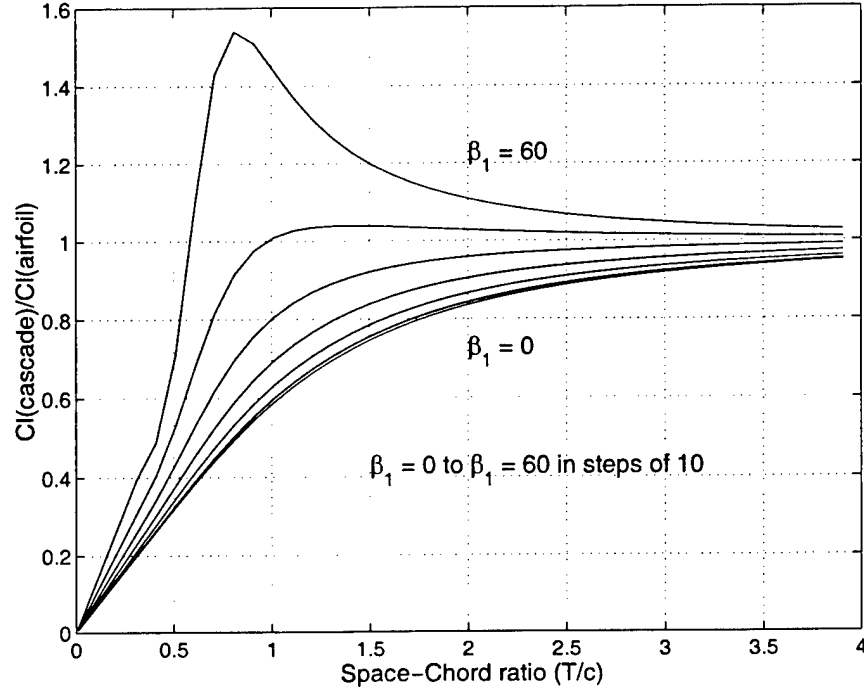


Figure 29: Cascade model results for the change in cascade interference coefficient $Cl_{\text{cascade}}/Cl_{\text{airfoil}}$ with space-chord ratio and stagger angle. No. of panels = 1.

large space-chord ratios. Also notice the large increase in cascade lift coefficient for stagger angles $\beta_1 > 45$ degrees and space-chord ratio $\sigma \approx 1.0$. This is due to the increased flow restriction between the adjacent flat plates at these high values.

The corresponding plot obtained using a conformal mapping method by Weinig [9] is shown in Figure 30. The overall trends compare well however the numerical values differ significantly at the higher stagger angles. Better agreement can be obtained using 5 vortex panels to represent the flat plates. The corresponding results shown in Figure 31 now compare to within 2% of Weinig's results¹². The model results for the steady state moment coefficient about the plate mid-chord location is plotted in Figure 32 normalized about the moment coefficient for an isolated airfoil. An equivalent theoretical prediction could not be found for comparison purposes for this case. The moment coefficient nevertheless approaches the thin airfoil predicted value in the limit of large space-chord ratio.

The results presented here confirm the model can adequately predict the numerical values and trends for the steady state cascade lift and moment coefficients. The model results for the quasi-steady lift and moment profiles induced by density wakes are discussed next.

¹²Results for stagger angles greater than 60 degrees could not be obtained using this model since the aero-influence coefficient matrix A becomes ill-conditioned and cannot be inverted.

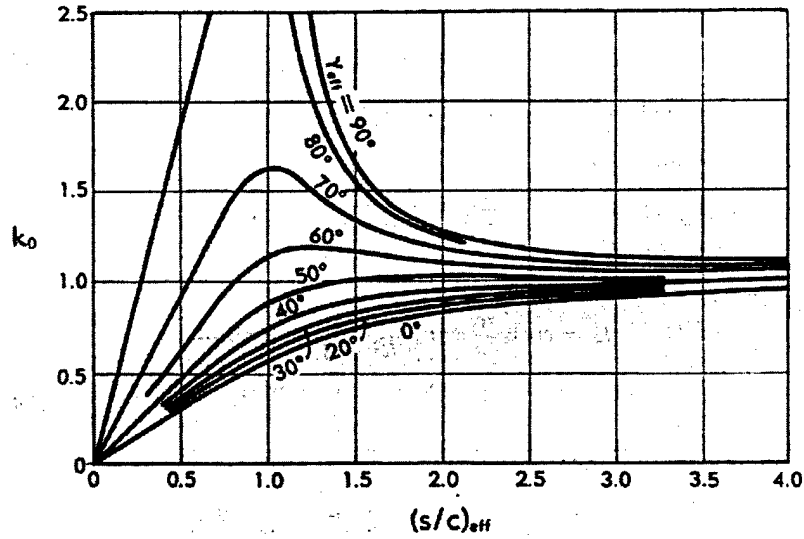


Figure 30: Weinig's conformal mapping prediction for the cascade interference coefficient k_0 ($Cl_{cascade}/Cl_{airfoil}$) as a function of stagger angle γ_{eff} and space-chord ratio $(s/c)_{eff}$.

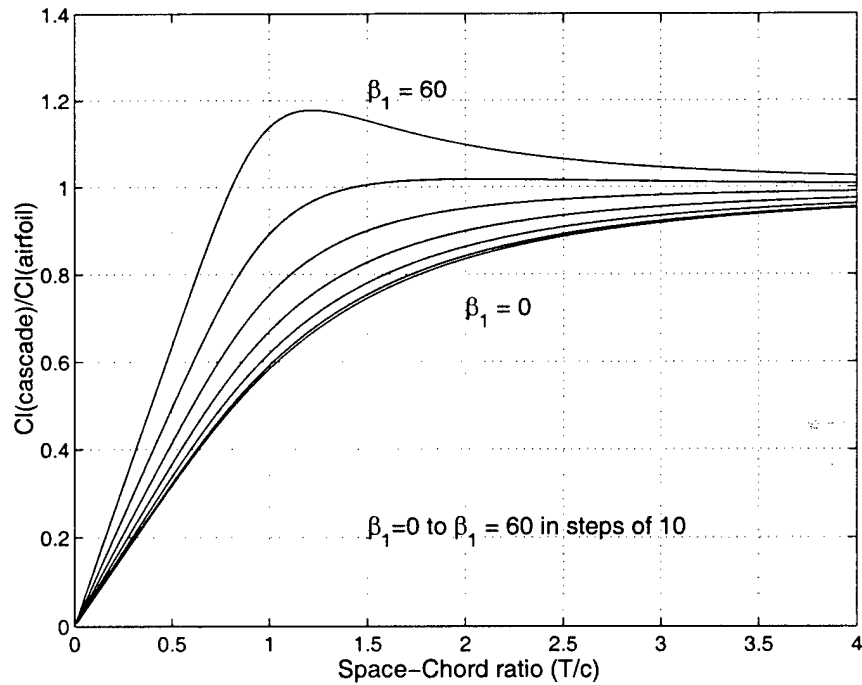


Figure 31: Cascade model results for the change in cascade interference coefficient $Cl_{cascade}/Cl_{airfoil}$ with space-chord ratio and stagger angle. No. of panels = 5.

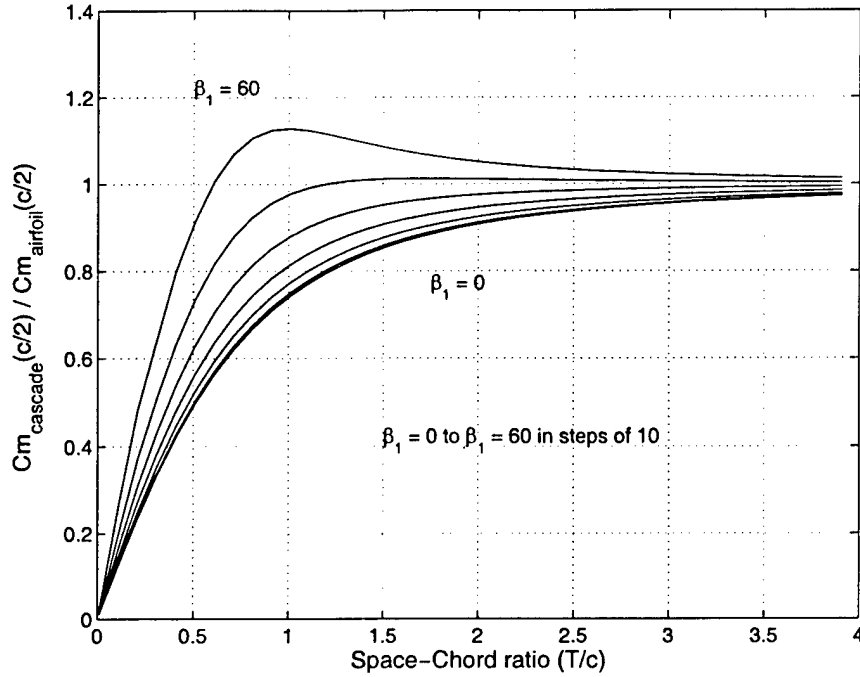


Figure 32: Cascade model results for the change in cascade interference coefficient $Cm_{cascade}/Cm_{airfoil}$ with space-chord ratio and stagger angle. No. of panels = 5.

| Property | Value |
|---------------------------|-----------|
| Space/chord ratio | 0.58 |
| Stagger angle | 15.0 deg. |
| Max. blade thickness | 0.037c |
| Blade leading edge radius | 0.0075c |

Table 2: Properties of the NACA4F cascade geometry used for the inviscid CFD tests.

7.5 Quasi-Steady Model Validation

The quasi-steady model validation involves comparison of the model prediction for the density wake induced flat plate lift and moment fluctuation with a corresponding inviscid CFD prediction. The model parameters are set to match the cascade geometry properties and density wake properties of a typical inviscid CFD calculation. For the cascade properties, a NACA4F blade geometry was chosen with properties listed in Table 2. For the density wake a width of $0.1c$ and density ratio 0.5 was considered a representative case. The model parameters corresponding to this set of cascade and density wake properties is listed in Table 3.

The model results and the inviscid CFD results for the force and moment fluctuations are compared in Figure 33. The dashed line represents the model prediction and the solid line represents the inviscid CFD prediction. The change in the lift and moment coefficients

| Variable | Value |
|--|---------------------------|
| Number of vortex panels (N) | 20 |
| Space/chord (s/c) | 0.58 |
| Cascade stagger angle (β_1) | 15.0 |
| Counterrotating vortex spacing (d) | $0.1c$ |
| Density ratio (ρ_2/ρ_1) | 0.5 |
| Upstream infl. of press. field (l_1) | $0.3c$ upstream of l.e. |
| Downstream infl. of press. field (l_2) | $0.4c$ downstream of l.e. |
| Incidence angle (α) | 5 deg. relative to blade |
| Circulation strength constant (K) | 0.32 |

Table 3: Cascade model parameters used to determine the flat plate force and moment coefficient fluctuation during passage of a density wake of width $0.1c$ and density ratio 0.5.

are shown as percentage changes from the steady state values. Note the definition for the model moment coefficient (positive clockwise about the mid-chord) was changed to positive counter-clockwise about the mid-chord for comparison purposes with the inviscid CFD results¹³. The maximum fluctuation in the model lift prediction is matched to the inviscid results by adjusting the value of the circulation constant K (Equation 16). 20 vortex panels are used to discretize the cascade flat plates for this case. Use of more than 20 panels is found to change the amplitude and frequency response by negligible amounts.

Significant deviation can be seen between the model and the inviscid CFD predictions. The maximum change in the lift response occurs at a time lag $\Delta\tau \approx 0.4$ after the corresponding maximum change in the inviscid CFD lift results. Similarly the maximum change in the moment occurs $\Delta\tau \approx 0.2$ before the corresponding maximum change in the inviscid CFD moment results. The initial decrease/increase in lift/moment compares well however the return to the steady state values does not compare. In addition the lift peak at $\tau = 0.1$ predicted by the model has a larger amplitude and occurs later than the similar peak predicted in the inviscid CFD results. The similar peak in the moment response is not captured by the model. Furthermore the overall maximum change in the moment is under predicted. The following list of model features have been highlighted as possible reasons for the observed discrepancies.

- The maximum change in the lift and moment coefficients occur as the density wake passes over the blade leading edge region. The blade leading edge geometry and corresponding pressure distribution pattern is therefore critical to the overall response profile. The model however replaces the finite blade radius with an infinite radius and consequently an infinite pressure peak. It may not be possible therefore to adequately capture the initial response shape with a flat plate geometry.

¹³ Also note the lift coefficient is defined normal to the flat plate whereas the force coefficient obtained from inviscid CFD simulations is defined along the azimuthal coordinate direction. The difference is absorbed into the model constant K .

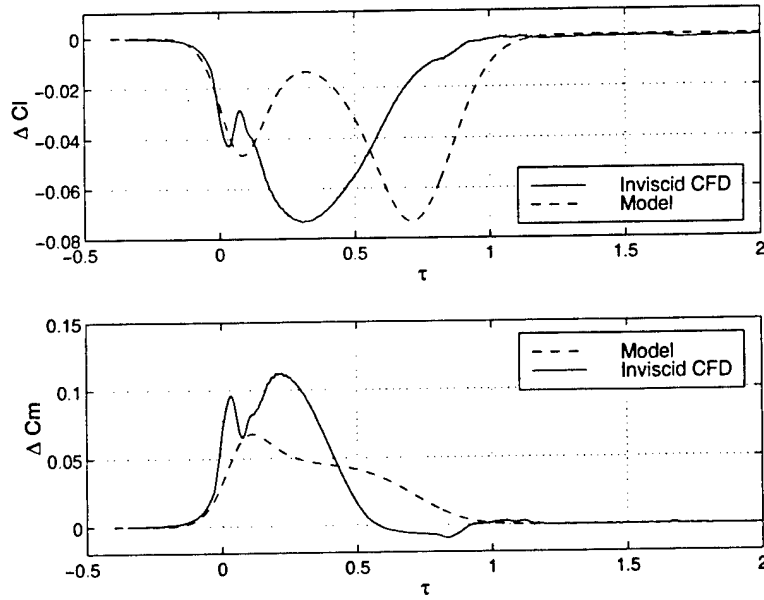


Figure 33: Comparison of the quasi-steady model results and the inviscid CFD results for the fluctuation in the blade force and moment coefficients during passage of a density wake of width $0.1c$ and density ratio 0.5 . $\Delta Cl = (Cl_{max} - Cl_{mean}) / (Cl_{mean})$, $\Delta Cm = (Cm_{max} - Cm_{mean}) / (Cm_{mean})$.

- The initial rise in the lift response curves was found to be governed by the induced velocity field of the clockwise vortex (vortex B) of the counterrotating vortex pair. The clockwise vortex induces an upwash velocity at the plate leading edge when it is located downstream of the plate leading edge. This results in an increase in the flow angle of attack and hence an increase in the lift coefficient. The model moment response does not capture this effect however. Since the moment is calculated about the plate mid-chord there must be a relative difference in induced velocity at the collocation points upstream and downstream of the mid-chord for a visible fluctuation in the moment to occur. The induced velocity of the clockwise vortex at the leading edge is however applied equally to all $3/4$ chord collocation locations on the vortex panels. There is little if no net difference in the moment therefore due to the increase in flow angle of attack. The induced velocity at the plate leading edge should therefore be weighted at the vortex panel collocation locations for improved comparison with the inviscid CFD results. This may also help to reduce the magnitude of the initial increase in the lift coefficient.
- The lag between the model and inviscid CFD results may be due to the influence of shed vorticity which is not accounted for in the model.

The sensitivity of the lift and moment response curves to changes in the density wake properties and the cascade geometry is examined next.

7.6 Parametric Results

7.6.1 Lift and Moment Sensitivity to Density Wake Properties

The NACA4F cascade geometry is used as the baseline geometry for the sensitivity analysis. The circulation constant K is fixed at 0.322. This sets the maximum fluctuation in lift coefficient to 7.3% and the maximum fluctuation in moment coefficient to -6.8% for a density wake of width $0.1c$ and density ratio 0.5 (see Figure 33).

The results for the maximum fluctuation in the lift and moment coefficients with varying density wake width and density ratio are plotted in Figure 34. The variation in density ratio is represented here by Marbles' density parameter ρ^* (Equation 2). The model data is indicated by markers joined by straight lines. The corresponding inviscid CFD results are shown superimposed as dashed lines. The model trends agree well with the inviscid CFD results. In particular the model values for the maximum fluctuation in azimuthal force coefficient compare to within 2% with the CFD numerical values for density parameter $\rho^* < 0$.

It is interesting to note how the model predicts the non-linearity in the maximum lift and moment fluctuations for large values of density parameter and wake width similar to the non-linearity observed in the inviscid CFD results. Initial investigations indicate the non-linearity to originate from the expressions for the counterrotating vortex circulation strengths¹⁴ (Equation 14).

7.6.2 Lift and Moment Sensitivity to Cascade Geometry

The density wake width and density ratio were held constant at $0.1c$ and 0.5 respectively as the cascade stagger and space-chord ratio were varied. The circulation constant K was again fixed at 0.322.

The results for the maximum fluctuation in the lift and moment coefficients with varying cascade space-chord ratio and stagger angle are plotted in Figure 35. The lift coefficient is more sensitive to the cascade space-chord ratio than to the stagger angle. This may be because the counterrotating vortices convect at the same stagger angle as the cascade¹⁵. The reduction in lift coefficient fluctuation as the space-chord ratio is increased is most likely due to the increased distance between the counterrotating vortices and the blade surfaces. The moment coefficient fluctuation also decreases with increasing space-chord ratio and shows greater sensitivity to the cascade stagger angle.

¹⁴ A systematic analysis of the model parameters can help to isolate the precise source of this non-linearity.

¹⁵ This is an assumption in the model.

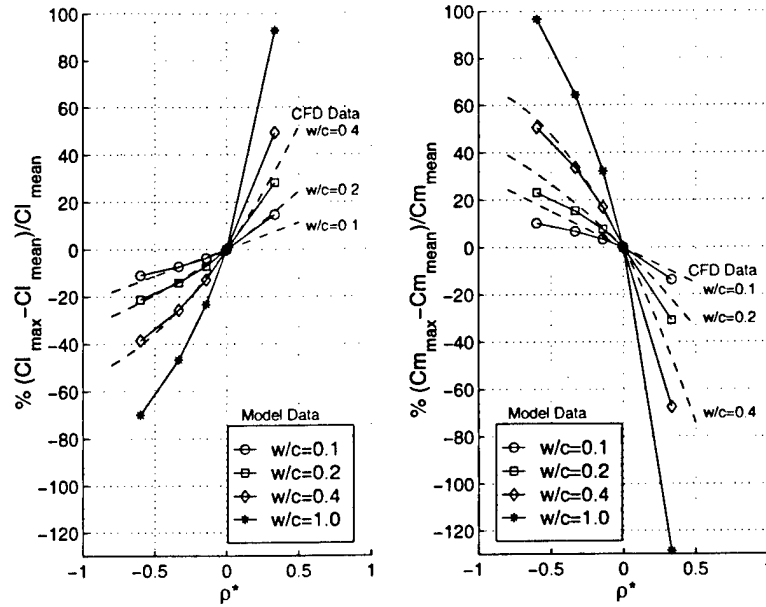


Figure 34: Cascade lift and moment fluctuation sensitivity to density wake width w/c and density parameter ρ^* (measure of density ratio). The NACA4F cascade geometry is used for all tests. Solid lines indicate the model results. Dashed lines indicate the inviscid CFD results.

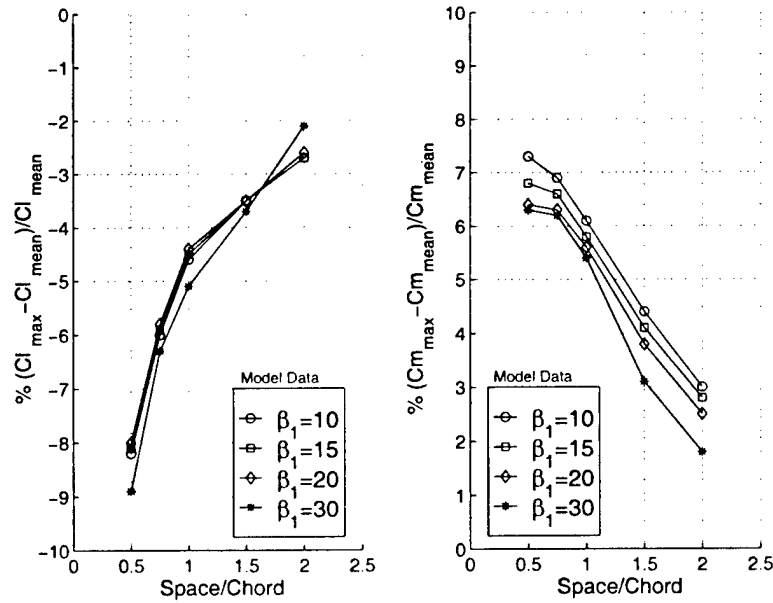


Figure 35: Cascade lift and moment sensitivity to cascade stagger angle and space-chord ratio. Density wake of width $0.1c$ and density ratio 0.5 is used for all tests.

7.7 Conclusion

A model to predict the density wake induced force and moment fluctuations on cascade blade rows has been described in this Section. The model is developed using the following main assumptions:

1. Effects due to blade camber and thickness can be neglected so that the cascade blades can be represented as flat plates.
2. The density wake can be represented as a row of counterrotating vortices which convect with the mean flow.
3. The influence of shed vorticity can be neglected.

The model predicts the maximum fluctuation in the lift and moment coefficients to (1) increase with density wake width, (2) increase with density parameter $|\rho^*|$, (3) decrease with increasing space-chord ratio and (4) remain relatively insensitive to blade stagger angle.

The model predicted trends for the force and moment fluctuations with varying density wake properties and fixed cascade geometry follow the same trends as the inviscid CFD results. Moreover for the case of density parameter $\rho^* < 0$ the numerical values for the maximum fluctuation in the lift coefficient agree to within 2% of the inviscid CFD predictions.

The model results for the moment coefficient however under predict the inviscid CFD results by up to 50%. The model does not adequately capture the extra length parameter (moment arm) required to determine the moment coefficient¹⁶. Thus the quasi-steady model while being instructive fails to match the unsteady characteristics.

¹⁶The assumptions in the model regarding the magnitude of the induced velocity at the vortex panel collocation points needs to be re-examined to determine the origin of this difference.

8 Overall Conclusions

The important conclusions from this study are listed below.

- The study of convecting density wakes through cascade blade rows have highlighted 4 distinct flow mechanisms which generate fluctuating blade forces and moments:
 1. The interaction of pressure gradients and density gradients to form counterrotating vortex pairs and concentrated fluid flux.
 2. Axial deflection of the blade passage shock wave position.
 3. Convecting separation bubbles.
 4. Vortex shedding.

The first 3 mechanisms are found to be excited by the passage of density wakes, the 4th mechanism is found to be temporarily suppressed by density wakes.

- The magnitude of the blade force and moment fluctuations generated by the above mechanisms are found to be characterized by a set of non-dimensional parameters based on density wake properties, flow Mach number and blade geometry:
 1. Density wake width w/c .
 2. Density parameter ρ^* .
 3. Density ratio ρ_2/ρ_1 .
 4. Prandtl Glauert compressibility factor $\sqrt{1 - M_\infty^2}$
 5. Blade spacing h/c .

The magnitude of the blade force and moment fluctuations have also been quantified using simple functional relationships.

- A simple cascade flow model has been developed to establish trends for the density wake - cascade blade row interaction. The model captures the trends for the variation of the blade force and moment coefficients as predicted by the inviscid CFD flow simulations. The model also shows the maximum fluctuation in the force and moment coefficients to (1) decrease with increasing cascade space-chord ratio and (2) remain relatively insensitive to blade stagger angle.

9 Personnel Supported

- Prof. Eugene E. Covert, T. Wilson Professor, Emeritus (MIT).
- Dr. Choon S. Tan, Principal Research Engineer (MIT).
- Prof. Frank Marble, Professor Emeritus (CalTech).
- Ms. B. Ramer, Research Assistant (MIT).
- Mr. H. Sanith Wijesinghe, Research Assistant (MIT).

10 Publications

- Ramer, B. E., "Aerodynamic Response of Turbomachinery Blade Rows to Convecting Density Distortions", S.M. Thesis, Massachusetts Institute of Technology, Department of Aeronautics and Astronautics, December 1996.
- Ramer, B. E., Wijesinghe, H. S., Tan, C. S., Covert, E. E., "Aerodynamic Response of Turbomachinery Blade Rows to Convecting Density Wakes". Proceedings of the ASME Aerospace Division, Presented at the International Mechanical Engineering Congress and Exposition, Dallas, Texas, AD-VOL.55, November 1997.
- Wijesinghe, H.S. "Aerodynamic Response of Turbomachinery Blade Rows to Convecting Density Wakes", S.M. Thesis, Massachusetts Institute of Technology, Department of Aeronautics and Astronautics, September 1998.

11 Interactions and Transitions

- USAF F-119 Ex. Review Group, August 1998.
- USAF ALC Review Group, July 1998.
- Lecture on "Aeromechanics" to Pratt & Whitney, Jan 1998, April 1998, July 1998, October 1998.

12 Inventions and Patents

None.

13 Honors and Awards

None.

References

- [1] *Basic Research Issues in Aerodynamics, Structural Dynamics and Control of High Cycle Fatigue*. Summary of a Workshop held at the Gas Turbine Laboratory, MIT, October 1995.
- [2] ANDERSON, J. D. JR. *Fundamentals Of Aerodynamics*. McGraw-Hill, Inc. 1991. pp. 542-545.
- [3] BOLDMAN, D. R., BRINICH, P. F., GOLDSTEIN, M. E. "Vortex Shedding From A Blunt Trailing Edge With Equal And Unequal External Mean Velocities". *Journal Of Fluid Mechanics*, Vol. 75, part 4, pp. 721-735.
- [4] CESNIK, C. E. S. Personal communication.
- [5] CHIENG, C. C. AND LAUNDER, B. E. "On the Calculation of Turbulent Heat Transport Downstream from an Abrupt Pipe Expansion". *Numerical Heat Transfer*, Vol. 3, 1980, pp.189-207.
- [6] COVERT, E. E. Personal Communication.
- [7] GILES, M. B. "Non-Reflecting Boundary Conditions for the Euler Equations". CFDL-TR-88-1, Computational Fluid Dynamics Laboratory, Massachusetts Institute of Technology, February 1988.
- [8] GOSTELOW, J. P. *Cascade Aerodynamics*. Pergamon Press Ltd. 1984. pp. 171-172.
- [9] HAWTHORNE, W. R. (ED.) *Aerodynamics Of Turbines And Compressors*. Princeton University Press. 1964. pp. 32-34.
- [10] HEINEMANN, H. J. AND BUTEFISCH, K. A. "Determination of the Vortex Shedding Frequency of Cascades with Different Trailing Edge Thickness". AGARD CP-227, Paper 35 (1978).
- [11] HOYING, D. A. "Blade passage Flow Structure Effects On Axial Compressor Rotating Stall Inception ". PhD. Thesis, Massachusetts Institute of Technology, Department of Aeronautics and Astronautics, September 1996.
- [12] KAUFMANN, W. *Fluid Mechanics*. McGraw-Hill Book Company, Inc., 1963, pp.354-356.
- [13] KEMP, N. H. AND SEARS, W. R. "The Unsteady Forces Due to Viscous Wakes in Turbomachines". *Journal of Aeronautical Sciences*, Vol.22, No.7, July 1955, pp.478-483.
- [14] KERREBROCK, J. L. AND MIKOLAJCZAK, A. A. "Intra-Stator Transport of Rotor Wakes and its Effect on Compressor Performance". *ASME Paper 70-GT-39*, 1970.

- [15] LAUNDER, B. E. AND SPALDING, D. B. *Computer Methods in Applied Mechanics and Engineering*. Vol. 3. 1974. pp. 269-289.
- [16] LAWACZECK, O. AND HEINEMANN, H. J. "Von Karman Vortex Streets in the Wakes of Subsonic and Transonic Cascades". AGARD CP-177, Paper 28 (1976)
- [17] MANWARING, S. R. AND WISLER, D. C. "Unsteady Aerodynamics and Gust Response in Compressors and Turbines". *ASME Paper 92-GT-422*, 1992.
- [18] MARBLE, F. E. "Response of a Thin Airfoil Encountering a Strong Density Discontinuity". *Journal of Fluids Engineering*, Vol. 115, December 1993, pp.580-589.
- [19] PARKER, R. "An Investigation Of Acoustic Resonance Effects In An Axial Flow Compressor Stage". *Journal of Sound and Vibration*, Vol. 8, pp. 281-297.
- [20] PERAIRE J. Personal communication.
- [21] PLATZER, M. F. "Unsteady Flows In Turbomachines - A Review of Current Developments". AGARD CP-227, Paper 33 (1978).
- [22] RAMER, B. E. "Aerodynamic Response of Turbomachinery Blade Rows to Convecting Density Distortions". S.M. Thesis, Massachusetts Institute of Technology, Department of Aeronautics and Astronautics, December 1996.
- [23] RAMER, B. E., WIJESINGHE, H. S., TAN, C. S., COVERT, E. E. "Aerodynamic Response of Turbomachinery Blade Rows to Convecting Density Wakes". *Proceedings of the ASME Aerospace Division*, Presented at the International Mechanical Engineering Congress and Exposition, Dallas, Texas, AD-VOL.55, November 1997.
- [24] STEGER, J. L. AND SORENSON, R. L. "Automatic Mesh-Point Clustering Near a Boundary in Grid Generation with Elliptic Partial Differential Equations". *Journal of Computational Physics*, Vol. 33, 1979, pp.405-410.
- [25] TAM, C. K. W. AND WEBB J. C. "Dispersion-Relation-Preserving Finite Difference Schemes for Computational Acoustics". *Journal of Computational Physics*, Vol. 107, 1993, pp.262-281.
- [26] TAN, C.S. "Aerodynamic Response of Turbomachinery Blade Rows to Convecting Density Wakes". Third progress report for AFOSR contract no. F49620-94-1-0202, September 1998.
- [27] VALKOV, THEODORE V. "Control of Unsteady Flow in a Stator Blade Row Interacting with Upstream Moving Wakes". S.M. Thesis, Massachusetts Institute of Technology, Department of Aeronautics and Astronautics. Also GTL Report No. 255, May 1992.
- [28] WIJESINGHE, H. S. "Aerodynamic Response of Turbomachinery Blade Rows to Convecting Density Wakes". Final report for AFOSR Contract No. F49620-94-1-0202, MIT Gas Turbine Lab, December 1997.

- [29] WILLIAMSON, C.H.K. AND ROSHKO, A. "Vortex Formation In The Wake Of An Oscillating Cylinder". *Journal of Fluids and Structures*, Vol.2, July 1988, pp.355-381.
- [30] WISLER, D. C. "Core Compressor Exit Stage Study, Volume I - Design Report". NASA CR-135391, NASA Lewis Research Center, December 1977.

14 Viscous Flow Solver

A two-dimensional, time-accurate, explicit Navier-Stokes flow solver developed by Høyning [11] is used for all the viscous compressible flow simulations. The aim of this section is to briefly highlight the main features of this flow solver and to detail the computational grid and boundary conditions used to obtain converged solutions. The compressor cascade properties and the imposed shape of the density wake profiles is also detailed. The characteristic variables used to non-dimensionalize the results is also described. Details of the inviscid flow solver and computational grid can be obtained from Ramer [22].

14.1 Features of The Viscous Flow Solver

The key features of the Navier-Stokes flow solver are summarized below.

1. Finite difference discretization.
2. Fourth-order spatial accuracy and third-order temporal accuracy.
3. Dispersion Relation Preserving (DRP) scheme (Tam and Web [25]).
4. k - ϵ turbulence model.
5. Wall functions (Chieng and Launder [5]).
6. Non-reflecting inlet and exit boundary conditions (Giles [7]).

The Dispersion Relation Preserving scheme used in this solver has the advantage of optimizing the dissipation and dispersion characteristics of the finite difference method over a large number of wavelengths (than say a four-stage Runge-Kutta scheme). The resulting high-order scheme also reduces the computational cost by requiring fewer grid points. As is the case with most high-order methods, the presence of high frequency waves in the solution is of great concern. The scheme is noted as being able to capture high frequency waves to an extent that unwanted waves will remain in the solution. Artificial damping based on the fourth derivative of pressure at each node however was found to be effective in removing the high-frequency waves without creating excessive damping of the desired waves. Specific implementation details are described in Høyning [11].

A standard two equation k - ϵ turbulence model was implemented in the solver using the following model constants,

$$C_\mu = 0.09, C_1 = 1.44, C_2 = 1.92, \sigma_\kappa = 1.0, \sigma_\epsilon = 1.3 \quad (21)$$

These constants as proposed by Launder and Spalding [15] are appropriate for free shear flows and flows near solid boundaries. A two-stage MacCormack Predictor-Corrector method is chosen to integrate the k - ϵ model equations. The flow equations and the k - ϵ model equations are advanced in time with the same time-step.

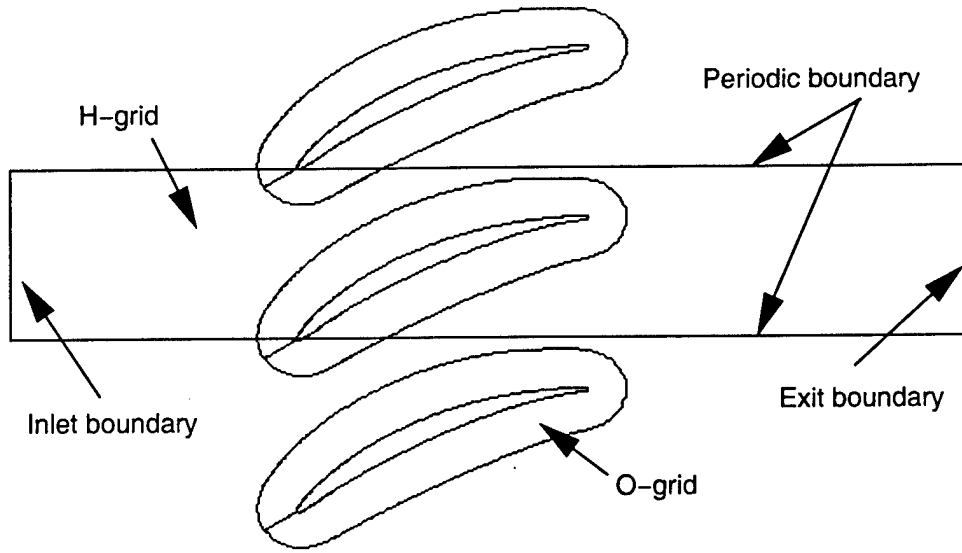


Figure 36: Schematic of the computational domain and boundary conditions.

Additional computational savings are achieved by using wall functions to model the inner portion of the blade boundary layers. Wall functions allow the first near wall grid point to be located at $y^+ \approx 30\text{--}150$. This results in a considerable saving of the number of near wall grid points. The wall functions calculate the wall shear stress and therefore a zero slip velocity at the wall cannot be specified as a boundary condition. A finite slip velocity is specified instead such that the correct wall shear stress is achieved ¹⁷. An adiabatic wall boundary condition is also applied at the blade surface.

The computational domain used in the solver is shown schematically in Figure 36. The flow upstream and downstream of the blade row is assumed to be governed by the Euler equations. The flow in the blade passages surrounding the blades is assumed to be governed by the Navier–Stokes equations. This division helps to reduce the computational time since the solution of the more expensive Navier–Stokes equations is confined to a physically smaller region of the flow.

Non-reflecting boundary conditions developed by Giles [7] are implemented at the inlet and exit boundaries of the computational domain. The aim of these boundary conditions are to allow all out-going modes of the solution to propagate through the inlet and exit boundaries without reflecting back into the computational domain. Periodic boundary conditions are employed along the side boundaries of the computational domain parallel to the axial flow direction. These boundary conditions are shown in Figure 36.

¹⁷See Hoying for more details.

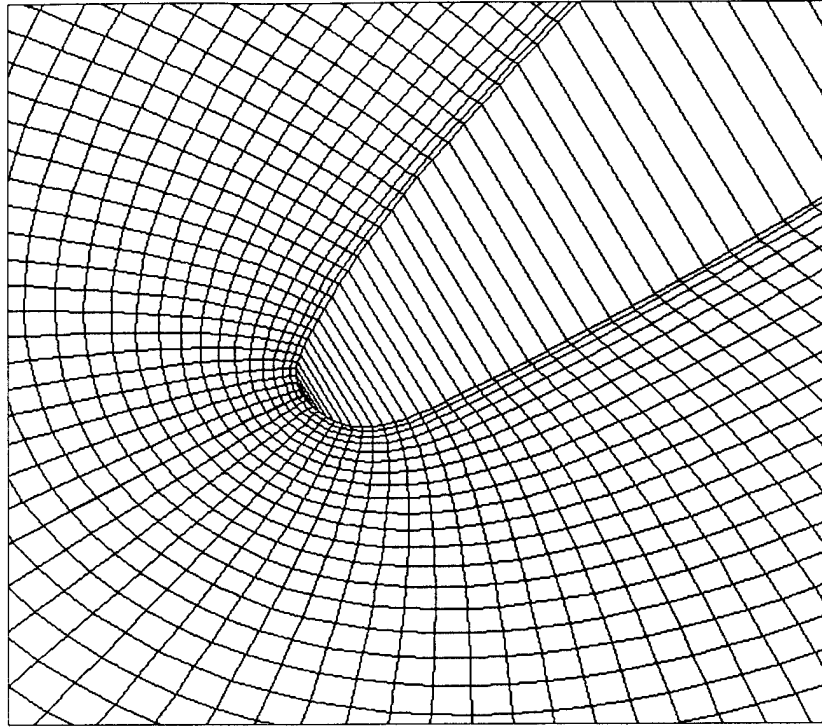


Figure 37: O-grid detail at the blade leading edge.

14.2 Computational Grid

The computational domain used in the solver consists of overlapping H and O grids as shown schematically in Figure 36. The H-grid has uniform spacing throughout the computational domain with a cell aspect ratio of 1.0. The orthogonality of the H-grid simplifies the evaluation of numerical derivatives as well as the H to O grid interpolation coefficients. The O-grid was generated using an elliptic partial differential equation method developed by Steger and Sorenson [24]. The O-grid detail near the blade leading edge and trailing edge is shown in Figure 37 and Figure 38. The grid cell aspect ratios obtained by this method are close to 1.0 near the blade leading and trailing edge. This is a typical “rule of thumb” value for grid cell aspect ratio in regions where the flow is not unidirectional [20]. The grid is also clustered closer at the blade surface and around the leading and trailing edge to help resolve the higher gradients in flow quantities in these regions. The Steger and Sorenson method also allows grid lines at the surface to be orthogonal to help simplify the evaluation of numerical derivatives. The grid is near-orthogonal in regions away from the surface.

The minimum grid resolution required to adequately capture flow features is a primary concern in any computational study. In the present study a detailed analysis of grid dependency was not conducted however. Instead the number of H-grid and O-grid nodes was increased until an upper limit was reached for the time required to achieve a converged

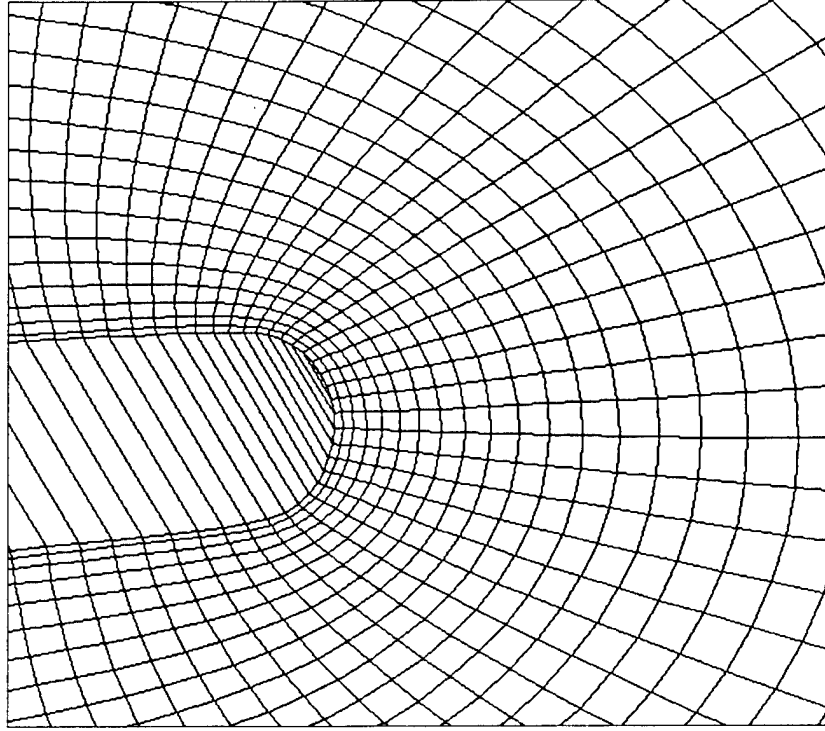


Figure 38: O-grid detail at the blade trailing edge.

solution (i.e. roughly equal to 3–4 weeks on a DEC Alpha workstation). The resulting O-grid consists of 421 nodes around the blade surface and 32 nodes radially outward from the blade surface. The H-grid consists of 161 nodes in the azimuthal direction and 1283 nodes in the axial direction.

14.3 Cascade Geometry and Blade Profile

The blade profile used in this study is the General Electric, Low Speed Research Compressor (LSRC) Stator-B blade. The 50% span section of this blade shown in Figure 39 is used for all the viscous flow simulations. The LSRC blade design is described in detail by Wisler [30]. The cascade geometry used for the viscous CFD simulations are listed in Table 4.

14.4 Density Wake Profile

A single density wake was convected through the cascade blade row in each simulation. The density wake, density variation is assumed to take a $(1 - \cosine)$ functional form. This ensures a smooth transition in density between the density wake and the free stream flow to help avoid possible numerical instabilities associated with step changes in flow properties.

| Cascade Geometry | Value |
|---------------------------|-----------|
| Chord/space ratio | 1.66 |
| Stagger angle | 24.5 deg. |
| Max. blade thickness | 0.071c |
| Blade leading edge radius | 0.007c |

Table 4: Properties of the LSRC cascade geometry used for the viscous CFD simulations. Experimental performance results from Wisler indicate a diffusion factor of 0.49 and a loss coefficient of 0.01 for this blade profile.

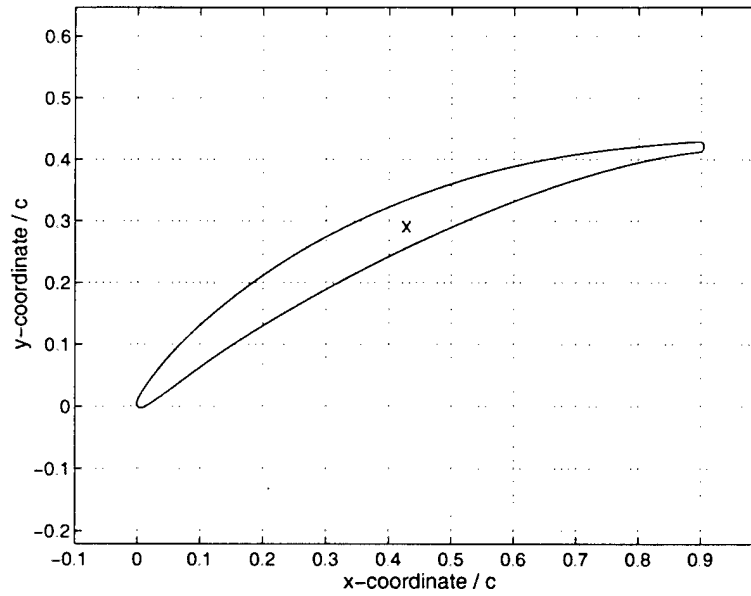


Figure 39: 50% span section of the LSRC Stator-B blade used for the viscous simulations. X denotes the location about which moments are evaluated (0.42c, 0.29c).

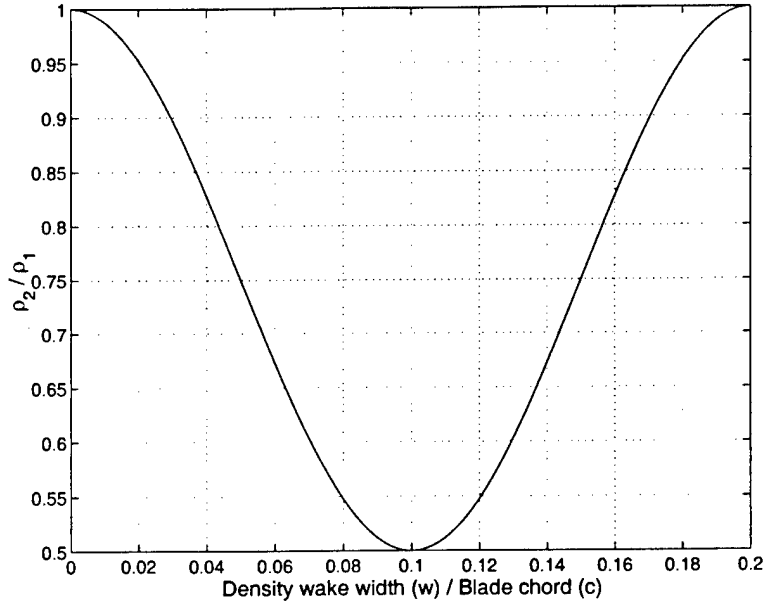


Figure 40: Density wake profile. $w/c = 0.2$, $\rho_2/\rho_1 = 0.5$.

The density wake profile specified to represent a wake width $0.2c$ and density ratio $\rho_2/\rho_1 = 0.5$ is illustrated in Figure 40.

14.5 Converged Solutions

A converged baseline solution was first obtained before simulating the passage of density wakes through the cascade. Solution convergence was determined by monitoring the time history of the L2 norm of the flow variables ρ , ρu , ρv and ρe where ρ , u , v , and e denote density, axial velocity, azimuthal velocity and energy. A typical variation in the L2 norm for ρe is plotted in Figure 41. A converged solution was attained when the L2 norm for each flow variable showed no further significant reduction with time. In addition the flow field contour plots were examined to ensure that unsteady transients were no longer present in the solution.

14.6 Non-Dimensionalization

The equations of motion are non-dimensionalized using the following reference quantities.

- Length : blade spacing (s)
- Velocity : rotor tip speed (U_R)
- Density : free stream density (ρ_∞)
- Temperature : free stream temperature (T_∞)

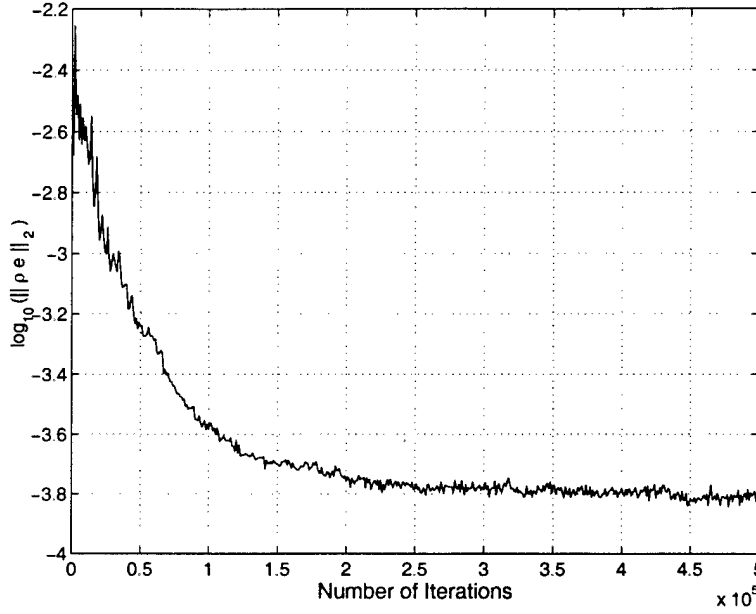


Figure 41: Convergence history for the L2 norm of density $\rho \times$ energy e . $M_\infty = 0.53$.

- Viscosity : free stream viscosity (μ_∞)
- Pressure : $\rho_\infty U_R^2$
- Energy : U_R^2

For the cascade geometry considered in this study the blade chord c and inlet total velocity U_∞ are more relevant non-dimensional variables for the length and velocity scales¹⁸. These variables are therefore used in the definitions for Reynolds number, Mach number, force coefficients, moment coefficient (positive clockwise about $x/c = 0.42$, $y/c = 0.29$) and skin friction coefficient as follows,

¹⁸An additional factor of 0.5 for the pressure non-dimensionalization is also more appropriate.

$$\begin{aligned}
Re_{\infty} &= \frac{\rho_{\infty} U_{\infty} c}{\mu_{\infty}} \\
M_{\infty} &= \frac{U_{\infty}}{\sqrt{\gamma R T_{\infty}}} \\
C_y &= \frac{p \Delta x}{0.5 \rho_{\infty} U_{\infty}^2 c} \\
C_x &= \frac{p \Delta y}{0.5 \rho_{\infty} U_{\infty}^2 c} \\
C_m &= \frac{p \Delta y \Delta l}{0.5 \rho_{\infty} U_{\infty}^2 c^2} \\
C_f &= \frac{\tau_w}{0.5 \rho_{\infty} U_{\infty}^2}
\end{aligned}$$

Note the flow Reynolds number and Mach number based on the inlet total velocity and blade chord are determined after a converged solution is obtained and cannot be specified a-priori. The Reynolds numbers and Mach numbers required as input conditions to the flow solver are based on the blade spacing and rotor tip speed instead¹⁹.

¹⁹Since there is no rotor in this study the values for Reynolds number and Mach number specified as input conditions are essentially unit values.

15 Baseline Flow Results

The following plots are included in this Section:

- Time averaged blade pressure distributions.
- Azimuthal force coefficient C_y , axial force coefficient C_x and moment coefficient C_m fluctuations in the baseline response.
- Time averaged boundary layer properties: non-dimensional momentum thickness θ/c , non-dimensional displacement thickness δ^*/c and skin friction coefficient C_f .

Note the following:

- The moment coefficient is defined positive clockwise and is calculated about the blade coordinates $x/c = 0.42$ and $y/c = 0.29$ (see Figure 39).
- The boundary layer properties are plotted vs. the surface distance to help increase resolution at the blade leading and trailing edge regions.

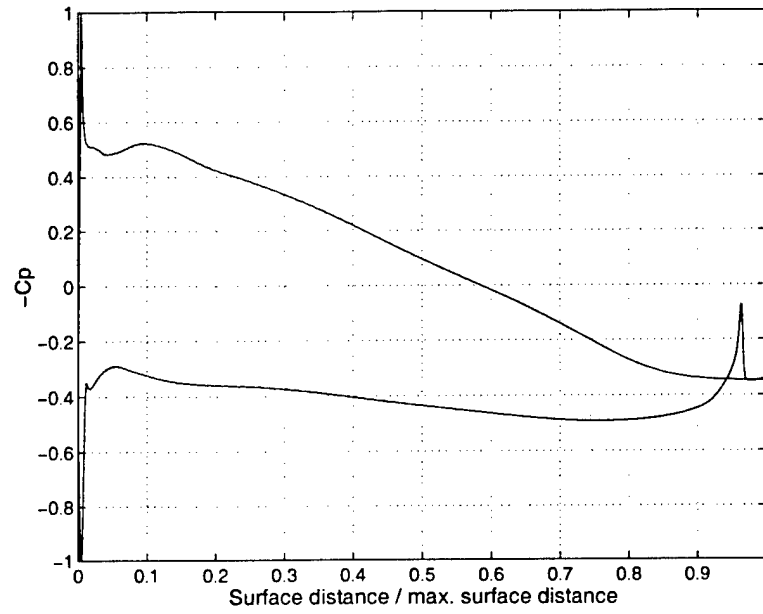


Figure 42: Time averaged blade pressure distribution. $M_\infty = 0.15$.

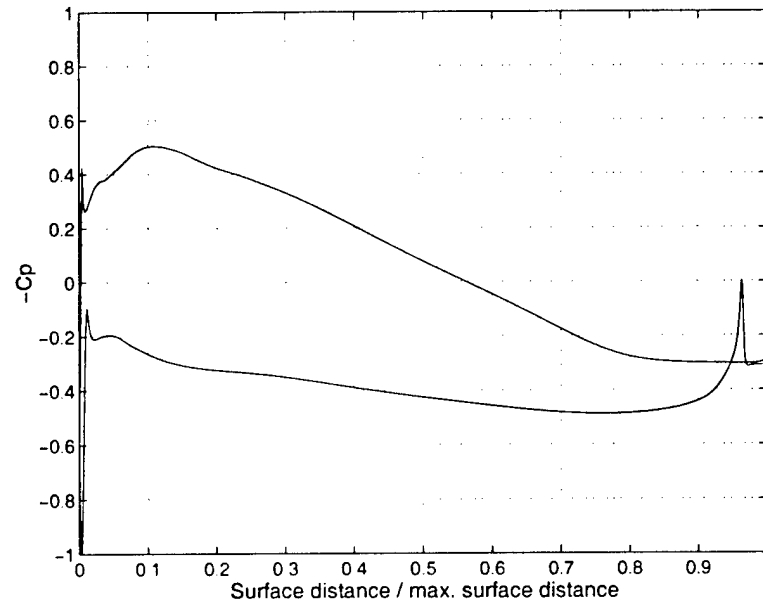


Figure 43: Time averaged blade pressure distribution. $M_\infty = 0.53$.

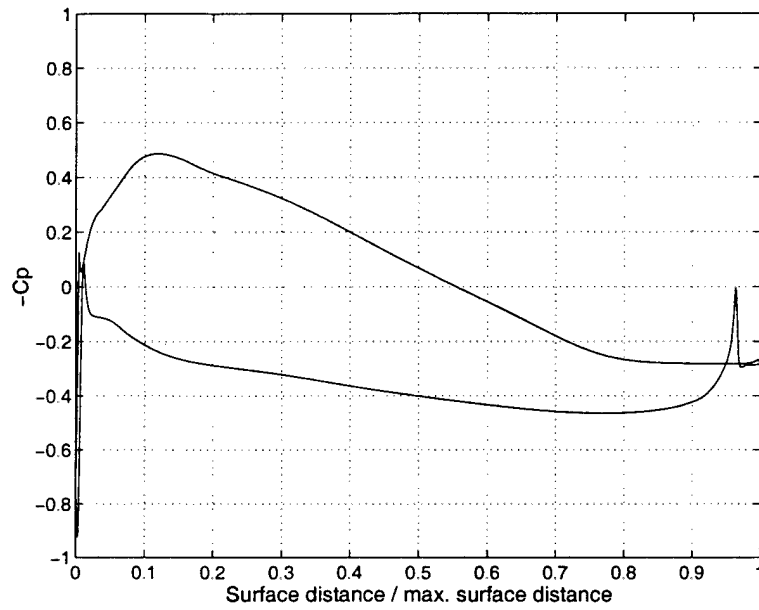


Figure 44: Time averaged blade pressure distribution. $M_\infty = 0.63$.

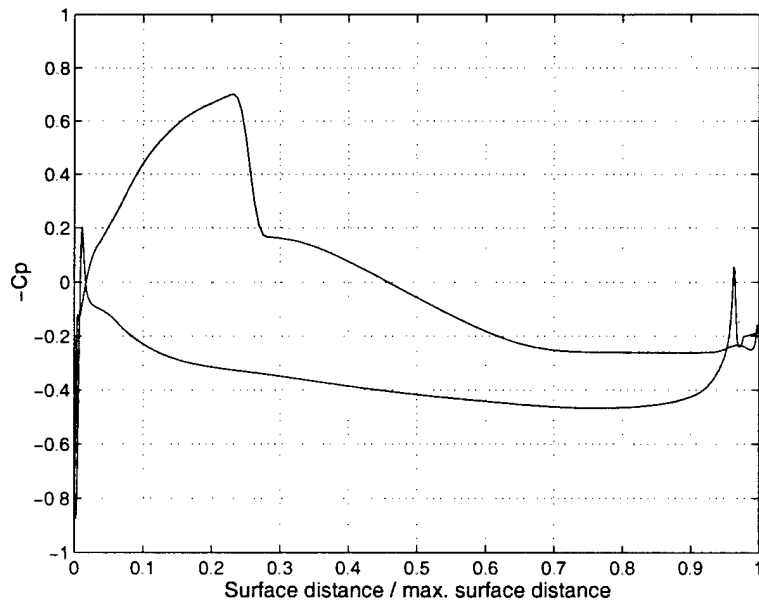


Figure 45: Time averaged blade pressure distribution. $M_\infty = 0.87$.

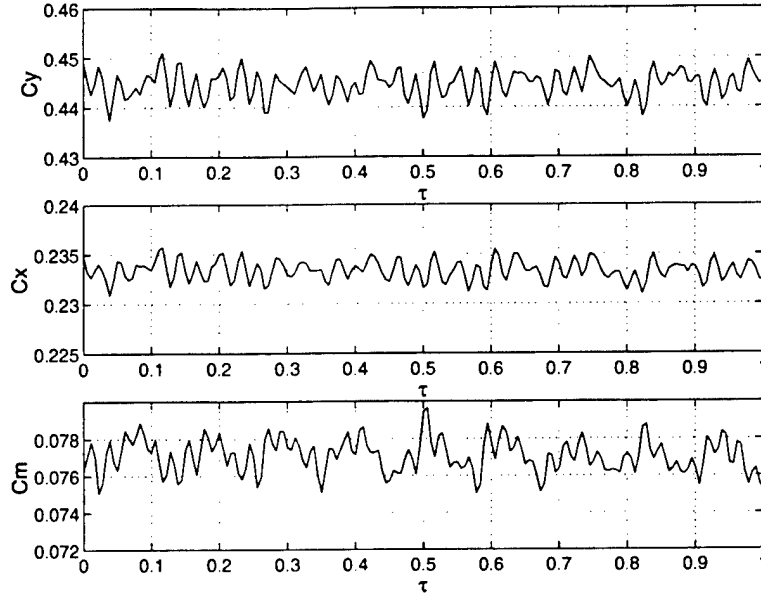


Figure 46: The force and moment coefficient fluctuation in the baseline solution of Run 1. C_y , C_x and C_m are the blade azimuthal force, axial force and moment coefficients respectively. τ = convective time scale. $M_\infty = 0.15$.

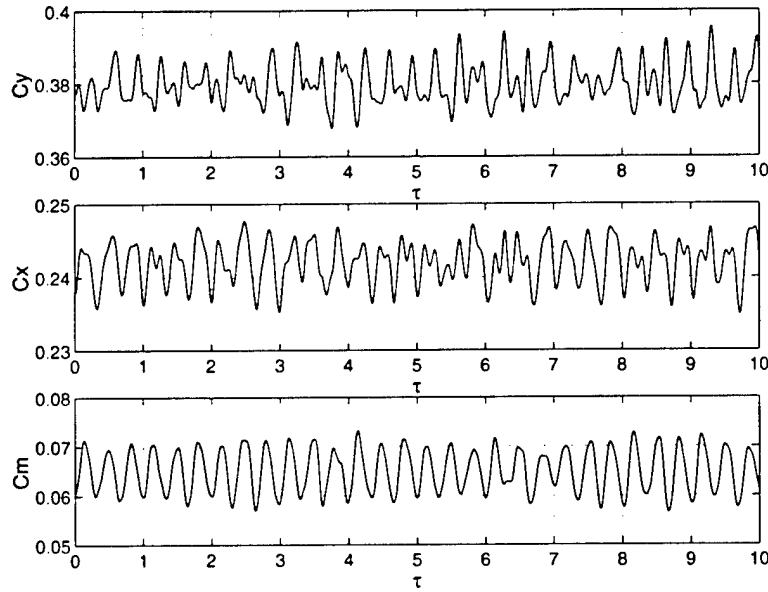


Figure 47: The force and moment coefficient fluctuation in the baseline solution of Run 2. C_y , C_x and C_m are the blade azimuthal force, axial force and moment coefficients respectively. τ = convective time scale. $M_\infty = 0.53$.

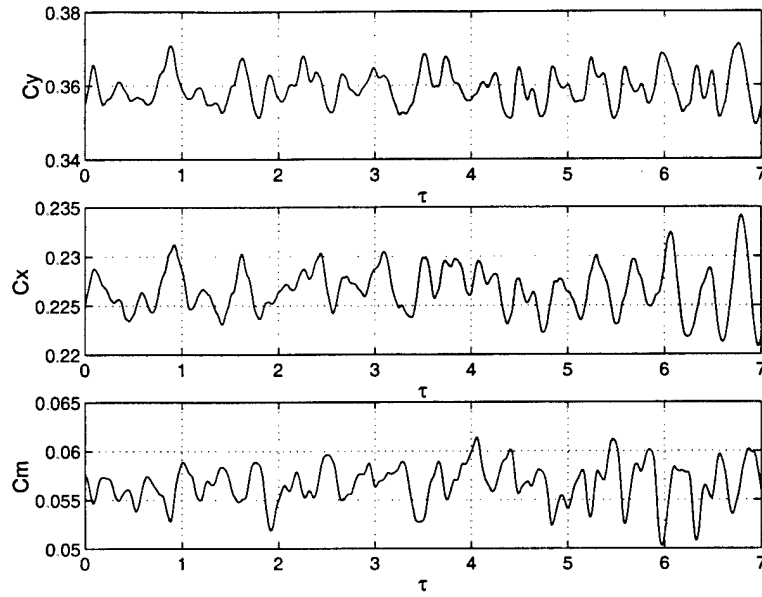


Figure 48: The force and moment coefficient fluctuation in the baseline solution of Run 3. C_y , C_x and C_m are the blade azimuthal force, axial force and moment coefficients respectively. τ = convective time scale. $M_\infty = 0.63$.

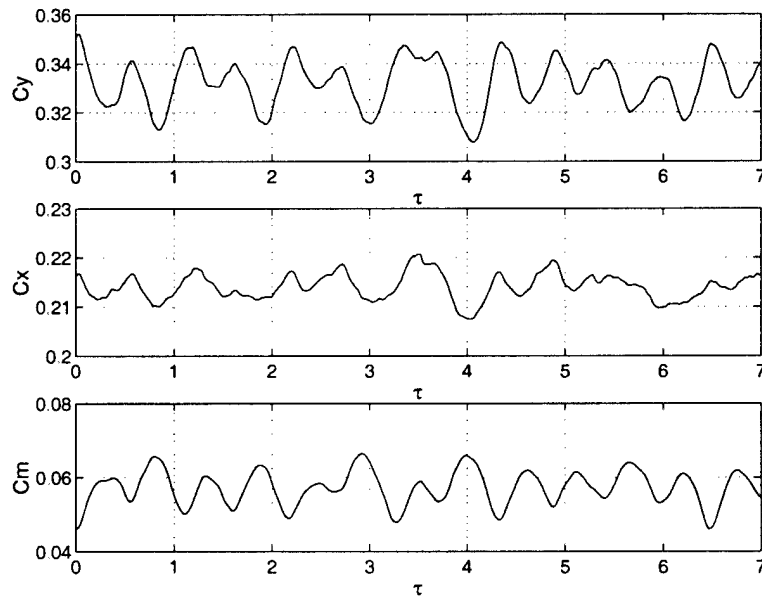


Figure 49: The force and moment coefficient fluctuation in the baseline solution of Run 4. C_y , C_x and C_m are the blade azimuthal force, axial force and moment coefficients respectively. τ = convective time scale. $M_\infty = 0.87$.

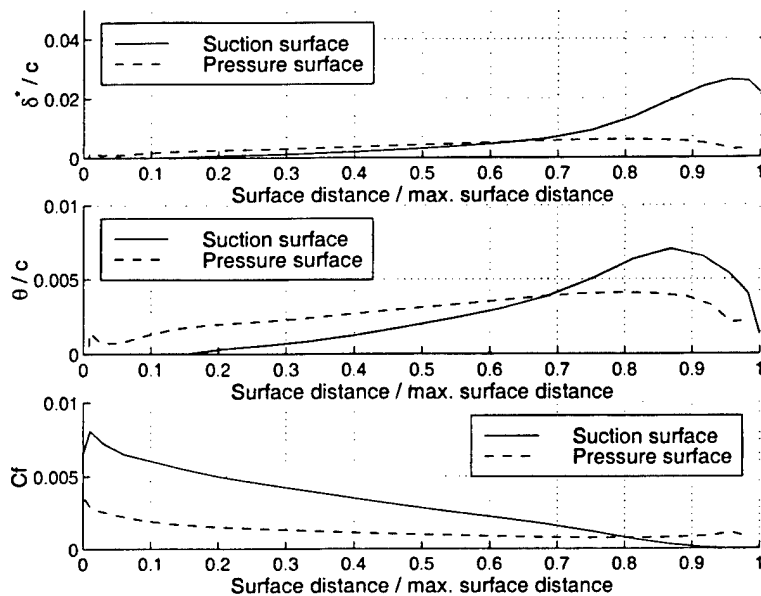


Figure 50: Time averaged boundary layer properties. $M_\infty = 0.15$.

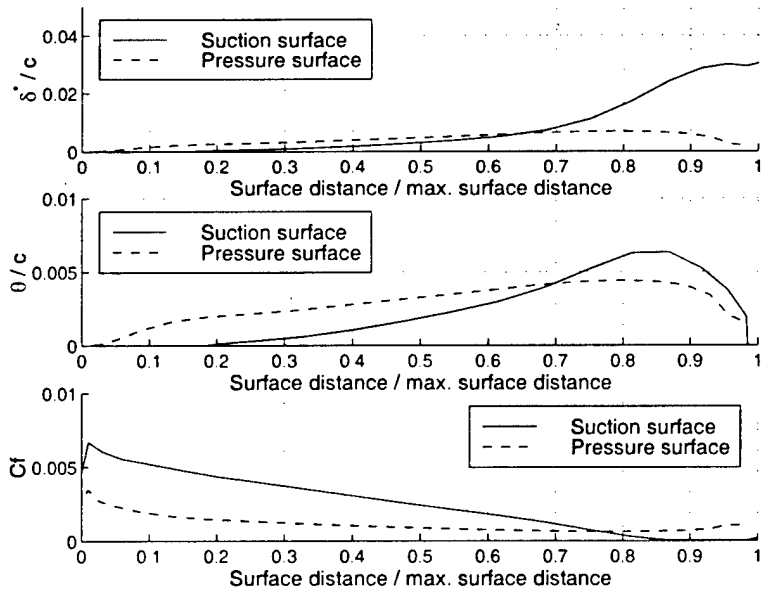


Figure 51: Time averaged boundary layer properties. $M_\infty = 0.53$.

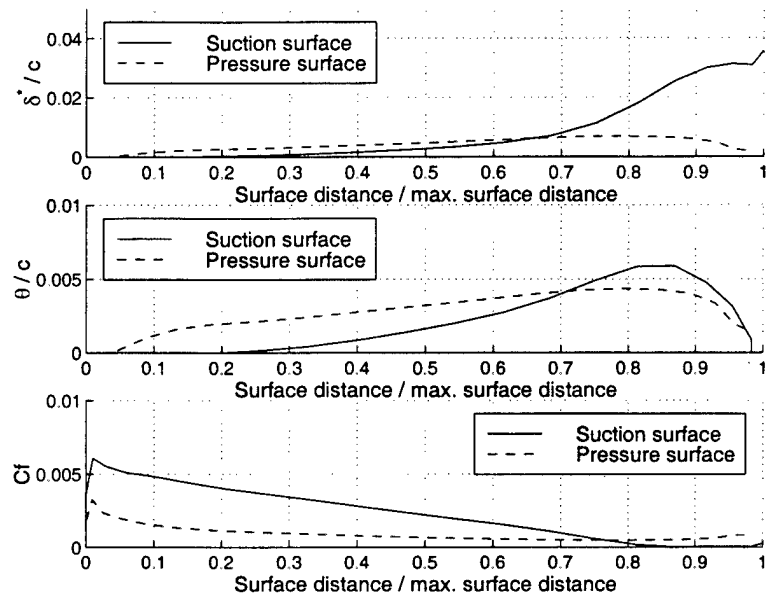


Figure 52: Time averaged boundary layer properties. $M_\infty = 0.63$.

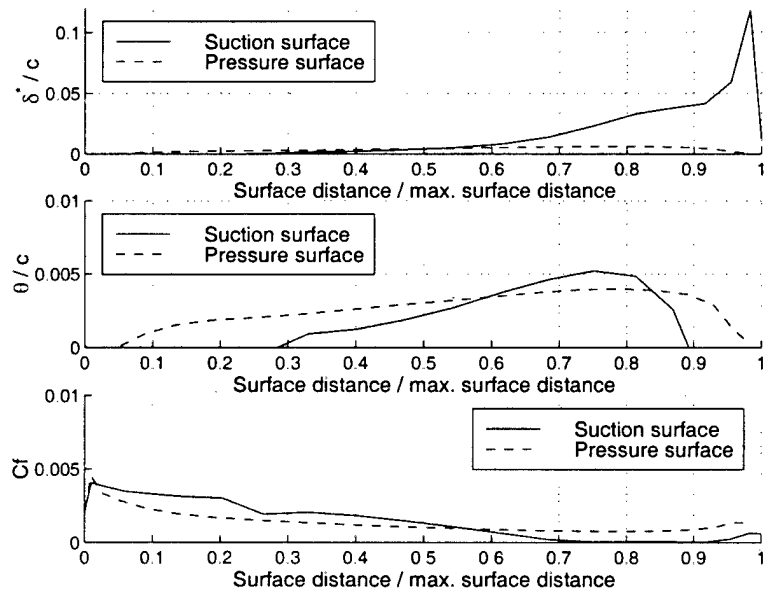


Figure 53: Time averaged boundary layer properties. $M_\infty = 0.87$.

16 Primary and Secondary Response Results

The following are included in this Section:

- Parametric test results for the (1) Azimuthal force coefficient C_y , (2) axial force coefficient C_x and (3) moment coefficient C_m fluctuations. The complete list of parametric tests are detailed in Table 5. Consecutive plots are ordered first according to the density ratio, secondly by the Mach number and thirdly by the wake width.
- Functional relationships to scale the maximum fluctuation in the force and moment response.

Note the moment coefficient is defined positive clockwise and is calculated about the blade coordinates $x/c = 0.42$ and $y/c = 0.29$ (see Figure 39).

| Parameter | Run 1 | Run 2 | Run 3 | Run 4 |
|-----------------|------------------------|---------------|-------|-------|
| M_∞ | 0.15 | 0.53 | 0.63 | 0.87 |
| w/c | 0.1,0.2,0.4,1.0 | 0.1, 0.2, 0.4 | | |
| ρ_2/ρ_1 | 0.25, 0.50, 0.75, 2.00 | | | |

Table 5: Parametric test variables. w/c = non-dimensional wake width, ρ_2/ρ_1 = maximum density inside wake / free stream density.

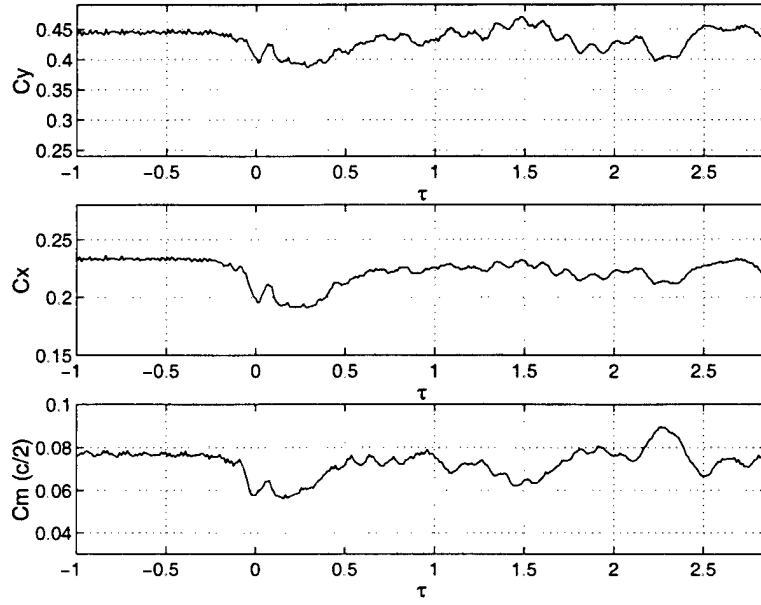


Figure 54: Fluctuation in blade force and moment coefficients. $w/c = 0.1$, $\rho_2/\rho_1 = 0.25$, $M_\infty = 0.15$.

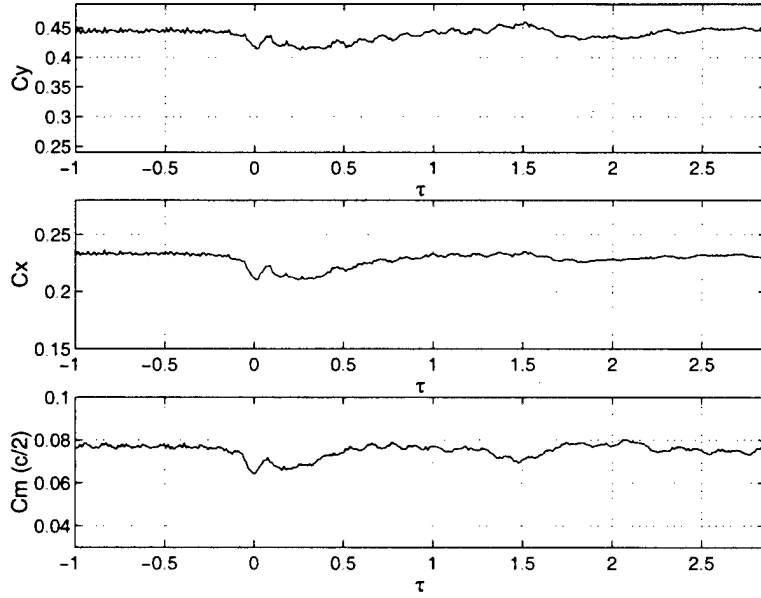


Figure 55: Fluctuation in blade force and moment coefficients. $w/c = 0.1$, $\rho_2/\rho_1 = 0.50$, $M_\infty = 0.15$.

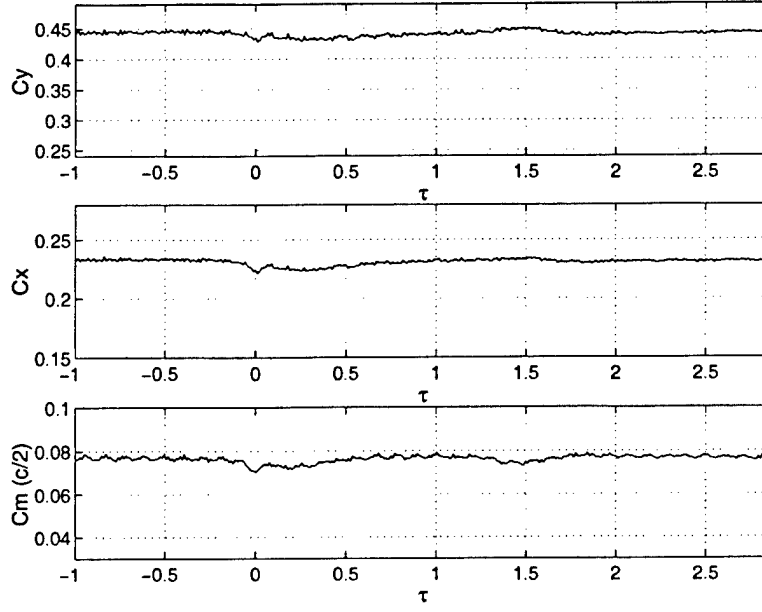


Figure 56: Fluctuation in blade force and moment coefficients. $w/c = 0.1$, $\rho_2/\rho_1 = 0.75$, $M_\infty = 0.15$.

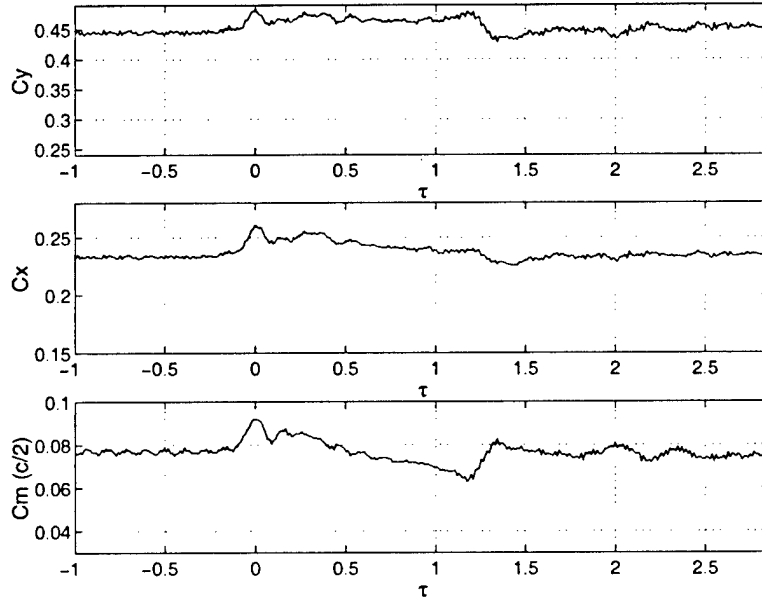


Figure 57: Fluctuation in blade force and moment coefficients. $w/c = 0.1$, $\rho_2/\rho_1 = 2.00$, $M_\infty = 0.15$.

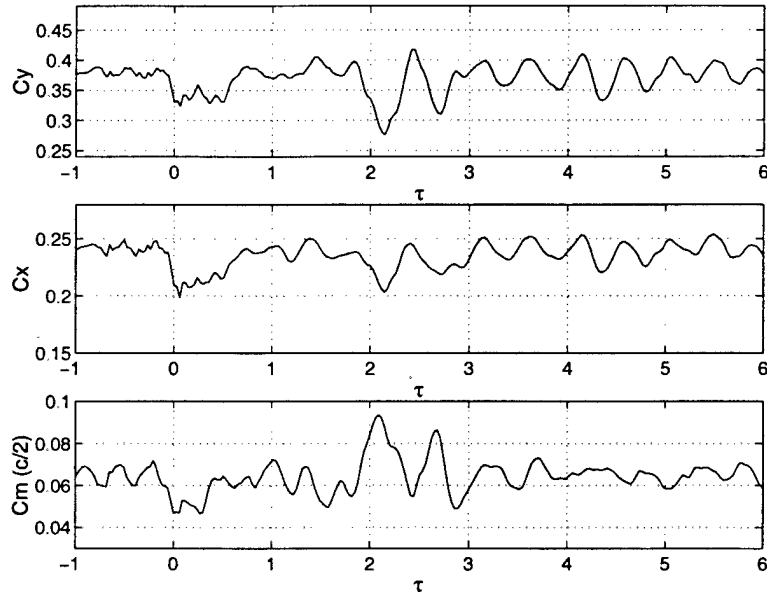


Figure 58: Fluctuation in blade force and moment coefficients. $w/c = 0.1$, $\rho_2/\rho_1 = 0.25$, $M_\infty = 0.53$.

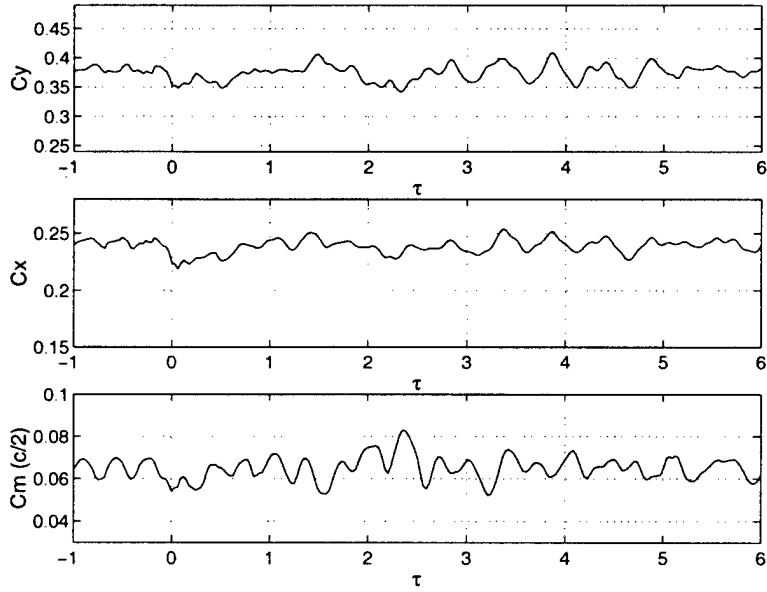


Figure 59: Fluctuation in blade force and moment coefficients. $w/c = 0.1$, $\rho_2/\rho_1 = 0.50$, $M_\infty = 0.53$.

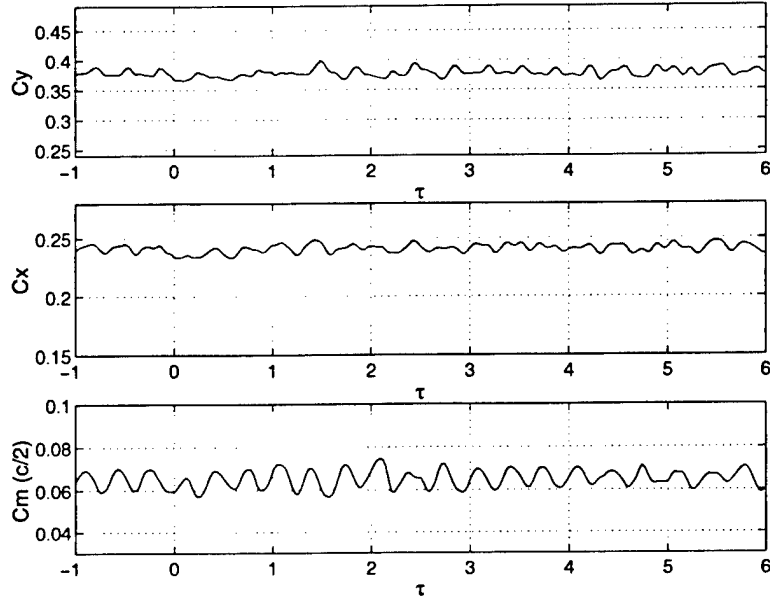


Figure 60: Fluctuation in blade force and moment coefficients. $w/c = 0.1$, $\rho_2/\rho_1 = 0.75$, $M_\infty = 0.53$.

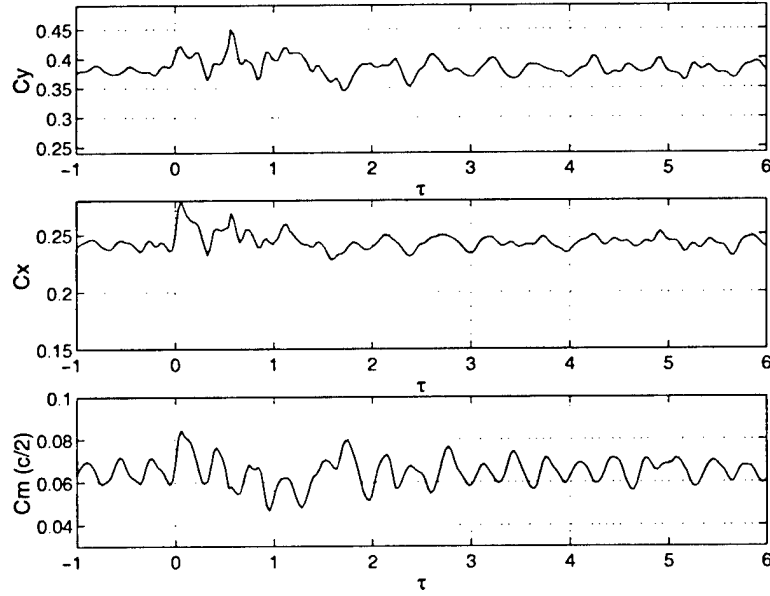


Figure 61: Fluctuation in blade force and moment coefficients. $w/c = 0.1$, $\rho_2/\rho_1 = 2.00$, $M_\infty = 0.53$.

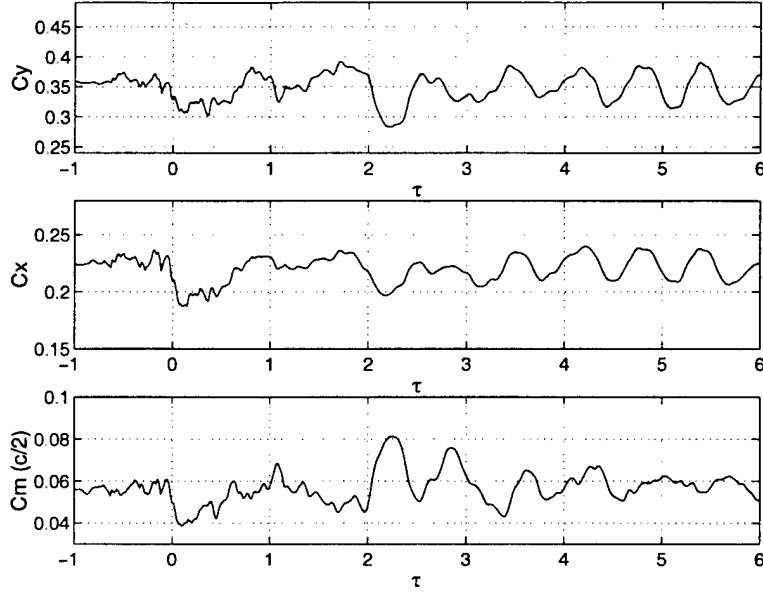


Figure 62: Fluctuation in blade force and moment coefficients. $w/c = 0.1$, $\rho_2/\rho_1 = 0.25$, $M_\infty = 0.63$.

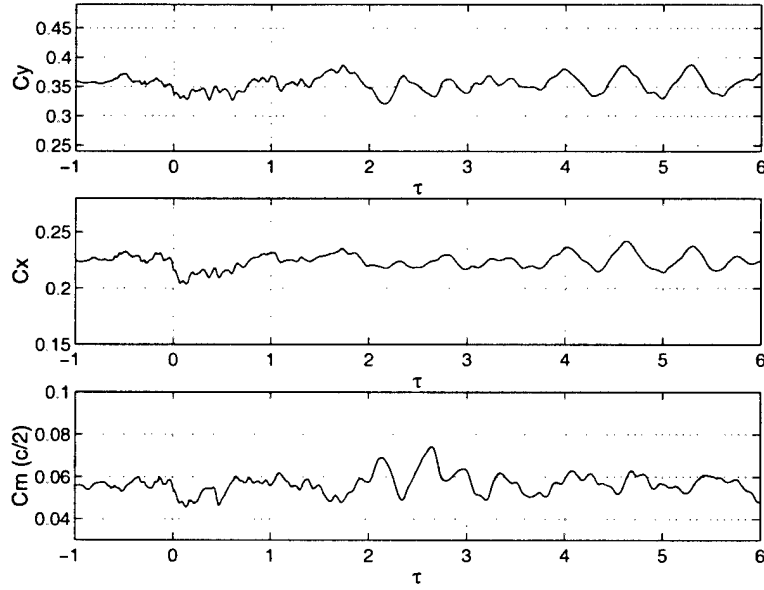


Figure 63: Fluctuation in blade force and moment coefficients. $w/c = 0.1$, $\rho_2/\rho_1 = 0.50$, $M_\infty = 0.63$.

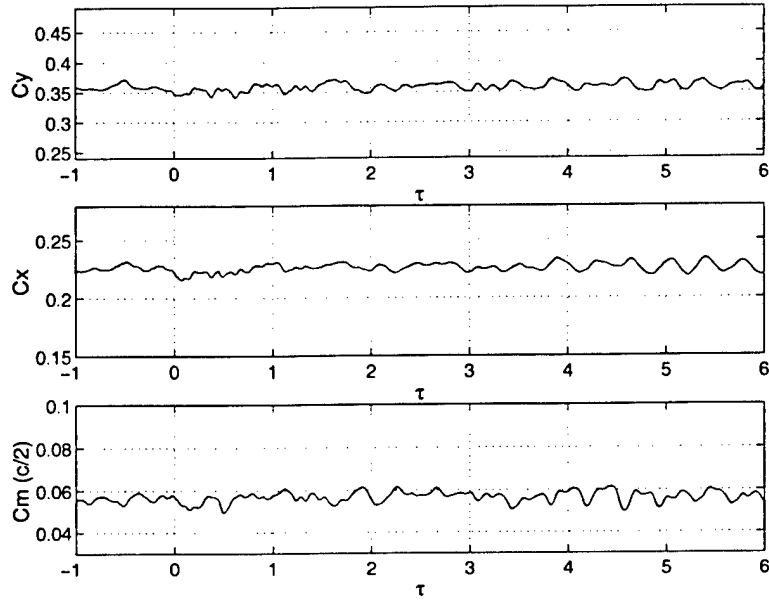


Figure 64: Fluctuation in blade force and moment coefficients. $w/c = 0.1$, $\rho_2/\rho_1 = 0.75$, $M_\infty = 0.63$.

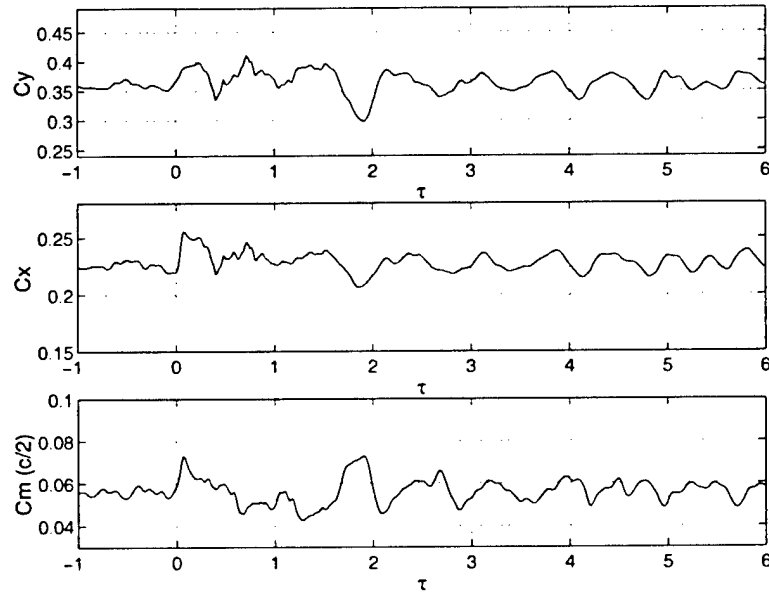


Figure 65: Fluctuation in blade force and moment coefficients. $w/c = 0.1$, $\rho_2/\rho_1 = 2.00$, $M_\infty = 0.63$.

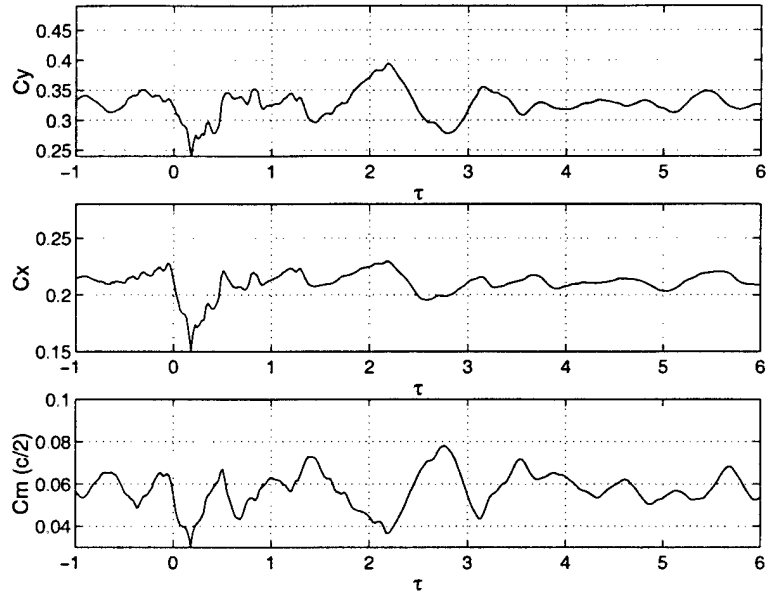


Figure 66: Fluctuation in blade force and moment coefficients. $w/c = 0.1$, $\rho_2/\rho_1 = 0.25$, $M_\infty = 0.87$.

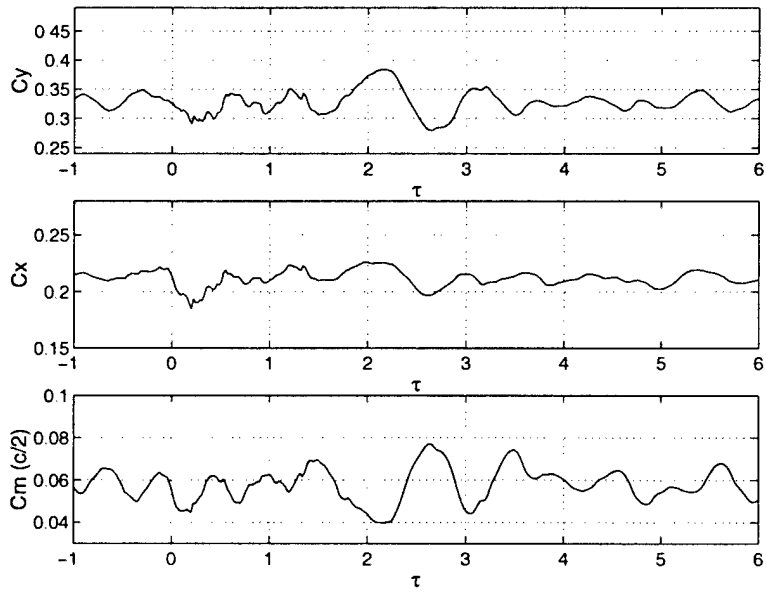


Figure 67: Fluctuation in blade force and moment coefficients. $w/c = 0.1$, $\rho_2/\rho_1 = 0.50$, $M_\infty = 0.87$.

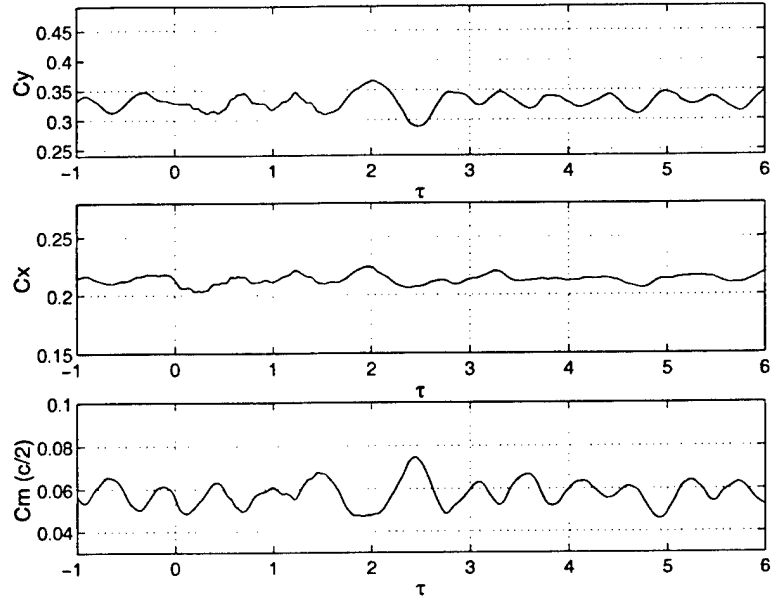


Figure 68: Fluctuation in blade force and moment coefficients. $w/c = 0.1$, $\rho_2/\rho_1 = 0.75$, $M_\infty = 0.87$.

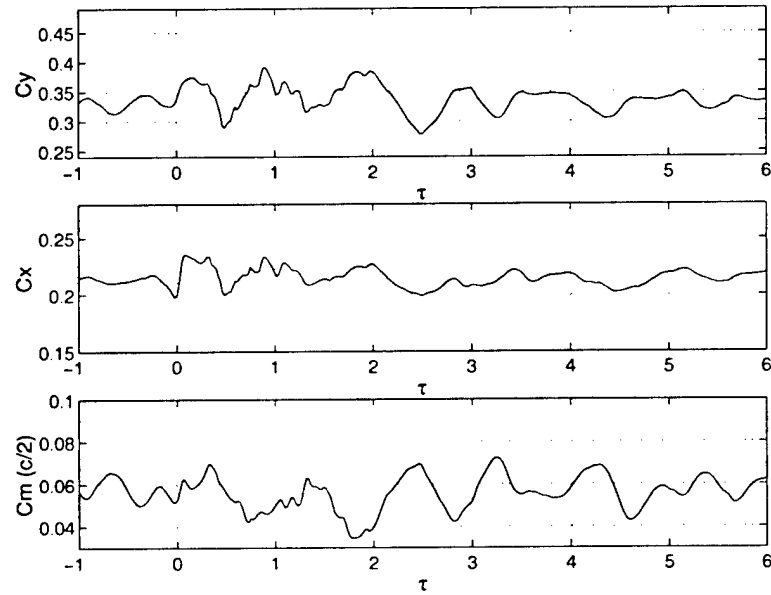


Figure 69: Fluctuation in blade force and moment coefficients. $w/c = 0.1$, $\rho_2/\rho_1 = 2.00$, $M_\infty = 0.87$.

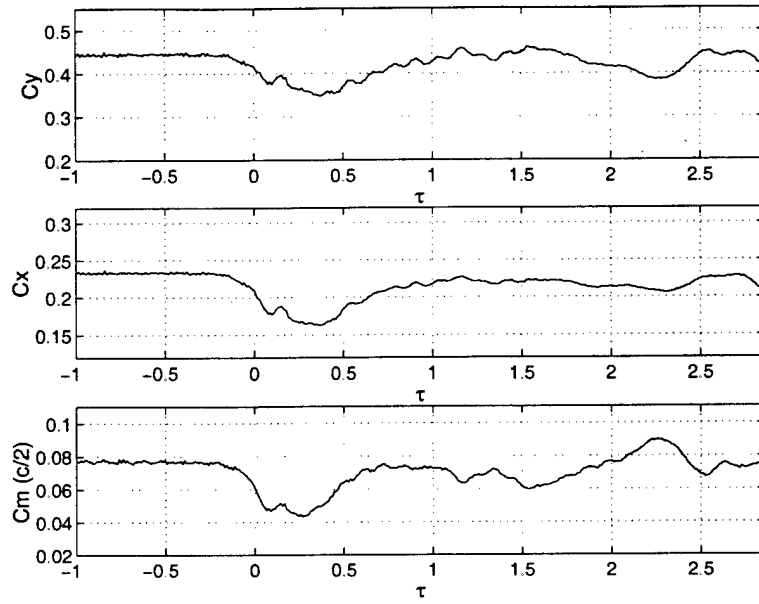


Figure 70: Fluctuation in blade force and moment coefficients. $w/c = 0.2$, $\rho_2/\rho_1 = 0.25$, $M_\infty = 0.15$.

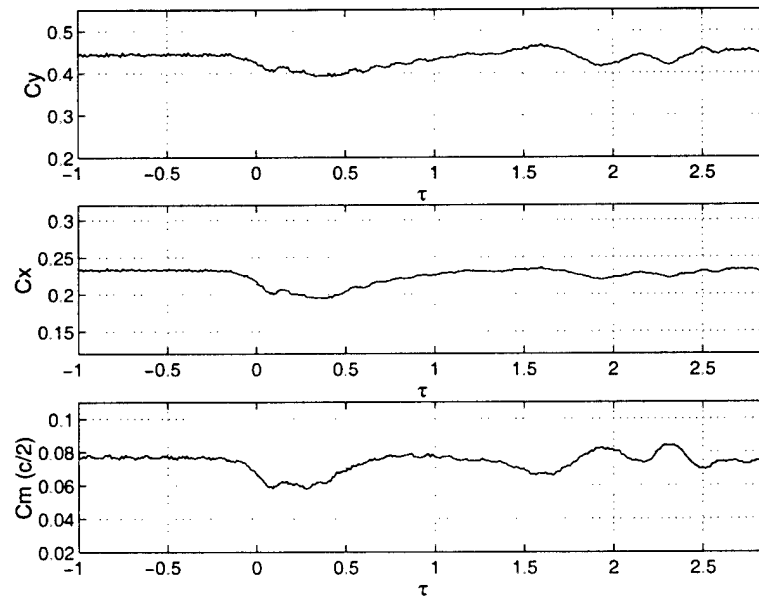


Figure 71: Fluctuation in blade force and moment coefficients. $w/c = 0.2$, $\rho_2/\rho_1 = 0.50$, $M_\infty = 0.15$.

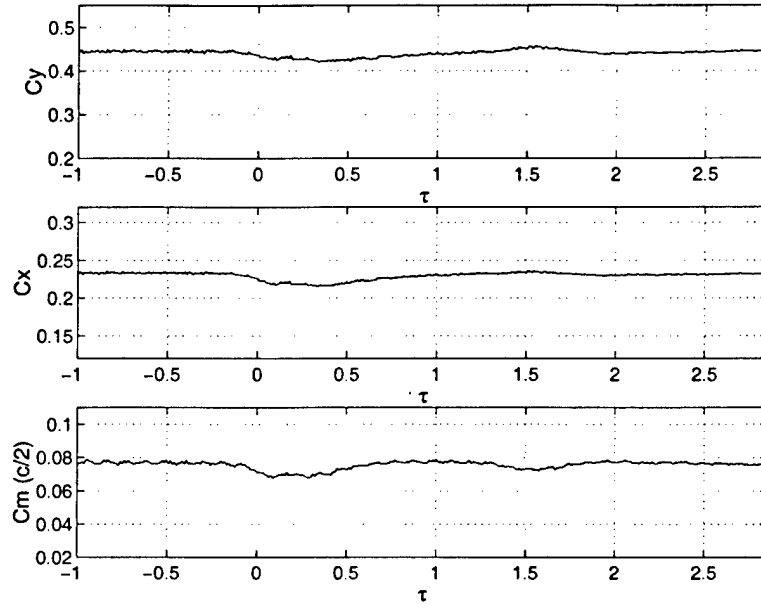


Figure 72: Fluctuation in blade force and moment coefficients. $w/c = 0.2$, $\rho_2/\rho_1 = 0.75$, $M_\infty = 0.15$.

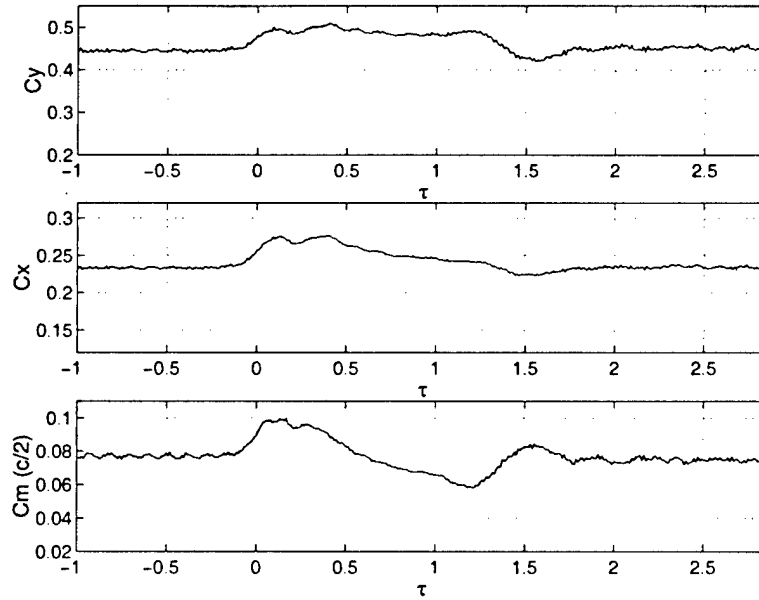


Figure 73: Fluctuation in blade force and moment coefficients. $w/c = 0.2$, $\rho_2/\rho_1 = 2.00$, $M_\infty = 0.15$.

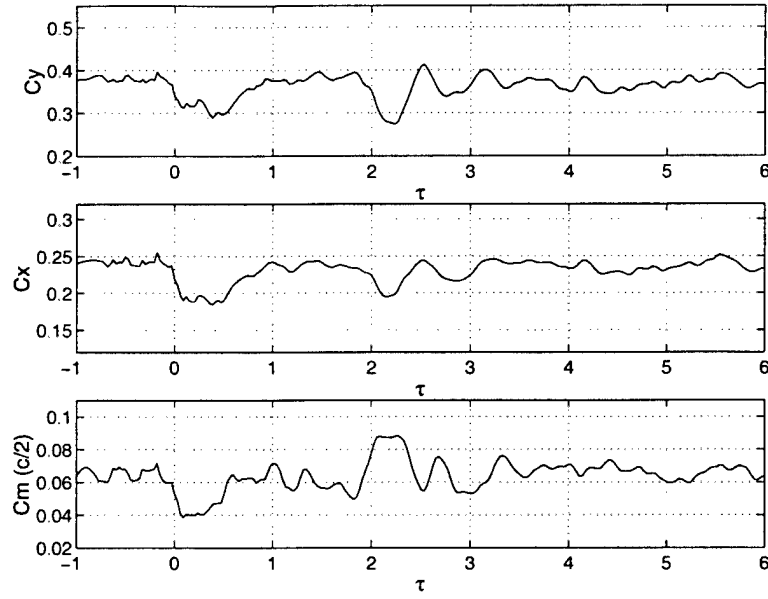


Figure 74: Fluctuation in blade force and moment coefficients. $w/c = 0.2$, $\rho_2/\rho_1 = 0.25$, $M_\infty = 0.53$.

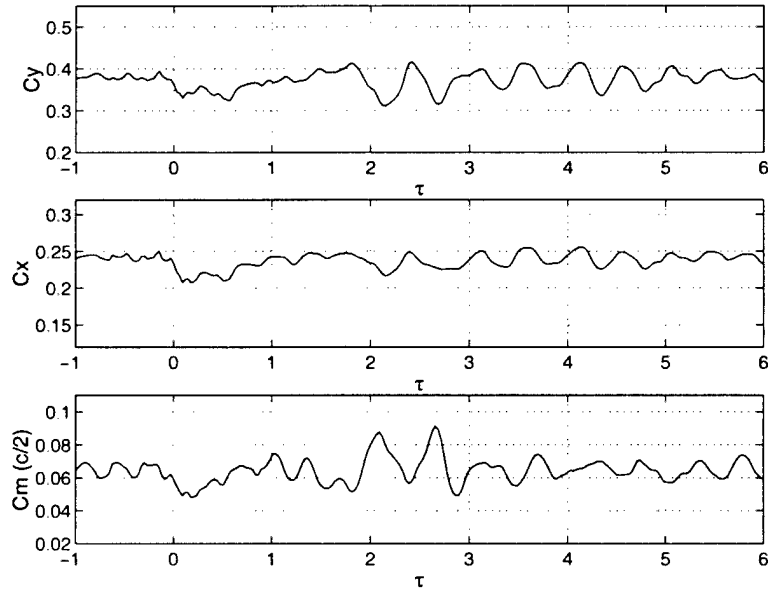


Figure 75: Fluctuation in blade force and moment coefficients. $w/c = 0.2$, $\rho_2/\rho_1 = 0.50$, $M_\infty = 0.53$.

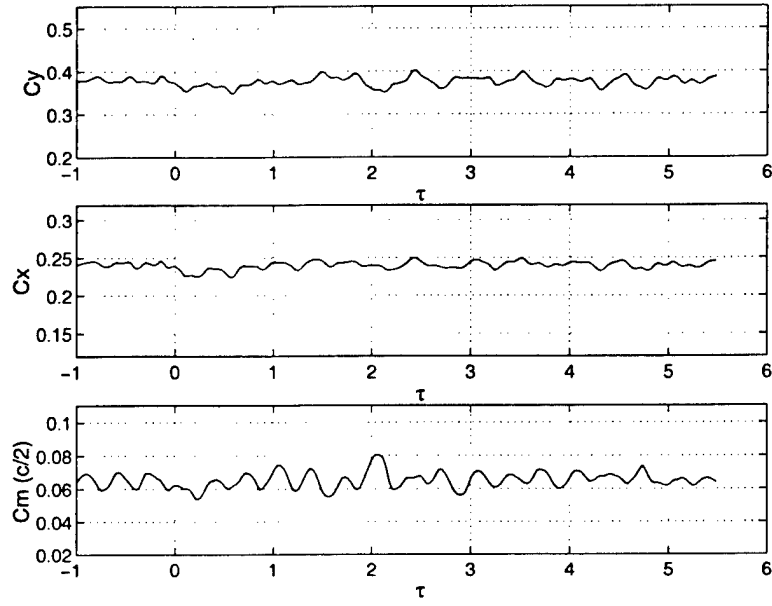


Figure 76: Fluctuation in blade force and moment coefficients. $w/c = 0.2$, $\rho_2/\rho_1 = 0.75$, $M_\infty = 0.53$.

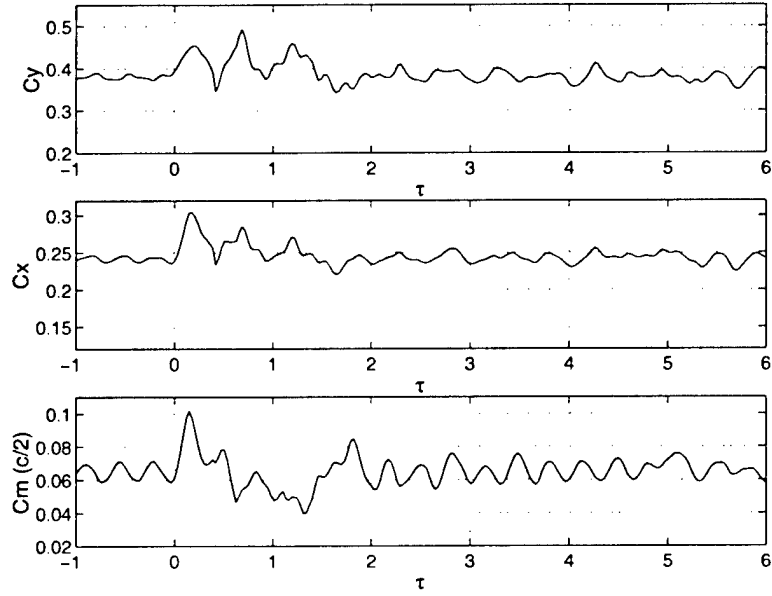


Figure 77: Fluctuation in blade force and moment coefficients. $w/c = 0.2$, $\rho_2/\rho_1 = 2.00$, $M_\infty = 0.53$.

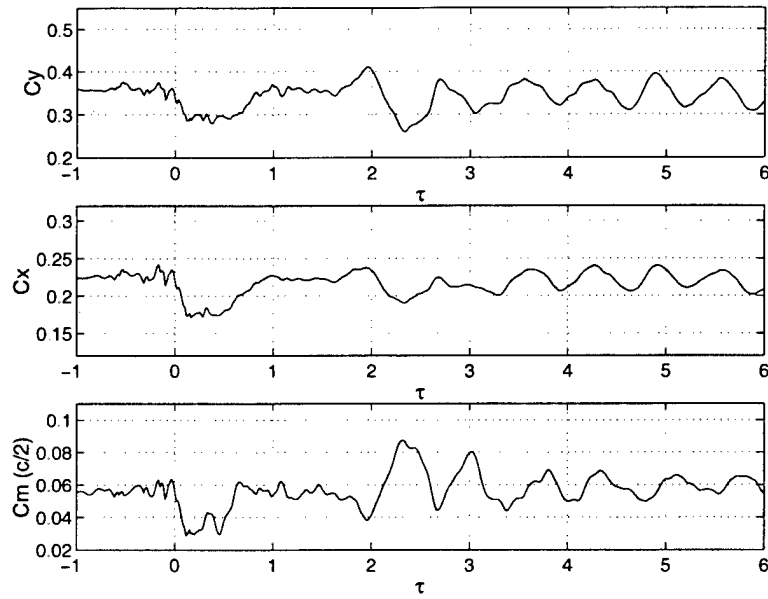


Figure 78: Fluctuation in blade force and moment coefficients. $w/c = 0.2$, $\rho_2/\rho_1 = 0.25$, $M_\infty = 0.63$.

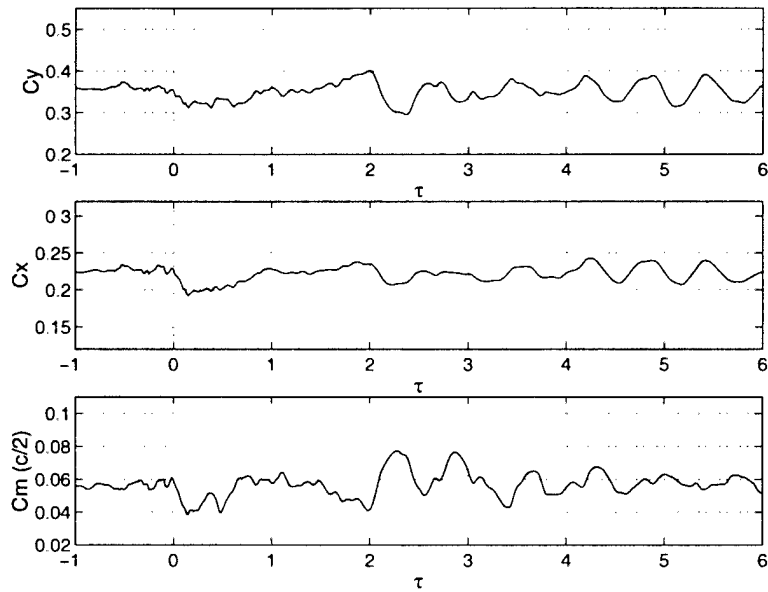


Figure 79: Fluctuation in blade force and moment coefficients. $w/c = 0.2$, $\rho_2/\rho_1 = 0.50$, $M_\infty = 0.63$.

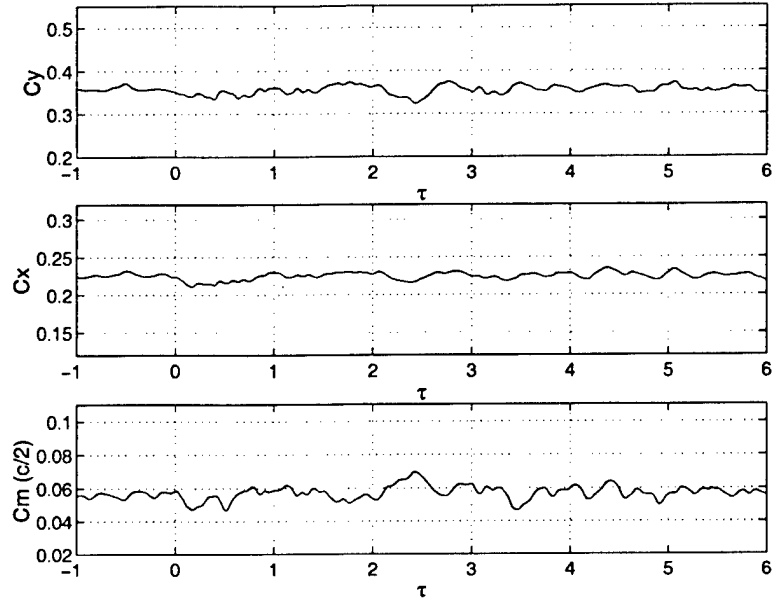


Figure 80: Fluctuation in blade force and moment coefficients. $w/c = 0.2$, $\rho_2/\rho_1 = 0.75$, $M_\infty = 0.63$.

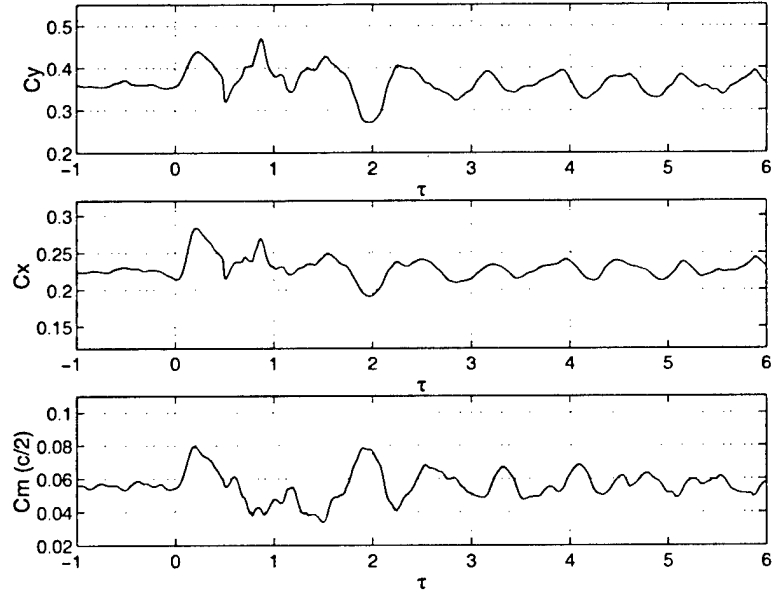


Figure 81: Fluctuation in blade force and moment coefficients. $w/c = 0.2$, $\rho_2/\rho_1 = 2.00$, $M_\infty = 0.63$.

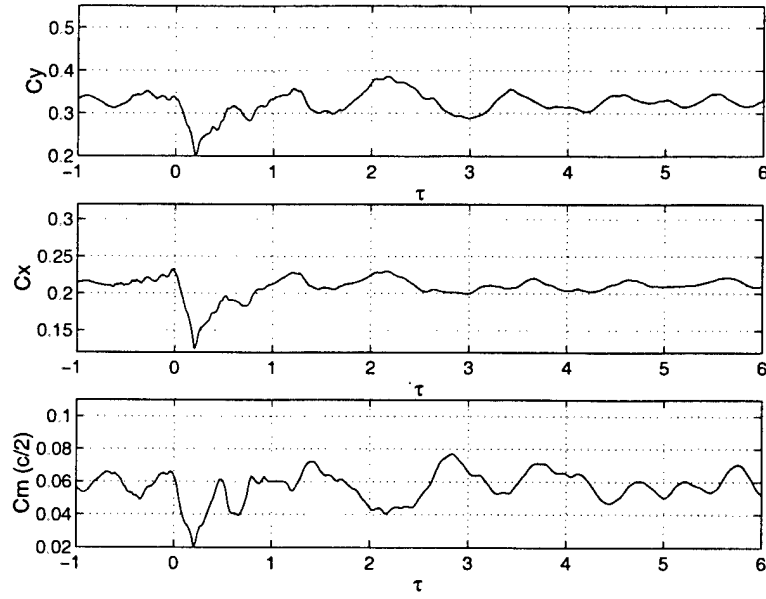


Figure 82: Fluctuation in blade force and moment coefficients. $w/c = 0.2$, $\rho_2/\rho_1 = 0.25$, $M_\infty = 0.87$.

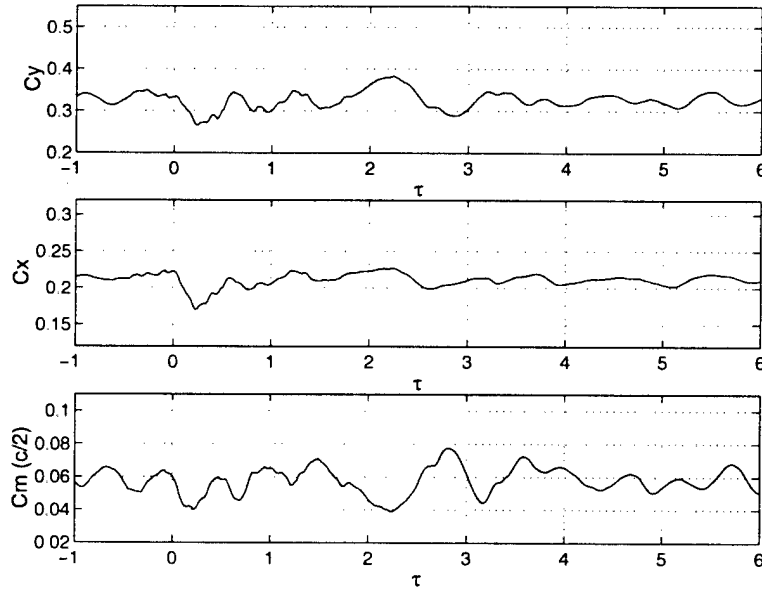


Figure 83: Fluctuation in blade force and moment coefficients. $w/c = 0.2$, $\rho_2/\rho_1 = 0.50$, $M_\infty = 0.87$.

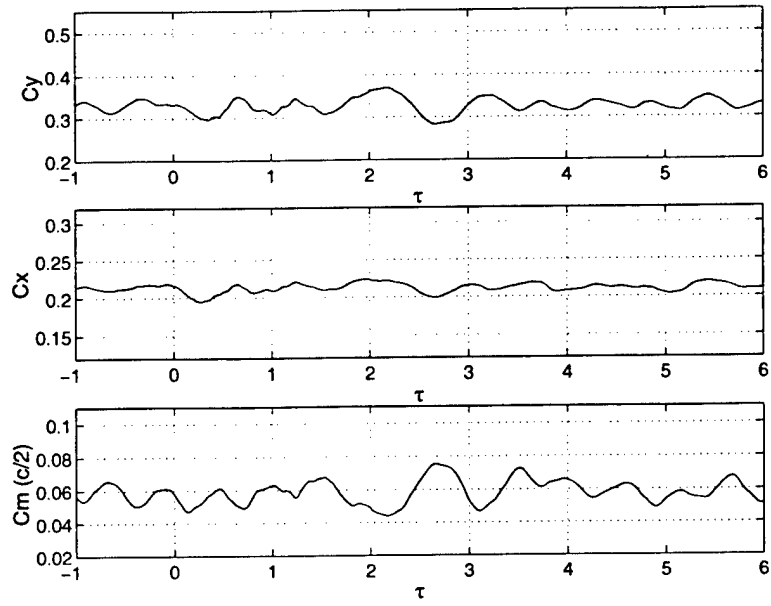


Figure 84: Fluctuation in blade force and moment coefficients. $w/c = 0.2$, $\rho_2/\rho_1 = 0.75$, $M_\infty = 0.87$.

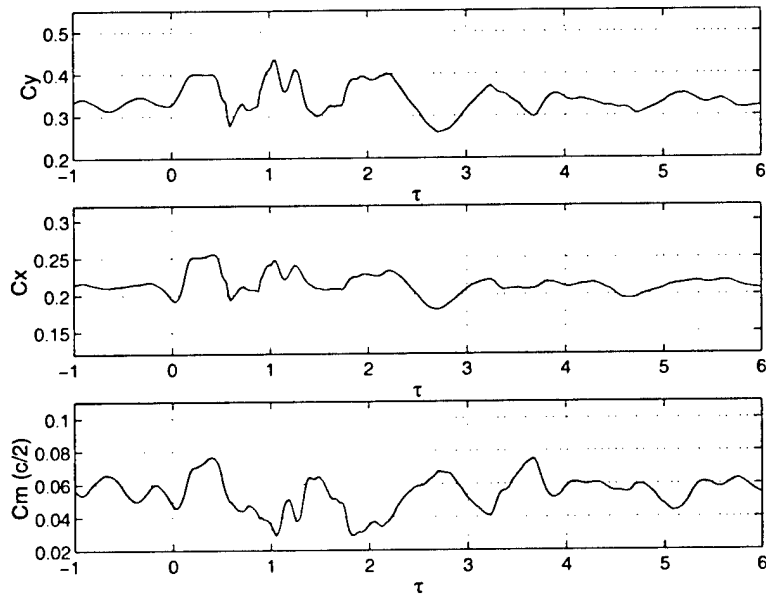


Figure 85: Fluctuation in blade force and moment coefficients. $w/c = 0.2$, $\rho_2/\rho_1 = 2.00$, $M_\infty = 0.87$.

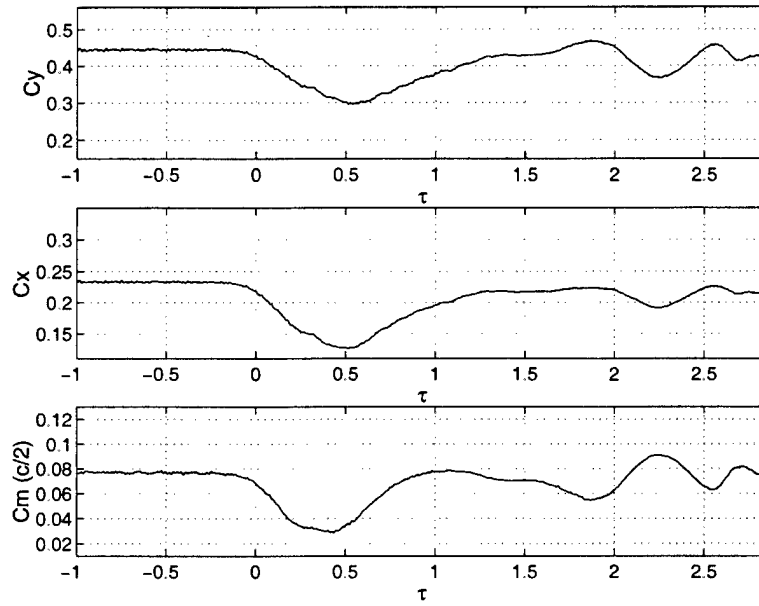


Figure 86: Fluctuation in blade force and moment coefficients. $w/c = 0.4$, $\rho_2/\rho_1 = 0.25$, $M_\infty = 0.15$.

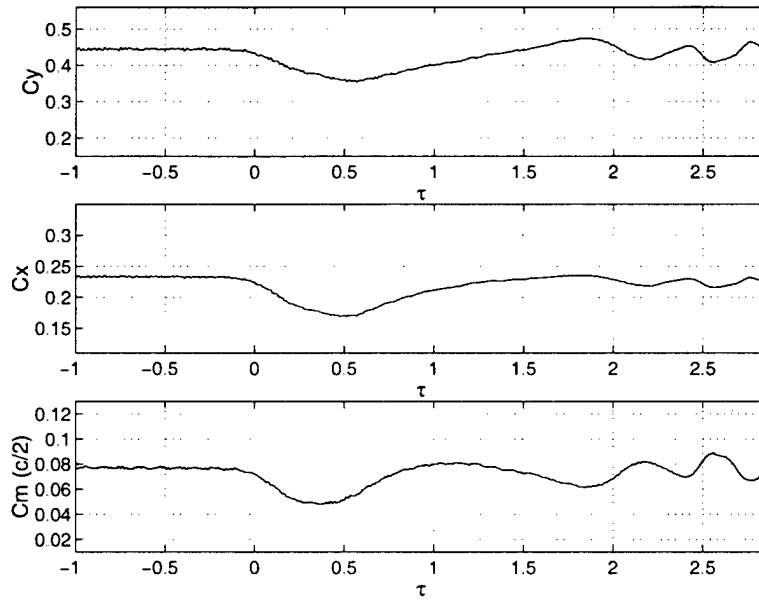


Figure 87: Fluctuation in blade force and moment coefficients. $w/c = 0.4$, $\rho_2/\rho_1 = 0.50$, $M_\infty = 0.15$.

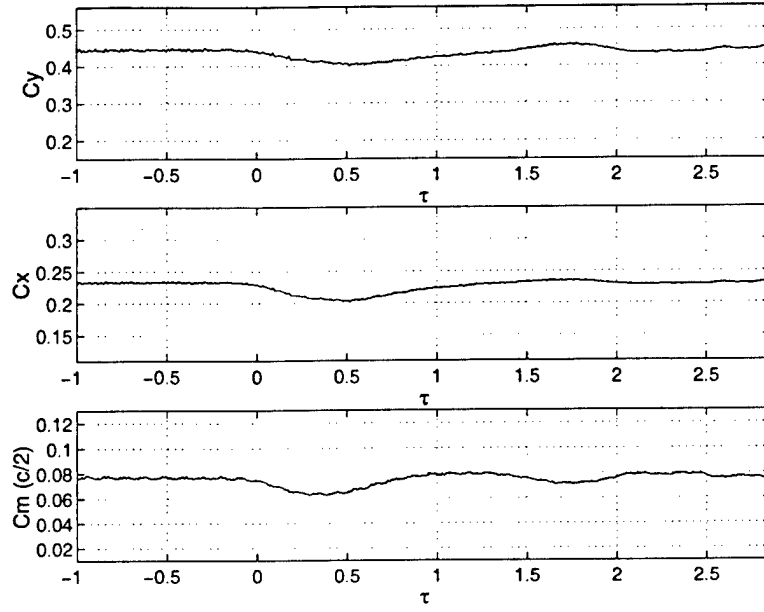


Figure 88: Fluctuation in blade force and moment coefficients. $w/c = 0.4$, $\rho_2/\rho_1 = 0.75$, $M_\infty = 0.15$.

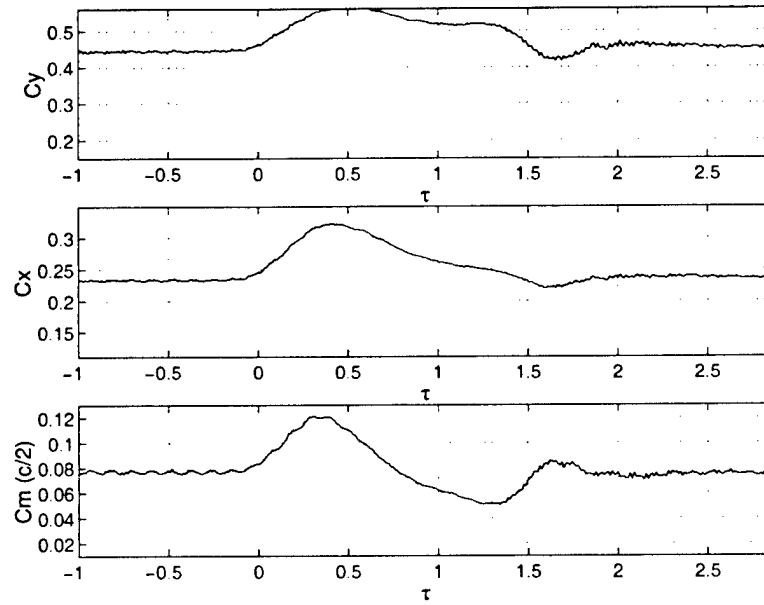


Figure 89: Fluctuation in blade force and moment coefficients. $w/c = 0.4$, $\rho_2/\rho_1 = 2.00$, $M_\infty = 0.15$.

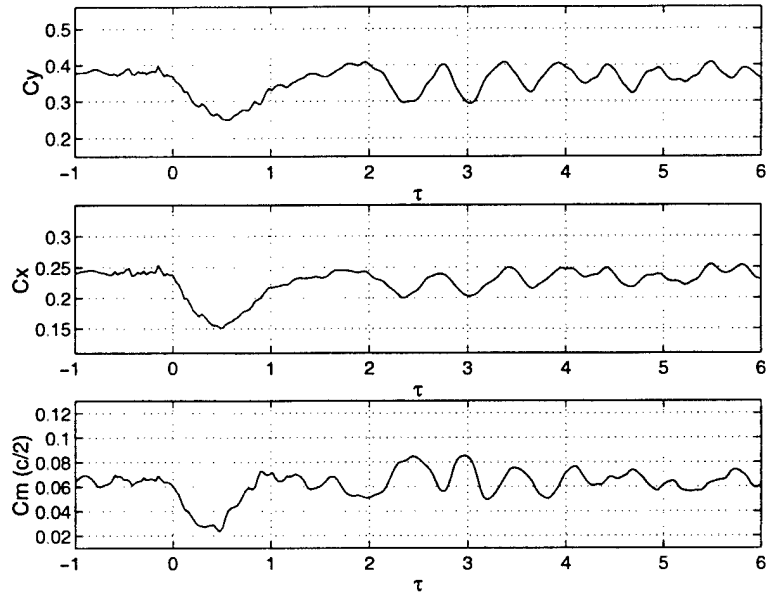


Figure 90: Fluctuation in blade force and moment coefficients. $w/c = 0.4$, $\rho_2/\rho_1 = 0.25$, $M_\infty = 0.53$.

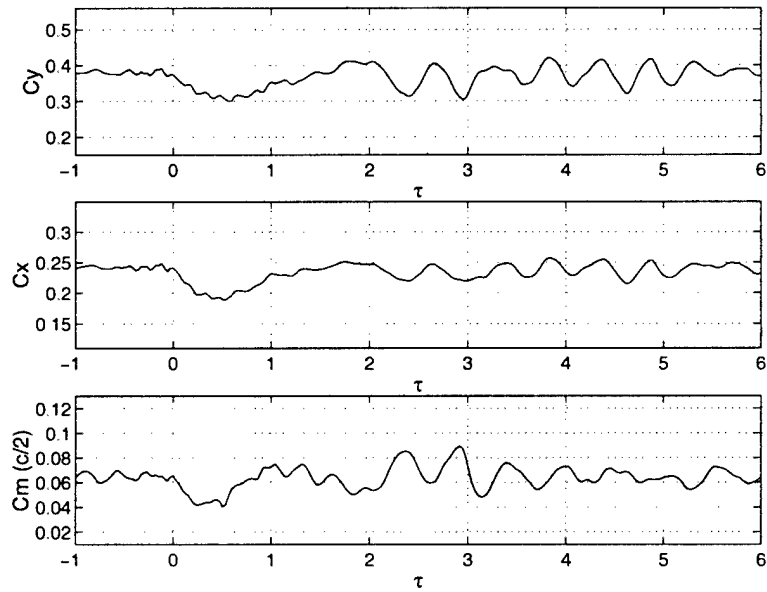


Figure 91: Fluctuation in blade force and moment coefficients. $w/c = 0.4$, $\rho_2/\rho_1 = 0.50$, $M_\infty = 0.53$.

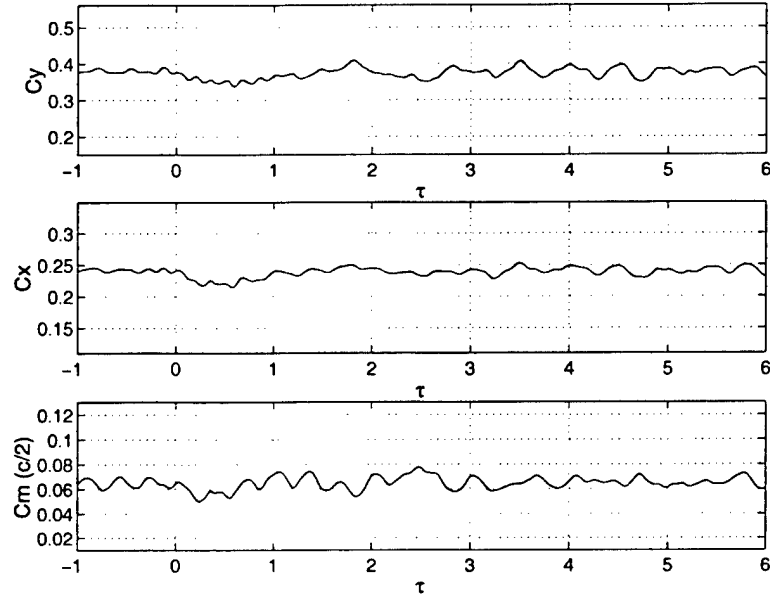


Figure 92: Fluctuation in blade force and moment coefficients. $w/c = 0.4$, $\rho_2/\rho_1 = 0.75$, $M_\infty = 0.53$.

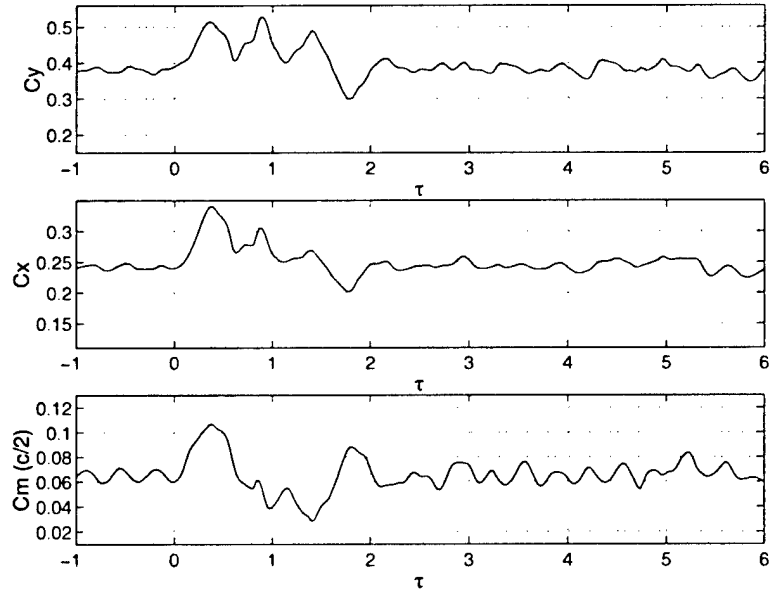


Figure 93: Fluctuation in blade force and moment coefficients. $w/c = 0.4$, $\rho_2/\rho_1 = 2.00$, $M_\infty = 0.53$.

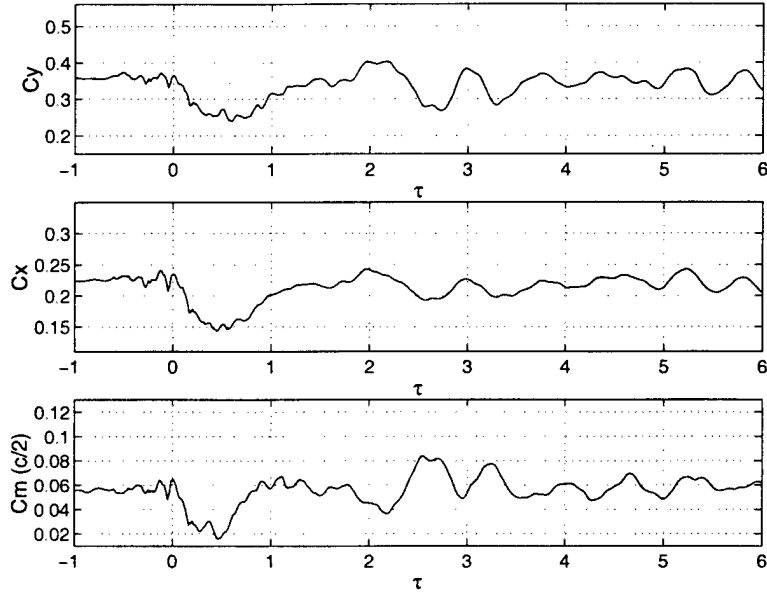


Figure 94: Fluctuation in blade force and moment coefficients. $w/c = 0.4$, $\rho_2/\rho_1 = 0.25$, $M_\infty = 0.63$.

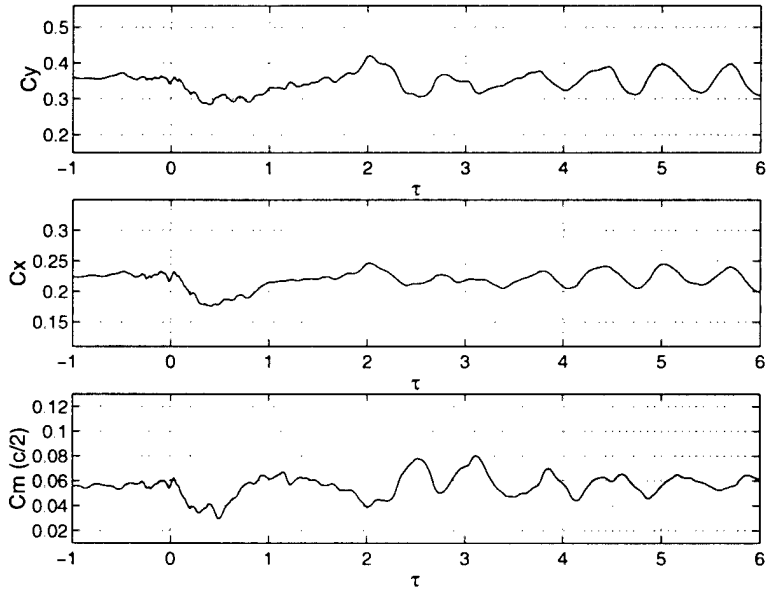


Figure 95: Fluctuation in blade force and moment coefficients. $w/c = 0.4$, $\rho_2/\rho_1 = 0.50$, $M_\infty = 0.63$.

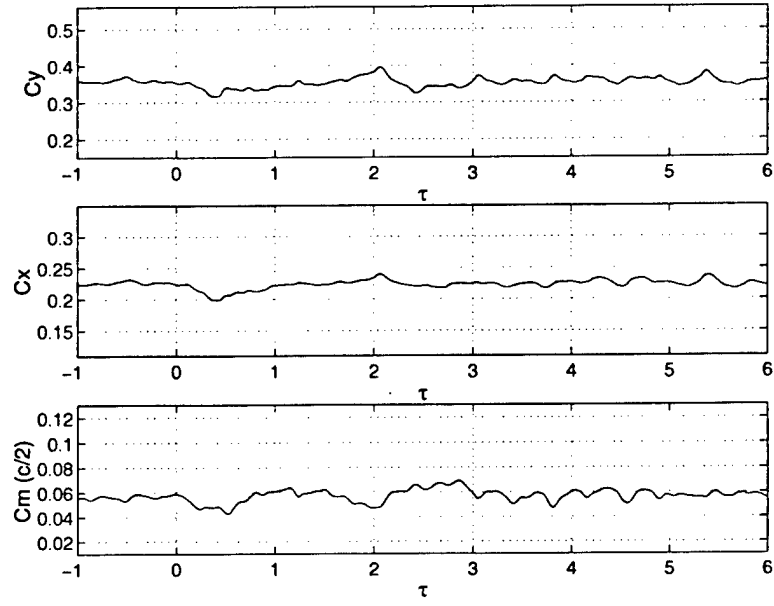


Figure 96: Fluctuation in blade force and moment coefficients. $w/c = 0.4$, $\rho_2/\rho_1 = 0.75$, $M_\infty = 0.63$.

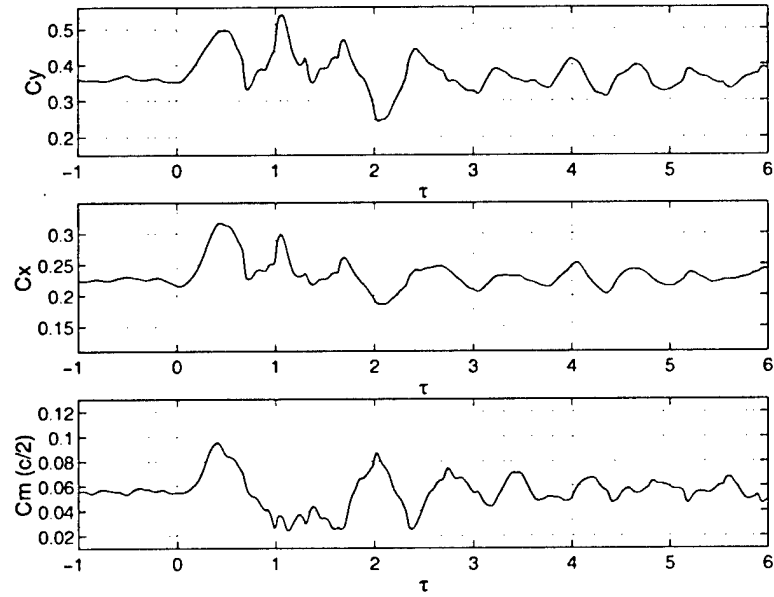


Figure 97: Fluctuation in blade force and moment coefficients. $w/c = 0.4$, $\rho_2/\rho_1 = 2.00$, $M_\infty = 0.63$.

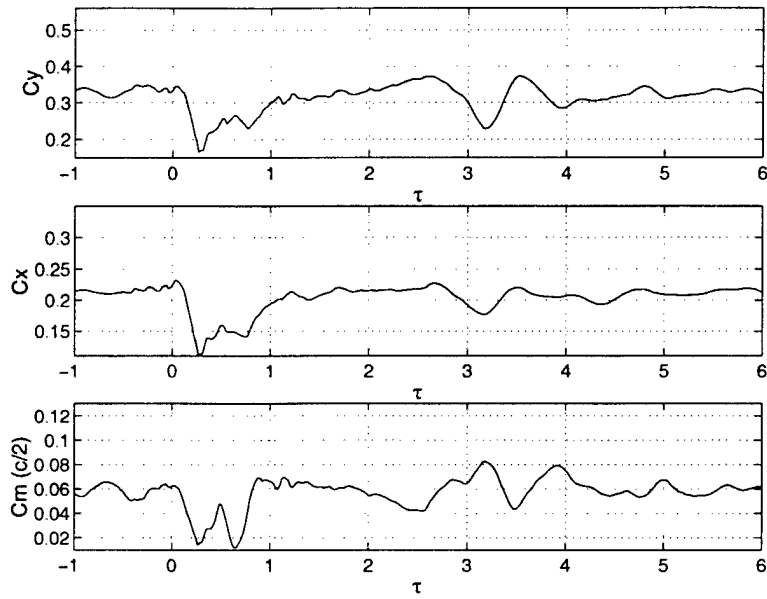


Figure 98: Fluctuation in blade force and moment coefficients. $w/c = 0.4$, $\rho_2/\rho_1 = 0.25$, $M_\infty = 0.87$.

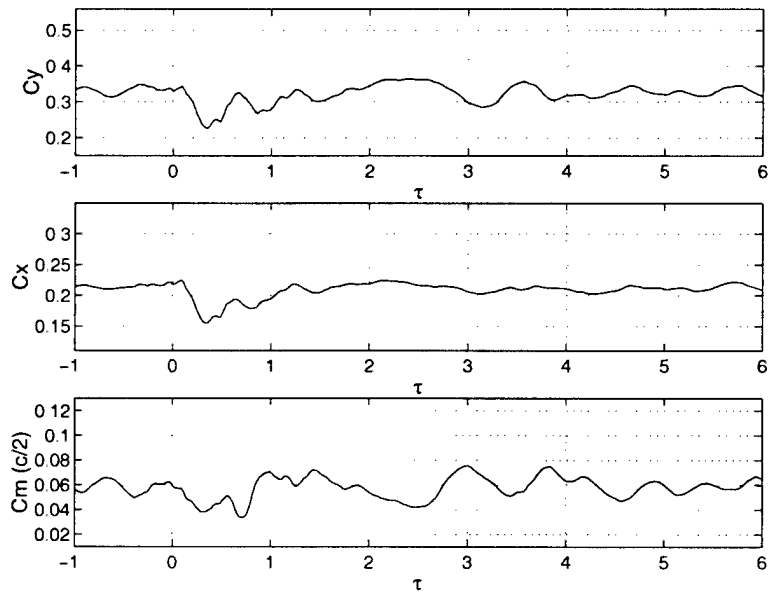


Figure 99: Fluctuation in blade force and moment coefficients. $w/c = 0.4$, $\rho_2/\rho_1 = 0.50$, $M_\infty = 0.87$.

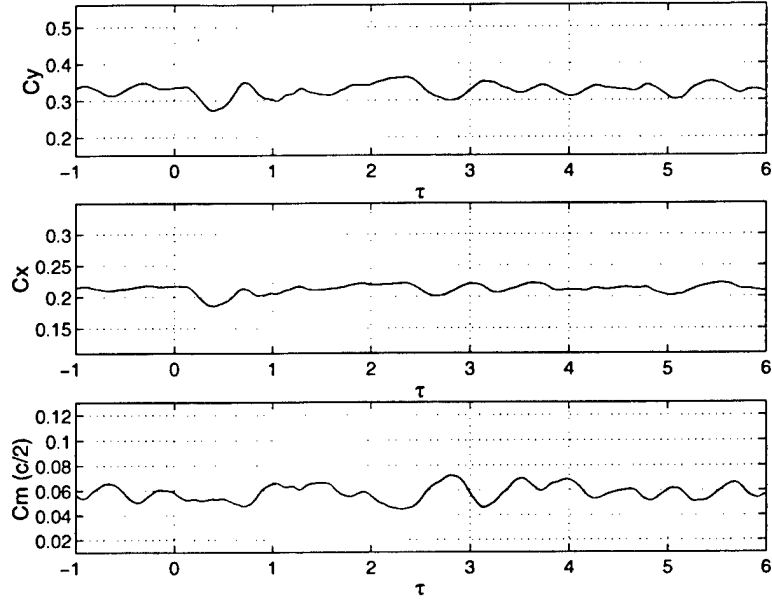


Figure 100: Fluctuation in blade force and moment coefficients. $w/c = 0.4$, $\rho_2/\rho_1 = 0.75$, $M_\infty = 0.87$.

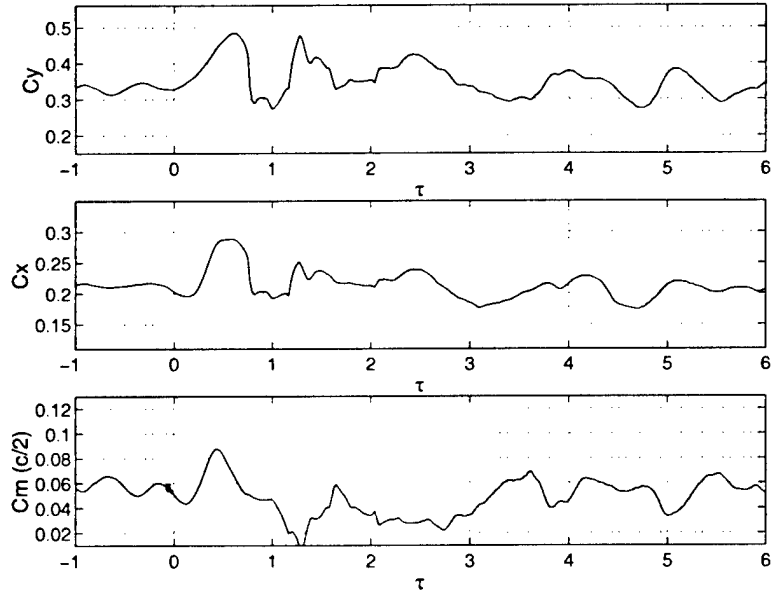


Figure 101: Fluctuation in blade force and moment coefficients. $w/c = 0.4$, $\rho_2/\rho_1 = 2.00$, $M_\infty = 0.87$.

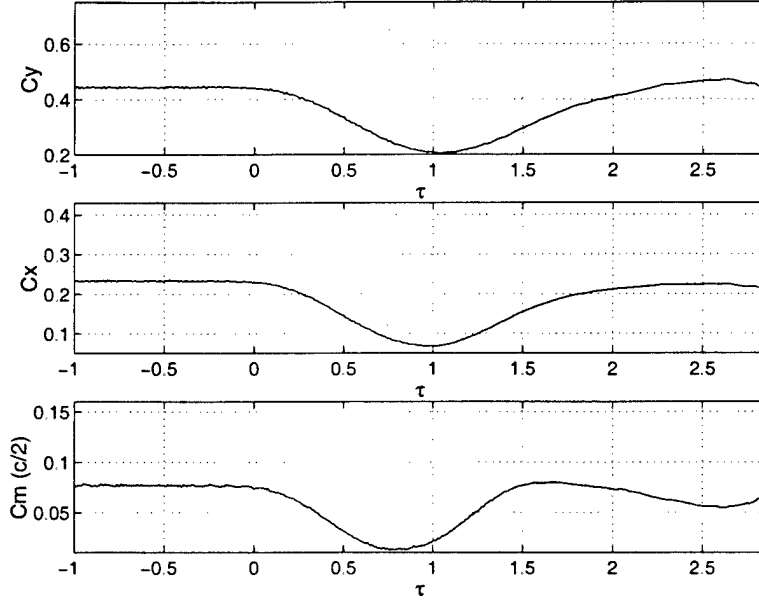


Figure 102: Fluctuation in blade force and moment coefficients. $w/c = 1.0$, $\rho_2/\rho_1 = 0.25$, $M_\infty = 0.15$.

16.1 Functional Relationships - Primary Response

The change in the maximum fluctuation of the primary response force and moment coefficients can be expressed by the following algebraic relationships,

$$\% \frac{C_{y_{max}} - C_{y_{mean}}}{C_{y_{mean}}} = \Pi_1 \rho^{*2} + \Pi_2 \rho^* + \Pi_3 \quad (22)$$

$$\% \frac{C_{m_{max}} - C_{m_{mean}}}{C_{m_{mean}}} = \Pi_1 \rho^{*2} + \Pi_2 \rho^* + \Pi_3 \quad (23)$$

$$\% \frac{C_{x_{max}} - C_{x_{mean}}}{C_{x_{mean}}} = \Pi_1 \rho^{*2} + \Pi_2 \rho^* + \Pi_3 \quad (24)$$

The constants Π_1 , Π_2 and Π_3 in the functional relationships are tabulated in Table 6 through Table 9 for each free stream Mach number flow. Note the functional relationships obtained here represent “best fit” curves to the data in a least-squares sense. This results in a small non-zero value for the Π_3 constant, often 2 orders of magnitude smaller than the values for Π_1 and Π_2 , which can be ignored.

The Π_2 constant for all force and moment coefficients is seen to increase by a factor of between 1.5–2.0 as the wake width doubles. The value for Π_1 also increases with increasing wake width, however in a much less defined manner by a factor of between 2–20 as the

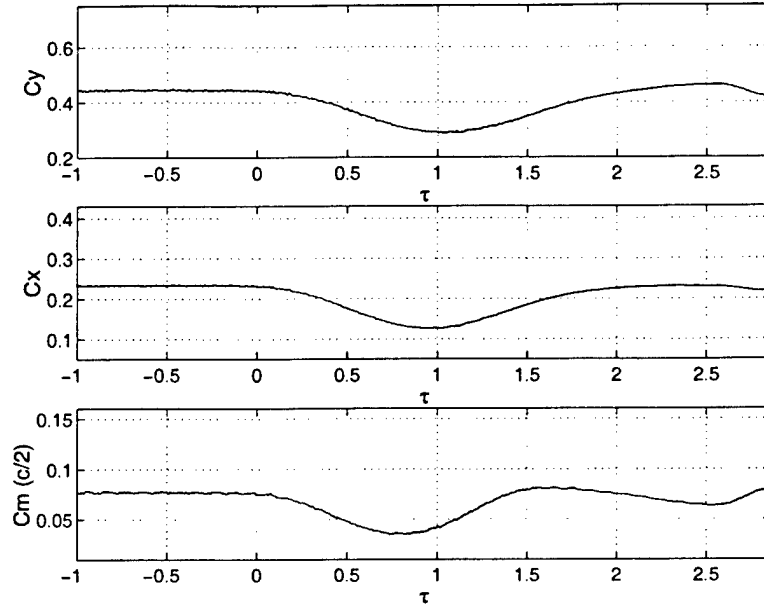


Figure 103: Fluctuation in blade force and moment coefficients. $w/c = 1.0$, $\rho_2/\rho_1 = 0.50$, $M_\infty = 0.15$.

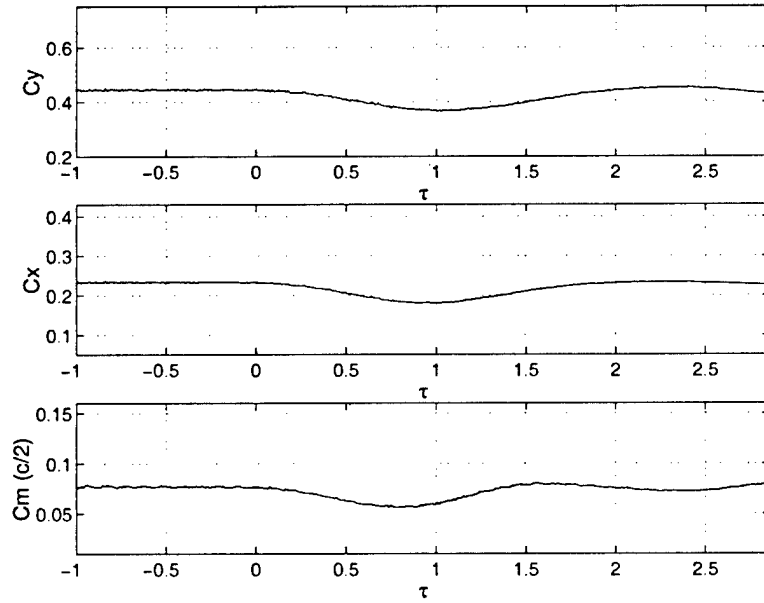


Figure 104: Fluctuation in blade force and moment coefficients. $w/c = 1.0$, $\rho_2/\rho_1 = 0.75$, $M_\infty = 0.15$.

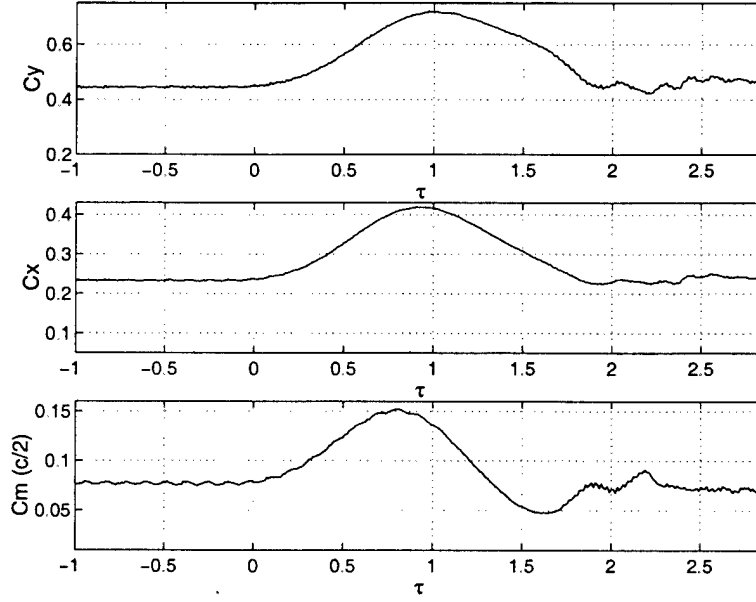


Figure 105: Fluctuation in blade force and moment coefficients. $w/c = 1.0$, $\rho_2/\rho_1 = 2.00$, $M_\infty = 0.15$.

| Coefficient | Wake Width (w/c) | Π_1 | Π_2 | Π_3 |
|-------------|----------------------|---------|---------|---------|
| C_y | 0.1 | 1.9 | 23.0 | -0.1 |
| | 0.2 | 7.2 | 40.4 | 0.2 |
| | 0.4 | 28.7 | 73.4 | 0.2 |
| | 1.0 | 95.0 | 149.3 | 1.1 |
| C_m | 0.1 | -4.4 | 41.7 | -0.5 |
| | 0.2 | 3.9 | 74.5 | -0.7 |
| | 0.4 | 60.6 | 143.0 | 0.9 |
| | 1.0 | 141.9 | 226.8 | 2.3 |
| C_x | 0.1 | -2.7 | 28.7 | 0.0 |
| | 0.2 | 5.2 | 53.4 | 0.2 |
| | 0.4 | 40.6 | 101.7 | 0.7 |
| | 1.0 | 118.5 | 191.8 | 2.3 |

Table 6: Constants in the functional relationships for the maximum fluctuation in the force and moment coefficients (primary response). $M_\infty = 0.15$.

| Coefficient | Wake Width (w/c) | Π_1 | Π_2 | Π_3 |
|-------------|------------------|---------|---------|---------|
| C_y | 0.1 | 8.7 | 28.4 | 0.5 |
| | 0.2 | 23.3 | 53.0 | -0.1 |
| | 0.4 | 49.9 | 87.5 | 1.0 |
| C_m | 0.1 | 44.5 | 72.2 | -0.3 |
| | 0.2 | 104.2 | 127.0 | 1.0 |
| | 0.4 | 87.3 | 157.5 | 0.4 |
| C_x | 0.1 | 18.5 | 35.8 | 1.4 |
| | 0.2 | 33.8 | 60.8 | 1.4 |
| | 0.4 | 54.8 | 97.3 | 2.0 |

Table 7: Constants in the functional relationships for the maximum fluctuation in the force and moment coefficients (primary response). $M_\infty = 0.53$.

| Coefficient | Wake Width (w/c) | Π_1 | Π_2 | Π_3 |
|-------------|------------------|---------|---------|---------|
| C_y | 0.1 | 9.0 | 29.7 | 0.3 |
| | 0.2 | 33.2 | 54.3 | 0.4 |
| | 0.4 | 58.9 | 90.7 | 0.9 |
| C_m | 0.1 | 39.0 | 75.3 | 1.7 |
| | 0.2 | 52.4 | 111.7 | 0.3 |
| | 0.4 | 99.1 | 178.5 | 0.7 |
| C_x | 0.1 | 10.9 | 35.0 | 0.5 |
| | 0.2 | 34.1 | 62.0 | 1.3 |
| | 0.4 | 59.2 | 97.3 | 1.4 |

Table 8: Constants in the functional relationships for the maximum fluctuation in the force and moment coefficients (primary response). $M_\infty = 0.63$.

| Coefficient | Wake Width (w/c) | Π_1 | Π_2 | Π_3 |
|-------------|------------------|---------|---------|---------|
| C_y | 0.1 | -10.6 | 40.2 | 0.4 |
| | 0.2 | -3.2 | 63.5 | -0.2 |
| | 0.4 | 62.0 | 118.9 | -0.5 |
| C_m | 0.1 | -5.2 | 71.7 | -1.3 |
| | 0.2 | -9.6 | 100.6 | 0.2 |
| | 0.4 | -2.1 | 131.9 | 6.3 |
| C_x | 0.1 | -21.3 | 36.2 | 0.5 |
| | 0.2 | -14.7 | 60.7 | 0.4 |
| | 0.4 | 26.9 | 95.6 | 0.2 |

Table 9: Constants in the functional relationships for the maximum fluctuation in the force and moment coefficients (primary response). $M_\infty = 0.87$.

wake width doubles. The largest increase in Π_1 is seen between wake widths of $0.2c$ and $0.4c$. The functional relations for $M_\infty = 0.87$ have a relatively smaller magnitude for Π_1 compared to the lower Mach number functional relations. This is due to the near-linear variation in the the shock wave motion (and hence blade static pressure fluctuations) with increasing $|\rho^*|$ alluded to in the previous section.

The functional relations should be used with caution. In particular for density parameters $\rho^* \approx 0$ the Π_3 constant may become dominant and the deviation from the data can be large.

16.2 Functional Relationships - Secondary Response

Functional relationships can be derived to help quantify the trends in the secondary response. The change in the amplitude of the force and moment coefficients with density ratio ρ_2/ρ_1 can be expressed by the following algebraic relationships,

$$\% \frac{Cy_{second}}{Cy_{baseline}} = \Phi_1(\rho_2/\rho_1)^2 + \Phi_2(\rho_2/\rho_1) + \Phi_3 \quad (25)$$

$$\% \frac{Cm_{second}}{Cm_{baseline}} = \Phi_1(\rho_2/\rho_1)^2 + \Phi_2(\rho_2/\rho_1) + \Phi_3 \quad (26)$$

$$\% \frac{Cx_{second}}{Cx_{baseline}} = \Phi_1(\rho_2/\rho_1)^2 + \Phi_2(\rho_2/\rho_1) + \Phi_3 \quad (27)$$

The constants Φ_1 , Φ_2 and Φ_3 in the functional relationships are tabulated in Table 10 through Table 13 for each free stream Mach number flow. Note the functional relationships obtained here represent "best fit" curves to the data in a least-squares sense and are valid only for $\rho_2/\rho_1 < 1.0$. Insufficient data points are available to obtain good curve fits for $\rho_2/\rho_1 > 1.0$.

| Coefficient | Wake Width (w/c) | Φ_1 | Φ_2 | Φ_3 |
|-------------|------------------|----------|----------|----------|
| C_y | 0.1 | 18.0 | -32.0 | 15.1 |
| | 0.2 | 5.9 | -18.1 | 13.0 |
| | 0.4 | 9.2 | -25.7 | 17.3 |
| | 1.0 | 8.2 | -20.9 | 13.8 |
| C_m | 0.1 | 19.0 | -34.0 | 16.1 |
| | 0.2 | 10.3 | -25.2 | 15.7 |
| | 0.4 | 10.9 | -28.4 | 18.4 |
| | 1.0 | 0.7 | -10.8 | 11.1 |
| C_x | 0.1 | 8.8 | -16.1 | 8.2 |
| | 0.2 | 3.2 | -9.2 | 7.0 |
| | 0.4 | 8.7 | -19.9 | 12.1 |
| | 1.0 | 39.5 | -66.1 | 28.1 |

Table 10: Constants in the functional relationships for the maximum fluctuation in the force and moment coefficients (secondary response). Valid for $\rho_2/\rho_1 < 1.0$. $M_\infty = 0.15$.

| Coefficient | Wake Width (w/c) | Φ_1 | Φ_2 | Φ_3 |
|-------------|------------------|----------|----------|----------|
| C_y | 0.1 | 11.7 | -21.5 | 10.8 |
| | 0.2 | 0.9 | -8.1 | 8.2 |
| | 0.4 | -5.8 | 1.7 | 5.1 |
| C_m | 0.1 | 3.2 | -7.9 | 5.7 |
| | 0.2 | -5.4 | 3.4 | 3.0 |
| | 0.4 | -5.7 | 4.2 | 2.5 |
| C_x | 0.1 | 6.8 | -13.9 | 8.1 |
| | 0.2 | 5.0 | -12.3 | 8.3 |
| | 0.4 | -4.0 | -0.5 | 5.5 |

Table 11: Constants in the functional relationships for the maximum fluctuation in the force and moment coefficients (secondary response). Valid for $\rho_2/\rho_1 < 1.0$. $M_\infty = 0.53$.

| Coefficient | Wake Width (w/c) | Φ_1 | Φ_2 | Φ_3 |
|-------------|------------------|----------|----------|----------|
| C_y | 0.1 | 6.6 | -12.2 | 6.5 |
| | 0.2 | 3.2 | -9.8 | 7.6 |
| | 0.4 | -3.1 | -1.0 | 5.0 |
| C_m | 0.1 | 3.9 | -8.8 | 5.8 |
| | 0.2 | -0.2 | -5.0 | 6.2 |
| | 0.4 | -1.5 | -3.1 | 5.5 |
| C_x | 0.1 | 8.4 | -15.3 | 7.9 |
| | 0.2 | 4.6 | -11.7 | 8.1 |
| | 0.4 | -1.9 | -4.1 | 6.9 |

Table 12: Constants in the functional relationships for the maximum fluctuation in the force and moment coefficients (secondary response). Valid for $\rho_2/\rho_1 < 1.0$. $M_\infty = 0.63$.

| Coefficient | Wake Width (w/c) | Φ_1 | Φ_2 | Φ_3 |
|-------------|------------------|----------|----------|----------|
| C_y | 0.1 | -4.3 | 2.2 | 3.1 |
| | 0.2 | -6.4 | 5.7 | 1.7 |
| | 0.4 | 4.2 | -9.3 | 6.2 |
| C_m | 0.1 | -2.5 | 0.7 | 2.8 |
| | 0.2 | -5.5 | 5.0 | 1.4 |
| | 0.4 | -1.2 | -0.8 | 3.0 |
| C_x | 0.1 | -0.9 | -1.1 | 3.0 |
| | 0.2 | -3.9 | 3.3 | 1.7 |
| | 0.4 | 6.2 | -11.3 | 6.2 |

Table 13: Constants in the functional relationships for the maximum fluctuation in the force and moment coefficients (secondary response). Valid for $\rho_2/\rho_1 < 1.0$. $M_\infty = 0.87$.

17 Compressibility Scaling Of The Maximum Force and Moment Fluctuations

This Section includes the following plots:

- The maximum fluctuation in the (1) azimuthal force coefficient C_y , (2) axial force coefficient C_x and (3) moment coefficient C_m (primary response) scaled by the Prandtl-Glauert compressibility factor $\sqrt{1 - M_\infty^2}$.

Note the results for the $M_\infty = 0.15$ calculation are overlayed in each plot for comparison purposes.

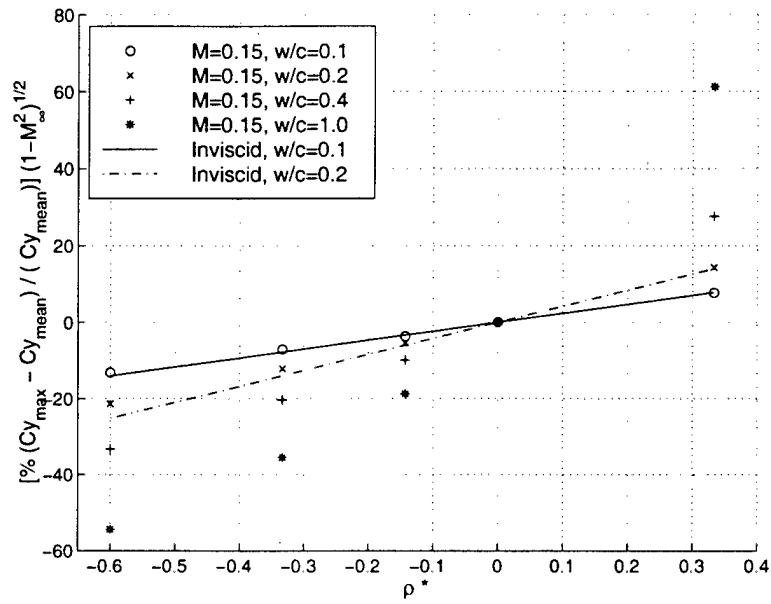


Figure 106: Comparison of the $M_{\infty} = 0.15$ viscous results and the inviscid results for the maximum fluctuation in the azimuthal force coefficient.

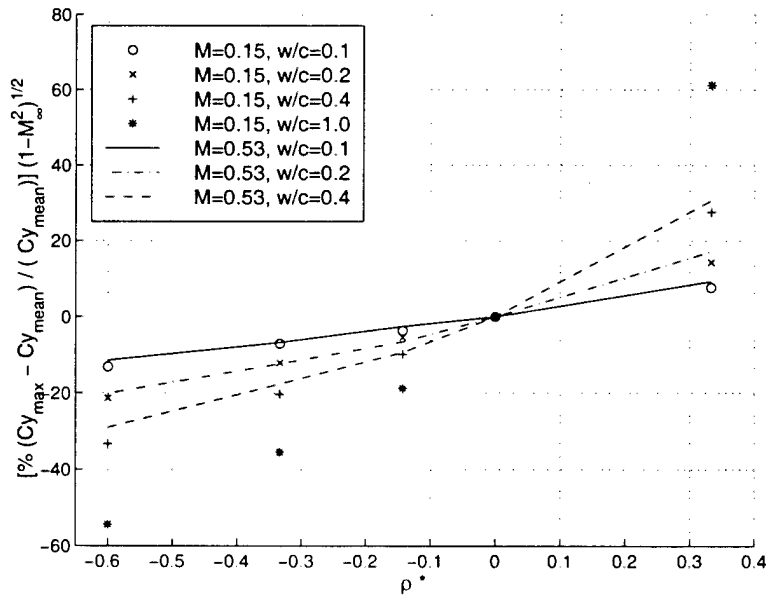


Figure 107: Comparison of the $M_{\infty} = 0.15$ and the $M_{\infty} = 0.53$ viscous results for the maximum fluctuation in the azimuthal force coefficient.

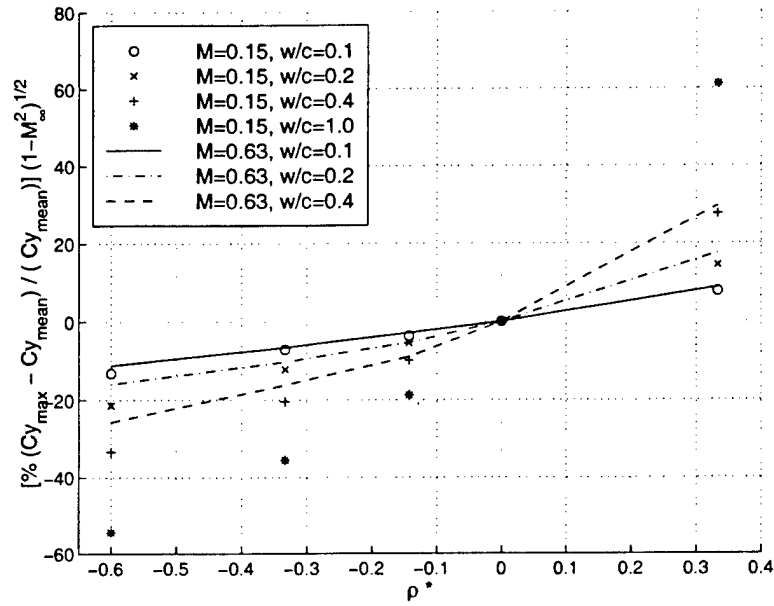


Figure 108: Comparison of the $M_{\infty} = 0.15$ and the $M_{\infty} = 0.63$ viscous results for the maximum fluctuation in the azimuthal force coefficient.

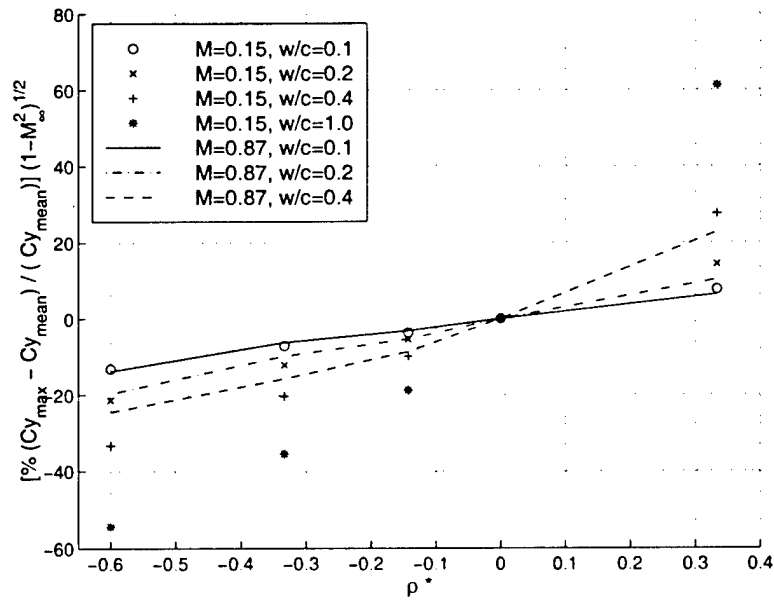


Figure 109: Comparison of the $M_{\infty} = 0.15$ and the $M_{\infty} = 0.87$ viscous results for the maximum fluctuation in the azimuthal force coefficient.

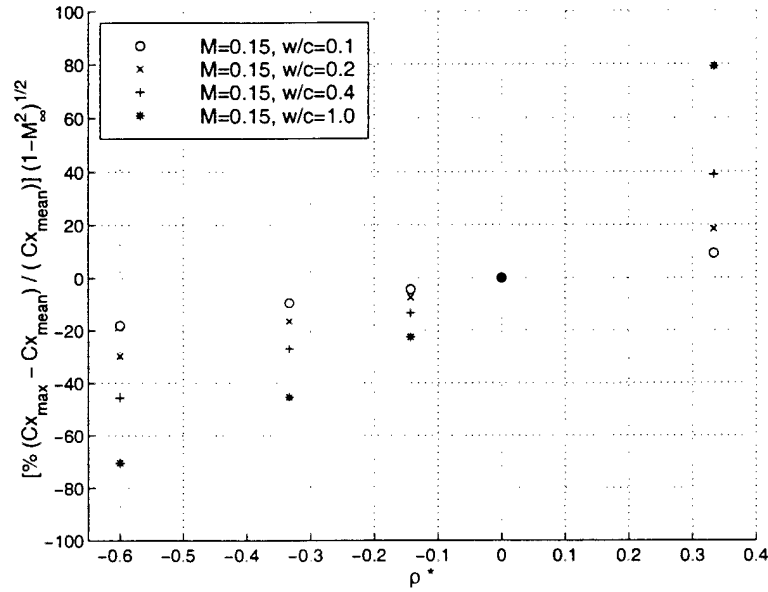


Figure 110: $M_\infty = 0.15$ viscous result for the maximum fluctuation in the axial force coefficient.

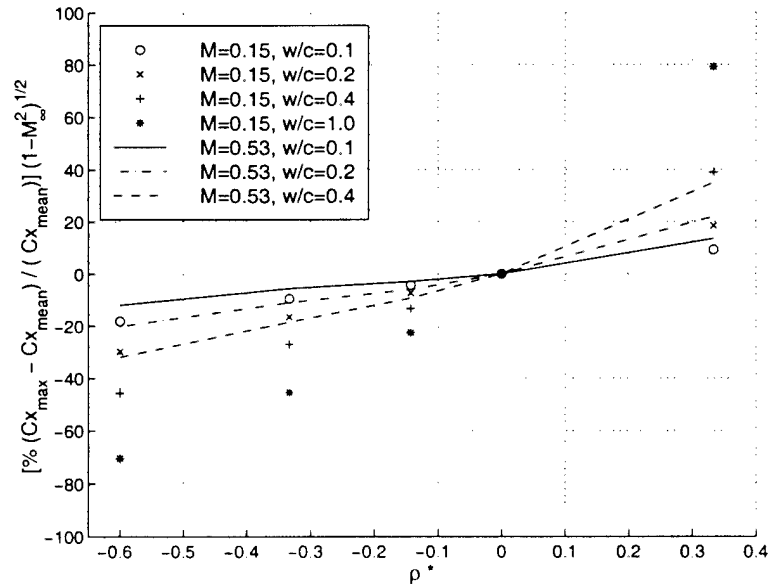


Figure 111: Comparison of the $M_\infty = 0.15$ and the $M_\infty = 0.53$ viscous results for the maximum fluctuation in the axial force coefficient.

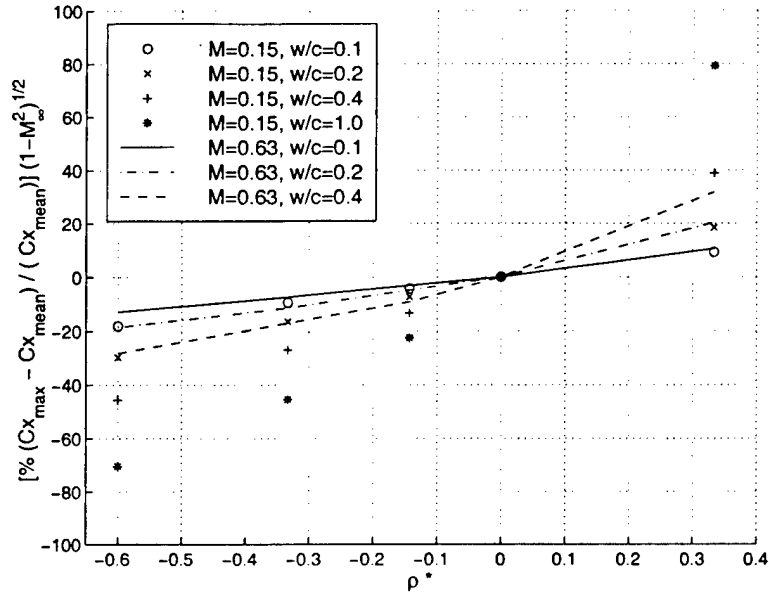


Figure 112: Comparison of the $M_{\infty} = 0.15$ and the $M_{\infty} = 0.63$ viscous results for the maximum fluctuation in the axial force coefficient.

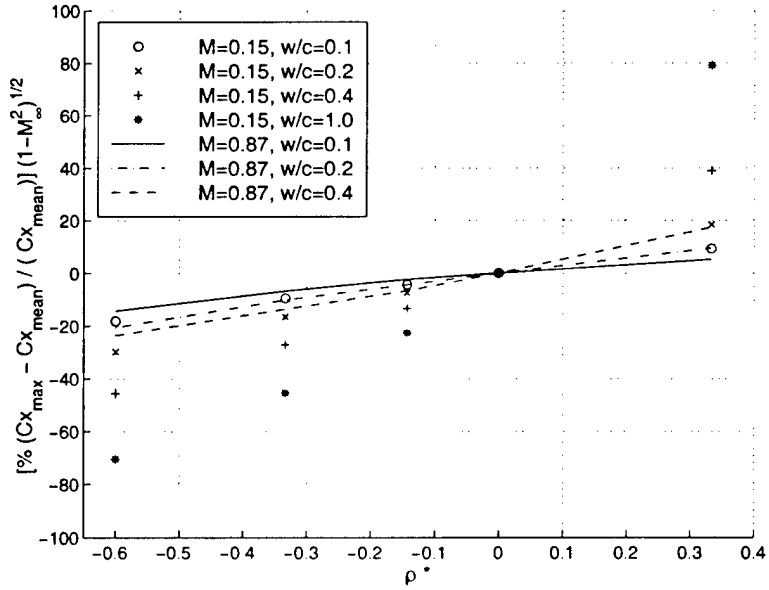


Figure 113: Comparison of the $M_{\infty} = 0.15$ and the $M_{\infty} = 0.87$ viscous results for the maximum fluctuation in the axial force coefficient.

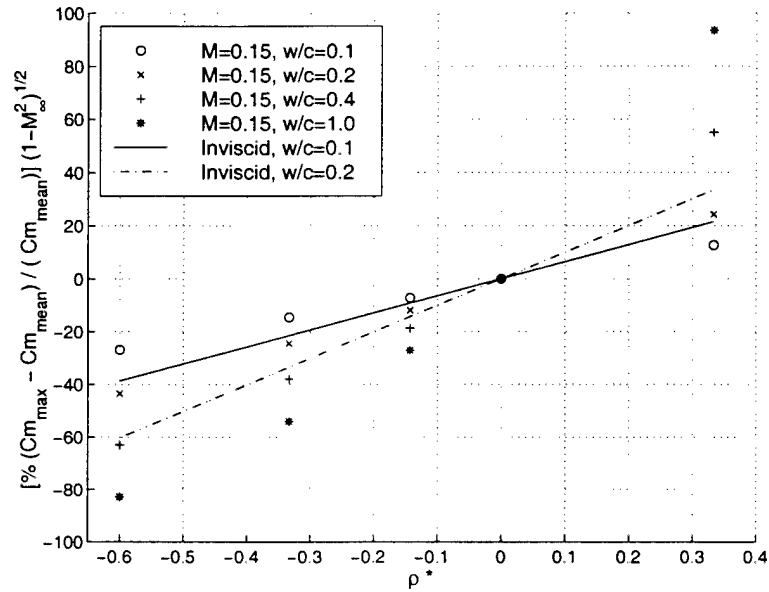


Figure 114: Comparison of the $M_\infty = 0.15$ viscous results and the inviscid results for the maximum fluctuation in the moment coefficient.

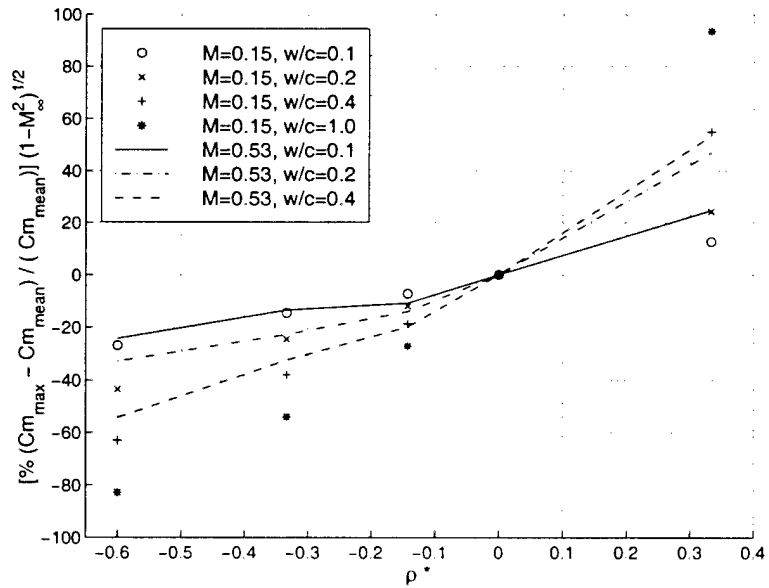


Figure 115: Comparison of the $M_\infty = 0.15$ and the $M_\infty = 0.53$ viscous results for the maximum fluctuation in the moment coefficient.

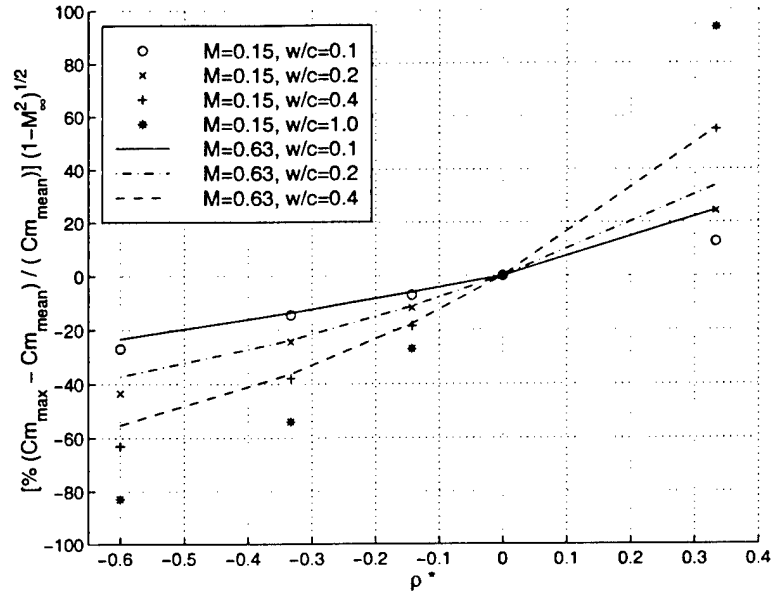


Figure 116: Comparison of the $M_{\infty} = 0.15$ and the $M_{\infty} = 0.63$ viscous results for the maximum fluctuation in the moment coefficient.

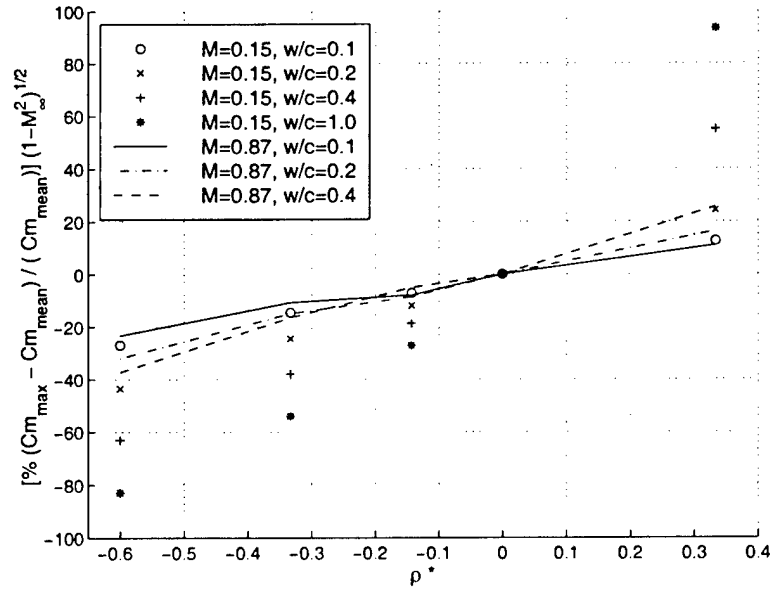


Figure 117: Comparison of the $M_{\infty} = 0.15$ and the $M_{\infty} = 0.87$ viscous results for the maximum fluctuation in the moment coefficient.

18 Cascade Model : Matlab Source Code

Filename: cascade.m

```
% [Cascade flow model v7.0]
% Written by Sanith Wijesinghe
% MIT Gas Turbine Lab. July 1998.
%
% Matlab script file.
%
% Lift and moment fluctuation on a flat plate cascade induced by a
% convecting density wake.
%
% Notes:
% o Cascade flat plate extends from -0.5 to +0.5.
% o Uncomment lines where indicated for either steady or quasi-steady
%   simulation.

% List of Symbols:

% N          = no. of vortex panels
% z          = vector of bound vortex locations
% x          = vector of collocation locations
% alpha      = flow angle of attack
% beta1      = stagger angle of blades
% sig        = gap-chord ratio

% beta2      = stagger angle of counterrotating vortices
% gamax, gbmax = max. circulation of the counterrotating vortices
% d          = separation of counterrotating vortices
% r2r1       = density ratio  $\rho_2 / \rho_1$ 
% l1         = max. upstream extent of press. field }
% l2         = downstream extend of press. field   } defines tanh func.
% sa         = location of vortex A (counterrotating pair)
% sb         = location of vortex B (counterrotating pair)
% k          = empirical constant determined from inviscid CFD

% cl         = lift coeff. normal to flat plate  $\{L/(0.5*\rho*U^2*c)\}$ 
% cm         = moment coeff. about mid chord  $\{M/(0.5*\rho*U^2*c^2)\}$ 
%
%-----

clear all;
```

```

% Initialize
global x1 sig beta1      %% Set global parameters

alpha = 5*pi/180;  %% General parameters
p      = 0.0;
q      = 0.0;
vel1   = 0.0;
vel2   = 0.0;
flag1  = 0.0;

N      = 5;        %% Cascade parameters
sig    = 0.666;
beta1  = 20*pi/180;
t      = 1:N;
z      = -0.5 + (t-1).*(1/N) + (1/N)*(0.25);
x      = -0.5 + (t-1).*(1/N) + (1/N)*(0.75);

l1     = -0.80;    %% Wake parameters
l2     = -0.10;
n      = -2;
beta2  = beta1;
d      = 0.1;
r2r1   = 0.50;
k      = 0.322;
coeffa = 6/(l2-l1);
coeffb = -3*(l1+l2)/(l2-l1);

% Start Main loop

%++ Uncomment this section for steady flow simulation

% for beta1 = 0*pi/180:10*pi/180:60*pi/180  %% Step in stagger angles
%   p=p+1
%   for sig = 0.01:0.1:4.0;    %% Step in gap-chord ratios
%       q=q+1;

%++

% Evaluate aero-influence coefficient matrix
for a=1:N,
    for b=1:N,
        x1 = x(a);                %% Set collo. pt. in kernel function.
        sum1 = -imag(kernel(z(b))); %% B. vortex z(b) infl. at loc. x(a).
    end
end

```

```

        A(a,b) = sum1;                %% A matrix
    end
end

%++ Uncomment this section for quasi-steady flow simulation

% Convect vortex pair
    p = p + 1
    for n = -1.0:0.02:2.5;
        q = q + 1;

%++

        sa = n;
        sb = sa - d;

% Hyperbolic tangent variation in vortex strength

        if sa <= l1
            ga = 0.0;
        elseif sa > l1 & sa <= l2
            ga = gamax*(1+tanh(coeffa*sa + coeffb))*0.5;
        elseif sa > l2
            ga = gamax;
        end
        gb = -ga;

% RHS source terms

for v=1:N %% Counterrotating Vortex pair infl. at panels + l.e.

    pa = imag(i*ga*exp(i*beta2)*coth((pi*(1/sig)*(x(v)-sa)
                                         + i*pi/2)*exp(i*beta2))));

    pb = imag(i*gb*exp(i*beta2)*coth((pi*(1/sig)*(x(v)-sb)
                                         + i*pi/2)*exp(i*beta2))));

    la = imag(i*ga*exp(i*beta2)*coth((pi*(1/sig)*(-0.5-sa)
                                         + i*pi/2)*exp(i*beta2))));

    lb = imag(i*gb*exp(i*beta2)*coth((pi*(1/sig)*(-0.5-sb)
                                         + i*pi/2)*exp(i*beta2))));

```

```

    w(v) = pa+pb+la+lb-sin(alpha);
end

gam    = inv(A)*w';           %% Solve for Gamma
cl     = 4*sig*(sum(gam));    %% Calculate lift coeff.
cm     = 4*sig*(gam'*z');     %% Calculate moment coeff.
kint   = cl/(-2*pi*sin(alpha)); %% Interf. -> cl(cas.)/cl(air.)

% Solution vector

out1(p,q) = n;
out2(p,q) = cl;
out3(p,q) = cm;
out4(p,q) = kint;
out5(p,q) = sig;
out6(p,q) = beta1;

% Calculate gamax and gbmax

if flag1 == 0.0

% gamma(x)dx -> gamma(x)

    g1 = gam/(1/N);

% Set gamax and gbmax using gamma@0.25 = (Cps-Cpp) and r2/r1

    gamax = -k*(g1(5))*(r2r1-1.0)
    gbmax = k*(g1(5))*(r2r1-1.0)

    flag1 = 1.0;
end

%++ Uncomment this section for steady flow simulation

% end
% q=0;

%++

end

% Maximum change in the lift and moment coefficients

```

```

chcl = -((max(out2(1,:))-out2(1,1))/out2(1,1))*100
chcm = ((max(out3(1,:))-out3(1,1))/out3(1,1))*100

```

```

%-----<END>-----

```

Filename: kernel.m

```

% Kernel function to be used with cascade model.

```

```

%

```

```

% Written by Sanith Wijesing

```

```

% MIT Gas Turbine Lab. July 1998.

```

```

%-----

```

```

function [t] = kernel(e)

```

```

global x1 sig beta1

```

```

nu = size(e,2);

```

```

sx = x1*ones(1,nu);

```

```

zt1 = sx-e;

```

```

t = (-i*exp(i*beta1)*coth(pi*(zt1)*(1/sig)*exp(i*beta1)));

```

```

%-----<END>-----

```